AN ABSTRACT OF THE THESIS OF

Paul Fuchs, for the degree of Doctor of Philosophy in Physics, presented on August 10, 1992.

Title: The Measurement of the Asymmetry in Pion-Proton Bremsstrahlung with positive pions at 261 MeV

Abstract approved: _____
Al Stetz

An attempt was made to measure the asymmetry in pion-proton bremsstrahlung with positive pions at 261 MeV kinetic energy. The experiment was carried out at the TRIUMF cyclotron laboratory. A beam of π^+ mesons was scattered off a polarized proton target (the TRIUMF frozen spin target) which produced an average polarization of 80 % normal to the scattering plane. All three outgoing particles from the bremsstrahlung reaction $\pi^+ p \rightarrow \pi^+ p\gamma$ were detected. The pion momentum was measured with a spectrometer consisting of a dipole magnet and a total of four horizontal drift chambers. The proton energy and angle were measured with an array of plastic scintillator blocks while the photon was detected with one of two large NaI crystals. Data were taken for a total of six weeks in January and April of 1989 at various experimental configurations. Only the most promising part of the data, taken during the last week in April, has been analysed.

Due to technical difficulties, particularly with the detector calibrations, no results for the asymmetry in pion-proton bremsstrahlung could be extracted from the measurements. We therefore present the details of the experiment from a general point of view with a special emphasis on the design phases for a new experiment.

The Measurement of the Asymmetry in Pion-Proton Bremsstrahlung with Positive Pions at 261 MeV

by
Paul Fuchs

A THESIS
submitted to
Oregon State University

in partial fulfillment of the
requirements for the degree of

Doctor of Philosophy

Completed August 10, 1992
Commencement June 1993.

Approved:

Redacted for Privacy

Professor of Physics in charge of major

Redacted for Privacy

Chairman of the Department of Physics

Redacted for Privacy

Dean of Graduate School

Date thesis presented August 10, 1992

Typed by Paul Fuchs using the text system LaTeX.

Acknowledgements

This experiment and thesis could not have been successful without the help of a great many people. I wish to thank my collaborators C. Choi, H. Coombes, F. Farzanpay, P. Green, D. Healey, R. Henderson, P. Kitching, D. Mack, G. Moss, W. Olsen, D. Ottewell, G. Smith, N. Stevenson, W. Swenson and N. Zhang, who helped at one stage or another.

I am particularly grateful to Dr. Gerry Moss and my very good friend Herb Coombes both of whom have taken on an almost fatherly role in my training. Their experience and insights have been an invaluable resource for me to draw on.

I owe many thanks to my supervisor Dr. Al Stetz who has given me support throughout all phases of this work and who has always backed me up, even when he did not agree with me.

There are many more people to whom I want to express my gratitude, be it for some timely advice or their lasting friendship.

Nothing can repay the debt I owe to my parents. They have always helped me out financially without giving a second thought to their own needs and I would not know where I'd be today without their advice and moral support. This thesis is dedicated to them -

and, of course, Carolanne.

Table of Contents

List of Figures

List of Tables

The Measurement of the Asymmetry in Pion-Proton Bremsstrahlung with Positive Pions at 261 MeV

Part I

Theory

Chapter 1

Introduction

As an introduction to Bremsstrahlung it is useful to discuss some general features of the electromagnetic interaction. To quote Harold Fearing [37] :

> "The electromagnetic interaction has several features which make it very useful as a probe of hadronic systems. In the first place it is 'weak'. Thus it can almost always be treated just to first order. One does not have to worry, for the photon, about the uncertainties introduced by distortion effects which are crucial for reactions induced by, say, protons or pions. ...The electromagnetic interaction is also 'known' so that the photon becomes, in principle, a useful probe of the less well known strong interactions.
>
> However, the electromagnetic interaction, while known, is also 'complicated'. This is not because the primary interaction itself is complicated. The coupling of a photon to a free elementary particle is in fact very simple. Its form is determined by general principles and there is usually a great deal of experimental information available to pin down form factors. The interaction becomes complicated because the hadronic interaction being probed is complicated, involving nucleons and clouds of pions or other mesons being exchanged, or at another level many quarks and gluons. The photons must couple to each charged particle. Thus even fairly simple microscopic descriptions of a strong process will lead to many contributions when a photon is coupled to all charges. ...

Another feature of the electromagnetic interaction is that it couples to a 'conserved current'. This is both a blessing and a curse. Current conservation allows one to use very general relations which often combine a lot of unknown and complicated physics into a simple result. ... Soft photon theorems [1,2,3] are an example of the use of current conservation to obtain a simple result, in this case a result which expresses the amplitude for a radiative process in terms of that for the non radiative process through the first two orders in the photon momentum k. However, current conservation implies constraints among many different contributions, and a photon coupling to a particular diagram may often imply coupling to many other diagrams so as to enforce the conservation. Thus it is often hard to obtain a 'simple' conserved current.

An essentially equivalent property of the electromagnetic interaction is that of 'gauge invariance', really just another way of stating current conservation. The full theory must be gauge invariant and in practice this both requires the existence of more complicated contributions and enforces cancellations among the various contributions. ... A very important but often ignored consequence of this cancellation enforced by gauge invariance is the fact that the relative magnitudes of the various diagrams are gauge dependent quantities. Thus to compare sizes of non gauge invariant subsets of diagrams is physically meaningless.

Thus to summarize, in this section we have considered some general properties of the electromagnetic interaction. It is 'weak' and 'known' and so should be a good probe of hadronic systems. It is however at the same time 'complicated' and 'constrained' by current conservation and gauge invariance and so provides a non-trivial and hence interesting window on these strongly interacting systems."

Kondratyuk and Ponomarev [6] were among the first to suggest that these ideas should be applied to the pion-proton system to study electromagnetic properties of the intermediate hadronic state, the delta Δ. Particularly, the study of the

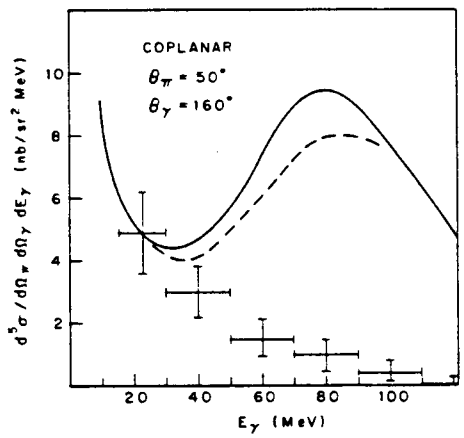

Figure 1. Predictions for the bremsstrahlung cross section based on the soft photon approximation. The solid line is a calculation by Picciotto [30], the dashed line by Fischer and Minkowski [11]. The results are compared to experimental data [29].

bremsstrahlung reaction $\pi^+ p \to \pi^+ p\gamma$ should allow one to determine the magnetic moment $\mu_{\Delta^{++}}$ of the Δ^{++}. First predictions for the cross section of this process were based either on the application of soft photon theorems [10,11,19,26], which employ gauge invariance to estimate possible internal contributions, or on effective isobar models [20,27,33], which treat the delta as an elementary particle with an effective magnetic moment coupling to the photon. In the latter case, the radiative vertex $\Delta\gamma\Delta$ was treated in first order only. All calculations agreed with each other qualitatively in that they predicted a rise in the cross section at intermediate photon energies due to the emergence of the delta resonance. It therefore came as a great surprise that data taken in a series of experiments in the 1970s by a group from UCLA [17,29,32] showed no such enhancement at all, but rather a smooth fall off in the cross section roughly following a $1/k$ behaviour (figure 1). This apparent contradiction sparked a flurry of further theoretical work [34,30,25,24,23,19,16] which eventually lead to an understanding of the importance of ambiguities inherent in soft photon theorems in the presence of a wide resonance.

It was recognized that what was needed was a dynamically consistent model not only for the elastic $\pi^+ p$ scattering process but for the full bremsstrahlung reaction. This approach was pioneered by a group at MIT [35,41] who started from a

non-relativistic framework to build a model that obeyed not only gauge invariance but also unitarity. Those same features were present in a fully relativistic model developed by Rick Wittman at TRIUMF [42]. These more comprehensive calculations were able to reproduce the absence of structure in the bremsstrahlung data through subtle cancellations among the various contributing amplitudes. Yet the predictions still disagreed with the data at higher photon energies, where the cross section was typically overestimated by a factor of two or more. At the same time, the calculations showed that results for spin observables are quite sensitive to the basic assumptions in the models. In recent years two experiments got under way to measure the asymmetry in the bremsstrahlung reaction normal to the scattering plane. One was run at PSI in Switzerland the results of which have now been published [43,44,45] and the other is the topic of this thesis.

The following chapters will discuss the various theoretical models in greater detail and compare their predictions to available data.

Chapter 2

Bremsstrahlung – The Classical Limit

A particle of charge ze undergoing acceleration emits radiation of energy ω and direction $\vec{n}$ with an intensity [46]

$$\frac{d^2I}{d\omega d\Omega} = \frac{z^2e^2}{4\pi^2c}\left|\int \frac{d}{dt}\left[\frac{\vec{n}\times(\vec{n}\times\vec{\beta})}{1-\vec{n}\cdot\vec{\beta}}\right] e^{i\omega(t-\vec{n}\cdot\vec{r}(t)/c)}dt\right|^2 \tag{2.1}$$

where $\vec{r}(t)$ describes the path of the particle relative to some origin

$\vec{\beta}$ $= \vec{v}/c$ is the velocity vector

$\vec{n}$ is a unit vector pointing towards the observer

A collision between two particles, 1 and 2, with charges z_1e and z_2e respectively, can be described classically as a period of acceleration of limited time duration τ. For very small energies ω, the exponential in equation 2.1 can be set to 1 and the integration can be performed analytically. Notice that the details of the reaction mechanism hidden in the path $\vec{r}(t)$ do not enter in this limit and the result which has been derived entirely in classical terms will still hold in the quantum-mechanical limit. Specifically, for π^+p scattering we will have

$$\lim_{\omega\to 0}\frac{d^2I}{d\omega d\Omega} = \frac{e^2}{4\pi^2c}\left|\vec{\epsilon^\star}\cdot\left\{\left(\frac{\vec{\beta}'_\pi}{1-\vec{n}\cdot\vec{\beta}'_\pi}-\frac{\vec{\beta}_\pi}{1-\vec{n}\cdot\vec{\beta}_\pi}\right)+\left(\frac{\vec{\beta}'_p}{1-\vec{n}\cdot\vec{\beta}'_p}-\frac{\vec{\beta}_p}{1-\vec{n}\cdot\vec{\beta}_p}\right)\right\}\right|^2 \tag{2.2}$$

where

$\vec{\varepsilon}$ = the photon polarization

$\vec{\beta}_\pi, \vec{\beta}_p$ = values of $\vec{\beta}$ for pion and proton, respectively, before the collision

$\vec{\beta}'_\pi, \vec{\beta}'_p$ = values of $\vec{\beta}$ after the collision

In order to establish the connection to the quantum-mechanical form, we first convert equation 2.2 into a spectrum of photons of energy $k = \hbar\omega$. The differential number spectrum per unit energy interval and per unit solid angle of "soft" photons ($\hbar\omega \to 0$) of polarization $\vec{\varepsilon}$ is :

$$\lim_{\omega\to 0} \frac{d^2N}{d(\hbar\omega)d\Omega_\gamma} = \frac{\alpha}{4\pi^2\hbar\omega}\left|\vec{\varepsilon^\star}\cdot\left\{\left(\frac{\vec{\beta}'_\pi}{1-\vec{n}\cdot\vec{\beta}'_\pi}-\frac{\vec{\beta}_\pi}{1-\vec{n}\cdot\vec{\beta}_\pi}\right)+\left(\frac{\vec{\beta}'_p}{1-\vec{n}\cdot\vec{\beta}'_p}-\frac{\vec{\beta}_p}{1-\vec{n}\cdot\vec{\beta}_p}\right)\right\}\right|^2 \tag{2.3}$$

where $\alpha = e^2/\hbar c \approx \frac{1}{137}$ is the fine structure constant. If the cross section for scattering that causes a change in velocity $c\vec{\beta} \to c\vec{\beta}'$ is denoted by $(\frac{d\sigma}{d\Omega})_{\pi^+p\to\pi^+p}$, then the cross section for bremsstrahlung with a pion being scattered into a solid angle $d\Omega_\pi$ and a photon being emitted with energy ω into a solid angle $d\Omega_\gamma$ is

$$\frac{d^5\sigma}{d\Omega_\pi d\Omega_\gamma d(\hbar\omega)} = \left[\lim_{\omega\to 0}\frac{d^2N}{d(\hbar\omega)d\Omega}\right]\cdot(\frac{d\sigma}{d\Omega})_{\pi^+p\to\pi^+p} \tag{2.4}$$

Making use of the particle physics convention $\hbar = c = 1$ and introducing the four-vectors of the photon, k^μ, the pion, q^μ, and the proton, p^μ, we end up with our final result

$$\frac{d^5\sigma}{d\Omega_\pi d\Omega_\gamma dk} = k\frac{\alpha}{4\pi^2}\left|\vec{\varepsilon^\star}\cdot\left\{\frac{p'}{k\cdot p'}-\frac{p}{k\cdot p}+\frac{q'}{k\cdot q'}-\frac{q}{k\cdot q}\right\}\right|^2(\frac{d\sigma}{d\Omega})_{\pi^+p\to\pi^+p} \tag{2.5}$$

The various scalar products are four-vector scalar products.

That equation 2.5 emerges from a quantum-mechanical calculation can be made plausible by considering the diagrams of figure 2. The upper diagram indicates the scattering process without emission of radiation. The lower three diagrams have scattering and also photon emission. Their contributions add coherently. The two diagrams on the left have the photon emitted by the external lines, that is, before

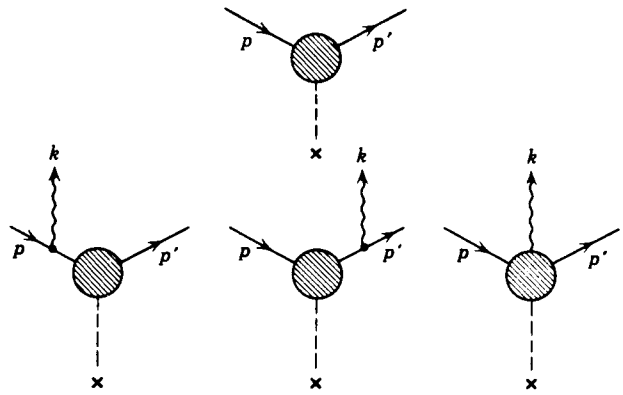

Figure 2. Quantum-mechanical diagrams describing the scattering of a particle without photon emission (top) and with the emission of a photon (bottom).

or after the collision. They both involve propagators for the particle between the scattering vertex and the photon vertex of the form,

$$\frac{1}{(p \pm k)^2 - M^2} = \frac{1}{\pm 2p \cdot k}$$

In the limit $\omega \rightarrow 0$ these propagators make the contributions from these two diagrams singular and provide the $(\hbar\omega)^{-1}$ in equation 2.3. On the other hand, the diagram on the right has the photon emitted from the interior of the scattering vertex. Its contribution is finite as $\omega \rightarrow 0$, and so is negligible compared to the first two. The explicit calculation yields equation 2.4 with 2.5 in the limit that the energy and the momentum of the photon can be neglected in the kinematics. Soft photon emission occurs only from the external lines in any process and is given by the classical result.

Chapter 3

The Soft Photon Theorems

The previous chapter on classical bremsstrahlung suggests that it would be useful to expand the cross section σ in powers of the photon energy k and see what we can learn from a study of the various terms. This idea was originally taken up by Low [1] who showed that the first two terms in

$$\sigma(k) = \frac{\sigma_{-1}}{k} + \sigma_0 + \sigma_1 \cdot k + O(k^2) \tag{3.1}$$

are independent of the details of the reaction and can be expressed in terms of the elastic scattering cross section $\sigma_{\pi^+ p \to \pi^+ p}$. The first term corresponds to the classical result of equation 2.5 and the second is completely determined by the requirement of gauge invariance. This result can also be stated in the form of amplitudes

$$\begin{aligned} M(k) &= \frac{M_{-1}}{k} + M_0 + M_1 \cdot k + O(k^2) \\ \sigma(k) &\propto |M|^2 \end{aligned} \tag{3.2}$$

and can be proven not only for spinless particles, as was originally done by Low, but for particles of any spin [4]. The consequences of this theorem are clear. Non-trivial model-dependent effects such as off-shell behaviour in the vertices or magnetic moment radiation from the internal hadronic states can contribute only to terms of order k or higher.

Let's look at a particular example in order to clarify this point : the scattering of two spin zero bosons, of which only one is charged. We will follow the notation of reference [19].

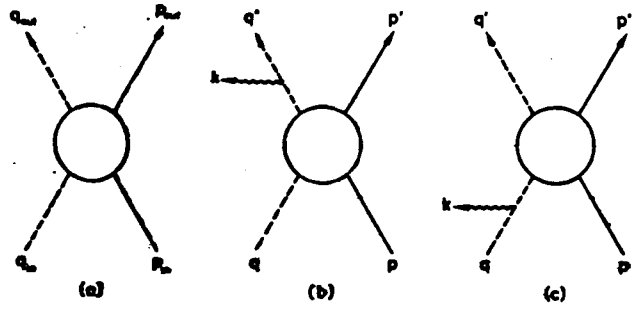

Figure 3. Kinematic variables used to describe (a) the strong amplitude and radiation by the charged particle (b) after and (c) before the interaction.

The four-vectors for the off-shell two-body scattering process are defined as in figure 3.

$$q_{in} + p_{in} \rightarrow q_{out} + p_{out} \tag{3.3}$$

The virtual masses are defined by the parameters

$$\delta = q_{in}^2 - \mu^2,\ \delta' = q_{out}^2 - \mu^2 \tag{3.4}$$

μ being the mass of the radiating particle. The strong amplitude is a function of δ, δ' and two other variables. Those can be chosen to be the two Mandelstam variables $t = (p_{in} - p_{out})^2$ and $s = \frac{1}{2}[(p_{in} + q_{in})^2 + (p_{out} + q_{out})^2]$. For our purposes, t will depend on the external parameters only, so we will neglect it and consider a strong amplitude $\mathcal{A}(s;\delta;\delta')$. $\mathcal{A}(s;0;0)$ is the amplitude on the mass shell.

The four-vectors for radiative scattering are defined as in figure 3 :

$$q + p = q' + p' + k \tag{3.5}$$

The expansion of the amplitude in powers of k will be carried out around $\bar{s} = \frac{1}{2}[(p+q)^2 + (p'+q')^2]$. For diagram 3b we get

$$\delta = 0, \delta' = 2q' \cdot k, s = s_i = (p+q)^2, s_i - s = Q \cdot k, Q = p + q$$

For diagram 3c we get

$$\delta = -2q \cdot k, \delta' = 0, s = s_f = (p'+q')^2, s_f - s = -Q \cdot k$$

The amplitude for the two processes in figs 3b,c can then be written as

$$\frac{1}{e}M^{(1)} = \frac{q'}{q'\cdot k}\mathcal{A}(s_i;0;\delta') - \frac{q}{q\cdot k}\mathcal{A}(s_f;\delta;0) \tag{3.6}$$

This expression is not gauge-invariant, and a gauge counterterm $M^{(2)}$ is chosen such that

$$M\cdot k = (M^{(1)} + M^{(2)})\cdot k = 0 \tag{3.7}$$

It follows that

$$\frac{1}{e}M^{(2)}\cdot k = -\frac{1}{e}M^{(1)}\cdot k = \mathcal{A}(s_f;\delta;0) - \mathcal{A}(s_i;0;\delta')$$

$$\begin{aligned}
\mathcal{A}(s_i;0;\delta') &= \mathcal{A}(\bar{s};0;0) + Q\cdot k\frac{\partial\mathcal{A}}{\partial s} + 2q'\cdot k\frac{\partial\mathcal{A}}{\partial\delta'} \\
\mathcal{A}(s_f;\delta;0) &= \mathcal{A}(\bar{s};0;0) - Q\cdot k\frac{\partial\mathcal{A}}{\partial s} - 2q\cdot k\frac{\partial\mathcal{A}}{\partial\delta}
\end{aligned}$$

Thus we obtain for $M^{(2)}\cdot k$

$$\begin{aligned}
\frac{1}{e}M^{(2)}\cdot k &= \{-2Q\frac{\partial\mathcal{A}}{\partial s} - 2q\frac{\partial\mathcal{A}}{\partial\delta} - 2q'\frac{\partial\mathcal{A}}{\partial\delta'}\}\cdot k \\
\frac{1}{e}M^{(2)} &= \{-2Q\frac{\partial\mathcal{A}}{\partial s} - 2q\frac{\partial\mathcal{A}}{\partial\delta} - 2q'\frac{\partial\mathcal{A}}{\partial\delta'}\}
\end{aligned} \tag{3.8}$$

Similarly, expanding $M^{(1)}$ leads to

$$\begin{aligned}
\frac{1}{e}M &= \frac{1}{e}M^{(1)} + \frac{1}{e}M^{(2)} \\
&= \frac{q'}{q'\cdot k}\{\mathcal{A}(\bar{s};0;0) + Q\cdot k\frac{\partial\mathcal{A}}{\partial s} + 2q'\cdot k\frac{\partial\mathcal{A}}{\partial\delta'}\} \\
&\quad - \frac{q}{q\cdot k}\{\mathcal{A}(\bar{s};0;0) - Q\cdot k\frac{\partial\mathcal{A}}{\partial s} - 2q\cdot k\frac{\partial\mathcal{A}}{\partial\delta}\} \\
&\quad - (p+q+p'+q')\frac{\partial\mathcal{A}}{\partial s} - 2q\frac{\partial\mathcal{A}}{\partial\delta} - 2q'\frac{\partial\mathcal{A}}{\partial\delta'} \\
&= (\frac{q'}{q'\cdot k} - \frac{q}{q\cdot k})\mathcal{A}(\bar{s};0;0) \\
&\quad + (\frac{p'\cdot k}{q'\cdot k}\,q' - p' + \frac{p\cdot k}{q\cdot k}\,q - p)\frac{\partial\mathcal{A}}{\partial s} + O(k)
\end{aligned} \tag{3.9}$$

This amplitude is gauge-invariant up to order k^0. Notice that in the limit $k \to 0$, the first two terms are determined by $\mathcal{A}(\bar{s};0;0)$ and its derivative with respect to s. The derivatives with respect to the off-mass-shell parameters $\frac{\partial\mathcal{A}}{\partial\delta}$ and $\frac{\partial\mathcal{A}}{\partial\delta'}$ have cancelled out and M depends only on on-shell information. However, there is no estimate of the size of the higher order terms.

Attempts have been made to extend Low's theorem to higher photon energies [21,22,25,26,40] and to make statements about the possible size of higher order terms.

To this end let us define the following finite-difference ratios :

$$\begin{aligned} D_1\mathcal{A}(s;\delta;\delta') &= [\mathcal{A}(s;\delta;\delta') - \mathcal{A}(\bar{s};\delta;\delta')]/(s-\bar{s}) \\ D_2\mathcal{A}(s;\delta;\delta') &= [\mathcal{A}(s;\delta;\delta') - \mathcal{A}(s;0;\delta')]/\delta \\ D_3\mathcal{A}(s;\delta;\delta') &= [\mathcal{A}(s;\delta;\delta') - \mathcal{A}(s;\delta;0)]/\delta' \end{aligned} \tag{3.10}$$

Expanding the strong amplitude in terms of these ratios instead of a Taylor series expansion leads to the result

$$\begin{aligned} \frac{1}{e}M &= (\frac{q'}{q'\cdot k} - \frac{q}{q\cdot k})\mathcal{A}(\bar{s};0;0) \\ &\quad + (\frac{p\cdot k}{q\cdot k}\,q - p)D_1\mathcal{A}(s_f;\delta;0) \\ &\quad + (\frac{p'\cdot k}{q'\cdot k}\,q' - p')D_1\mathcal{A}(s_i;0;\delta') \end{aligned} \tag{3.11}$$

In the limit $k \to 0$ the finite-difference ratio D_1 becomes $\frac{\partial}{\partial s}$ and we recover our earlier result. Unlike equation 3.9, however, this amplitude is gauge-invariant to all orders of k, and hence for all k. Therefore, a discrepancy between data and the predictions of this "hard-photon" theorem will come from radiation of the internal scattering structure, and experimental evaluation of properties such as the magnetic moment of the Δ^{++} will be possible.

In order to show that the result obtained in equation 3.11 is *not* unique, we have to go back and take a closer look at the parameterization of the strong interaction amplitude. We had defined $\mathcal{A}$ as a function of s, δ and δ', but in fact, due to the freedom in the off-shell behaviour we can define a more general amplitude $\mathcal{T}$ as

$$\mathcal{T}(\nu;\delta;\delta') = \mathcal{A}(\nu - a\delta - b\delta';\delta;\delta') \tag{3.12}$$

where a and b are arbitrary constants. Figure 4 attempts to show what is being done here. Our expansion point which is on-shell is indicated by ν_0. The off-shell point $(\nu,\delta,0)$ is indicated by X_1. What the difference ratios allow us to do is to relate

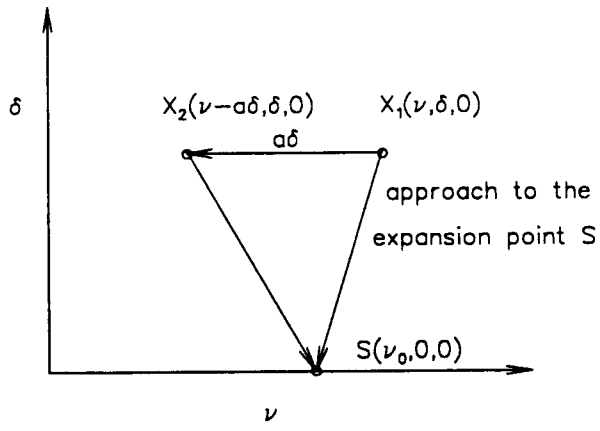

Figure 4. The problem of describing the off-shell behaviour of the strong amplitude.

the amplitude X_1 to the expansion point ν_0 as is shown by the arrow. However, the off-shell behaviour of the strong amplitude is not directly accessible to experiment and a reparameterization such as in equation 3.12 is possible. This effectively moves the point X_1 to the position $X_2 = (\nu - a\delta, \delta, 0)$ and our approach to the expansion point ν_0 has changed. The amplitude at X_1 can not be related to the amplitude at X_2 without an explicit model for the off-shell behaviour of $\mathcal{A}(s;\delta;\delta')$.

Expansion about the point $\nu_0 = \bar{s}$ yields the following results :

$$\begin{aligned} \nu_i &= \nu_0 + Q\cdot k + 2bq'\cdot k \\ \nu_f &= \nu_0 - Q\cdot k - 2aq\cdot k \end{aligned}$$

Note that

$$\begin{aligned} \mathcal{T}(\nu_0;0;0) &= \mathcal{A}(\bar{s};0;0) \\ \mathcal{T}(\nu_f;\delta;0) &= \mathcal{A}(s_f;\delta;0) \\ \mathcal{T}(\nu_i;0;\delta') &= \mathcal{A}(s_i;0;\delta') \end{aligned}$$

but

$$\mathcal{T}(\nu_f;0;0) = \mathcal{A}(\nu_f;0;0) \neq \mathcal{A}(s_f;0;0)$$

etc.

Following the by now familiar path with difference ratios defined as

$$\begin{aligned} D_1'\mathcal{T}(\nu;\delta;\delta') &= [\mathcal{T}(\nu;\delta;\delta') - \mathcal{T}(\nu_0;\delta;\delta')]/(\nu-\nu_0) \\ D_2'\mathcal{T}(\nu;\delta;\delta') &= [\mathcal{T}(\nu;\delta;\delta') - \mathcal{T}(\nu;0;\delta')]/\delta \\ D_3'\mathcal{T}(\nu;\delta;\delta') &= [\mathcal{T}(\nu;\delta;\delta') - \mathcal{T}(\nu;\delta;0)]/\delta' \end{aligned} \tag{3.13}$$

we find

$$\begin{aligned} \frac{1}{e}M &= (\frac{q'}{q'\cdot k} - \frac{q}{q\cdot k})\mathcal{T}(\nu;0;0) \\ &\quad + (\frac{p\cdot k}{q\cdot k}\,q - p)D_1'\mathcal{T}(\nu_f;\delta;0) \\ &\quad + (\frac{p'\cdot k}{q'\cdot k}\,q' - p')D_1'\mathcal{T}(\nu_i;0;\delta') \end{aligned} \tag{3.14}$$

Again, in the limit $k \to 0$ we recover Low's result 3.9 valid up to order k^0. It is different, however, from the hard-photon theorem in equation 3.11, since the finite-difference ratios are not the same. One can show that the difference between expressions 3.11 and 3.14 to order k is

$$[a(p\cdot k\, q - q\cdot k\, p) - b(p'\cdot k\, q' - q'\cdot k\, p')]\frac{\partial^2\mathcal{T}}{\partial s^2}$$

Since a and b are arbitrary constants, it is possible to have an arbitrary difference between these "hard-photon" theorems for terms of order k and higher. In fact, the presence of a resonance such as the Δ^{++} and the implied strong dependence of the amplitude on energy serves to amplify this ambiguity.

An example of how well soft/hard-photon theorems do on data was given in figure 1.

Chapter 4

Dynamically Consistent Models

It is clear from the previous chapter that an essential ingredient is missing in the definition of the bremsstrahlung amplitude. This ingredient is dynamical consistency or unitarity. In fact, we will see that the definition of a magnetic moment for a strongly decaying particle such as the Δ requires this consistency. Unitarity, like gauge invariance, relates diagrams of different order in the coupling constants and therefore implies a non-trivial constraint on the amplitude.

Our discussion will follow the developments in reference [42] with some simplifications, which will allow us to get an intuitive feeling for the important new features without getting muddled in too much detail. The starting point will be the coupling of the pion and proton to a bare delta isobar with spin $\frac{3}{2}$, isospin $\frac{3}{2}$ according to

$$\mathcal{L}_{\pi N\Delta} = \frac{g_\Delta}{2m}\overline{\Delta_\mu}(x)N(x)\partial^\mu\pi(x) + H.c. \tag{4.1}$$

where Δ, N, and π are the delta, nucleon and pion fields, respectively. The driving term is the Born amplitude for the graph of figure 5 and can be written as

$$\overline{u_f}V_\Delta u_i = (\frac{g_\Delta}{2m})^2\overline{u_f}q'_\mu[H^{-1}_{\Delta 0}(p)]^{\mu\nu}q_\nu u_i \tag{4.2}$$

where u_i and u_f are the initial and final Dirac spinors for the nucleon, q^μ and q'^μ are the initial and final pion four-momenta, p^μ is the total (or Δ) four-momentum, m is the proton mass, g_Δ is the $\pi N\Delta$ coupling strength and $H_{\Delta 0}$

$$H^{\mu\nu}_{\Delta 0} = (-g^{\mu\nu} + \gamma^\mu\gamma^\nu)(\not{p} - M) + p^\mu\gamma^\nu - \gamma^\mu p^\nu \tag{4.3}$$

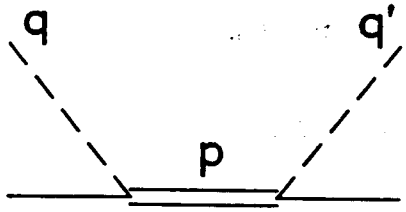

Figure 5. The elementary $\pi N\Delta$ interaction graph. The incoming and outgoing pion momenta are labeled q and q' (dashed lines), the intermediate Δ momentum p (double line), and the proton is denoted with solid lines.

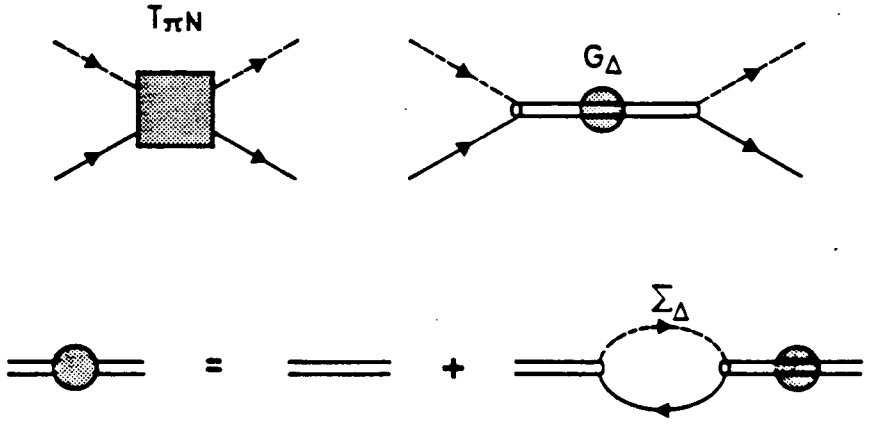

Figure 6. πN scattering in the isobar model.

yields the *free* Δ propagator [7]. In equation 4.3, M is the Δ - isobar mass (M = 1231.8 MeV) and $\not{p}$ refers to the scalar four-vector product $p \cdot \gamma = p^{\mu}\gamma_{\mu}$. The full T matrix is defined through the Bethe-Salpeter equation

$$T_{\Delta}(p,q',q) = V_{\Delta}(p,q',q) + \int \frac{d^4k}{(2\pi)^4} V_{\Delta}(p,q',k)G(p,k)T_{\Delta}(p,k,q) \qquad (4.4)$$

which sums up a unitary set of graphs and thus dynamically introduces the Δ decay width (see figure 6).

Since V_{Δ} is separable, T_{Δ} can be found in closed form :

$$T_{\Delta} = (\frac{g_{\Delta}}{2m})^2 q'_{\mu}[H_{\Delta}^{-1}(p)]^{\mu\nu}q_{\nu}, \qquad (4.5)$$

where the full propagator is derived from

$$H_\Delta(p) = H_{\Delta 0}(p) - (\frac{g_\Delta}{2m})^2 \Sigma(p) \tag{4.6}$$

The self-energy $\Sigma(p)$ is a complex function of momentum

$$\Sigma^{\mu\nu}(p) = \int \frac{d^4k}{(2\pi)^4} k^\mu G(p,k) k^\nu \tag{4.7}$$

$$G(p,k) = \frac{i}{k^2 - \mu^2 + i\epsilon} \frac{i}{\not p - \not k - m + i\epsilon} \tag{4.8}$$

with μ as the pion mass. The real part of Σ can be lumped together with the bare Δ mass to give the mass M of the *physical* Δ, while the imaginary part of Σ is responsible for preserving unitarity.

Dynamical consistency between the π^+p scattering and bremsstrahlung amplitudes implies that the magnetic moment of the bare delta, $\mu_{\Delta^{++}}$, will undergo the same kind of renormalization as was just described for the mass of the delta. The magnetic moment of the physical Δ, $\widetilde{\mu_{\Delta^{++}}}$, will be a complex function of momentum. The real part can once again be lumped together with the bare Δ magnetic moment to give us an effective $\mu^{eff}_{\Delta^{++}}$, which looks just like the parameter which was introduced in the tree approximation in earlier isobar models [11,20,30]. The imaginary part of $\widetilde{\mu_{\Delta^{++}}}$, however, is not represented in those models and it is a crucial ingredient in maintaining dynamical consistency as one goes from elastic to radiative π^+p scattering. Figure 7 shows $\Re\widetilde{\mu_{\Delta^{++}}}$ and $\Im\widetilde{\mu_{\Delta^{++}}}$ as a function of energy [41]. In the next section, we will discuss the results from this kind of calculation and compare them to experimental data.

4.1 Model Calculations

To date there exist two models for π^+p bremsstrahlung which satisfy gauge invariance, unitarity and the soft-photon theorem of Low.

The first such calculation was performed by the group from MIT [41]. The model is non-relativistic and makes use of various forms of structure functions to describe the $\pi p\Delta$ vertex. The approach stresses the importance of interaction currents

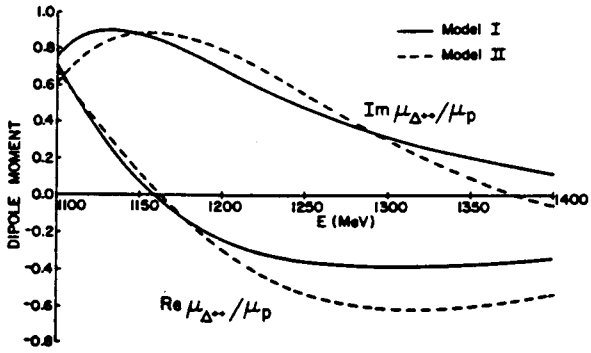

Figure 7. Energy dependence of the effective dipole moment $\widetilde{\mu_{\Delta^{++}}}$. The calculations are taken from reference [41]. Models I and II refer to different parameterizations of the elastic $\pi^+ p$ scattering amplitude.

at the vertex, which are needed to make the theory gauge invariant. Corrections are added to the formalism to account for the relativistic motion of the pion.

The second model was done at TRIUMF [42] and is fully relativistic. Phenomenological vertex functions are avoided through the use of a K-matrix type approach, where only the imaginary parts of Σ and $\widetilde{\mu_{\Delta^{++}}}$ are calculated.

In both models, free parameters are fitted to elastic $\pi^+ p$ scattering data. The only free parameters left as one goes from elastic scattering to bremsstrahlung are the magnetic moments of the Δ^{++}.

In the figures 8 to 17, we compare cross sections and asymmetries for both models for the values of $\mu_{\Delta^{++}}$ which best describe available experimental data [43, 45]. Those values are listed in table 1. The value for the TRIUMF model results from a fit to the measured cross section, the MIT value from a fit to the measured asymmetry.

Figure 17 shows a comparison of the predictions for the asymmetry alone and where we chose to put our photon detectors in this experiment.

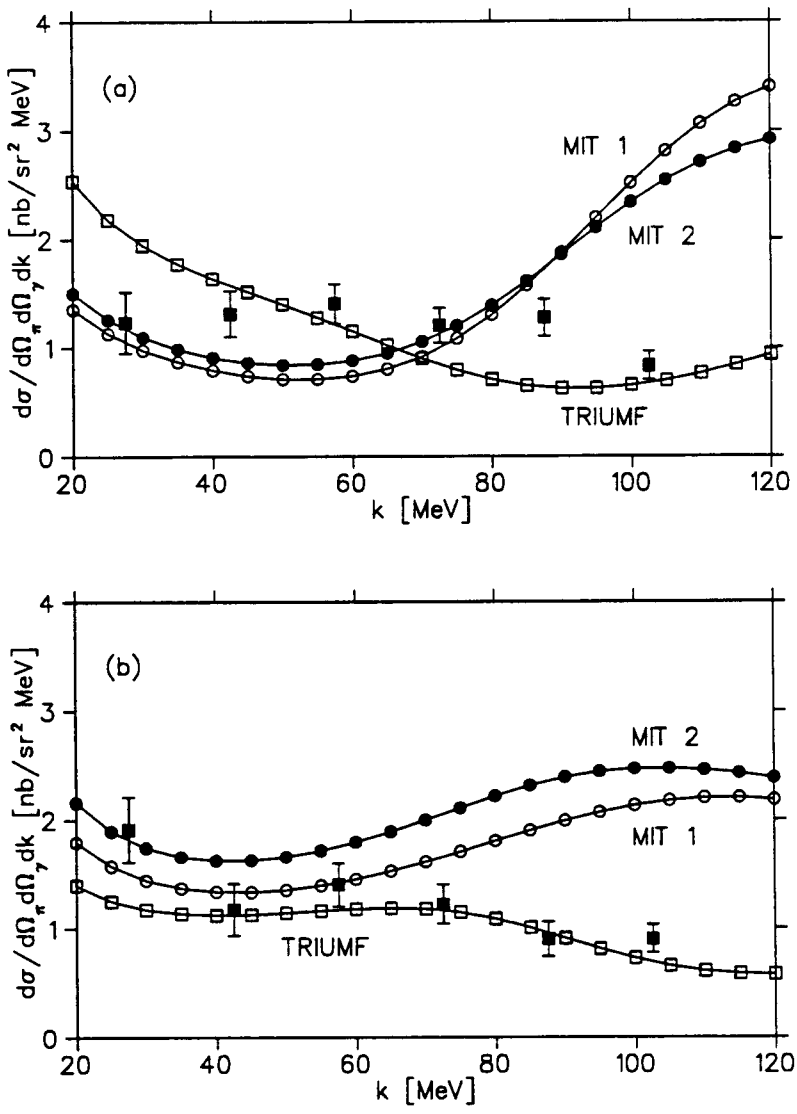

Figure 8. Comparison of the MIT and TRIUMF predictions for the cross section to experimental data. The theoretical error on the cross section can be as large as $\pm 0.2 \frac{\text{nb}}{\text{sr}^2\,\text{MeV}}$ at high photon energies depending on the choice of the delta magnetic moment. Figure (a) shows data for $\alpha_\pi = -63°$, figure (b) for $\alpha_\pi = -83°$ and $\alpha_\gamma = 119°$, $T_0 = 299\,\text{MeV}$ in a coplanar geometry.

Model	$\mu_{\Delta^{++}}/\mu_p$
TRIUMF [42]	2.3 ± 0.4
MIT [45]	$1.62 \pm 0.18 \pm 0.16$

Table 1. Value for the parameter $(\mu_{\Delta^{++}}/\mu_p)$ which best fits the available experimental data for each model. The first uncertainty is experimental, the second theoretical.

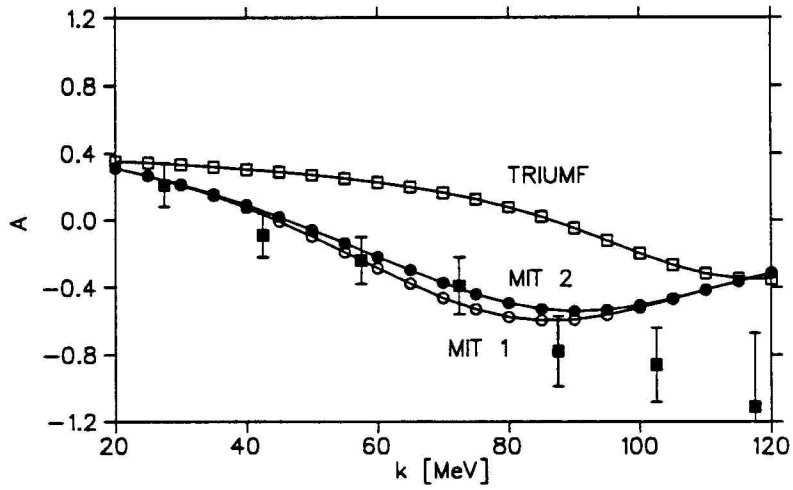

Figure 9. Comparison of the MIT and TRIUMF predictions for the asymmetry to experimental data. $\alpha_\pi = -89°$, $\alpha_\gamma = 119°$, and $T_0 = 298$ MeV in a coplanar geometry.

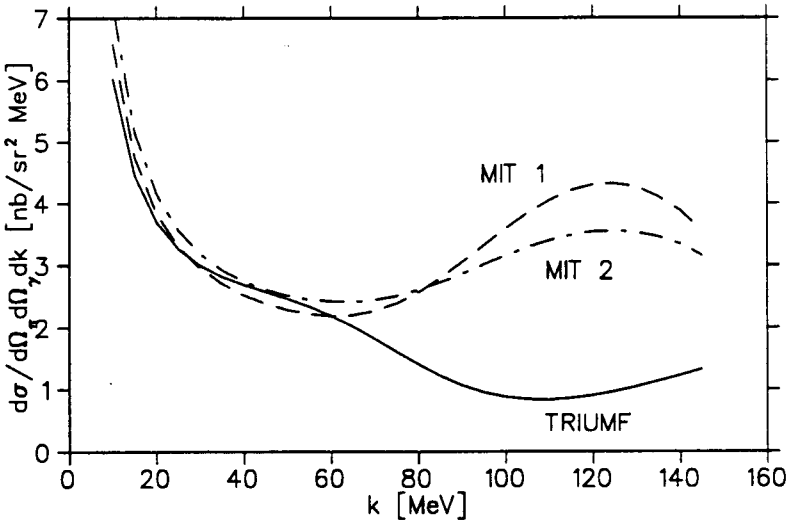

Figure 10. Predictions for the cross section as function of photon energy for $\alpha_\pi = -75°$ and $\alpha_\gamma = 105°$.

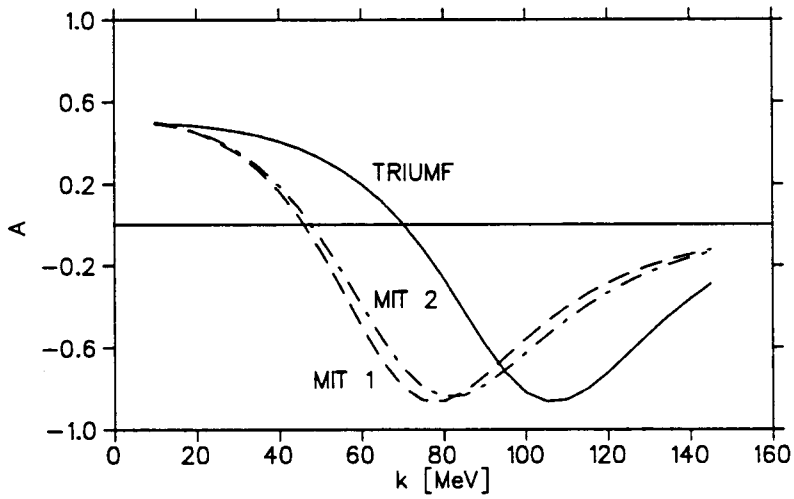

Figure 11. Predictions for the asymmetry as function of photon energy for $\alpha_\pi = -75°$ and $\alpha_\gamma = 105°$.

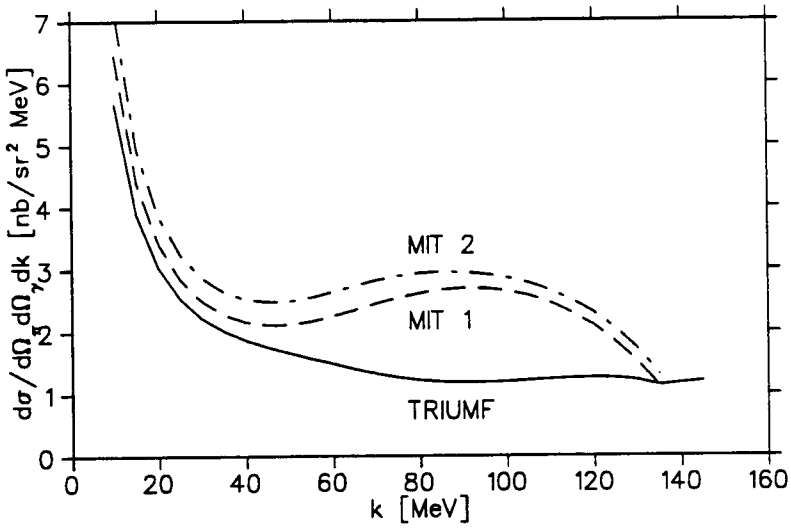

Figure 12. Predictions for the cross section as function of photon energy for $\alpha_\pi = -75°$ and $\alpha_\gamma = 150°$.

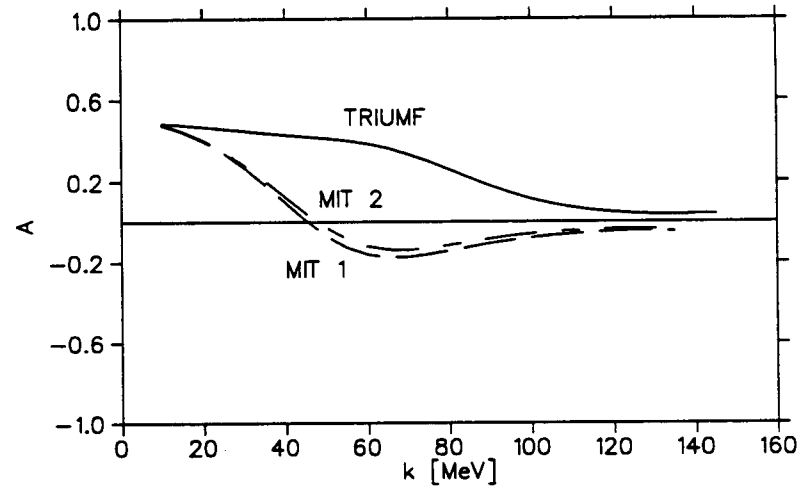

Figure 13. Predictions for the asymmetry as function of photon energy for $\alpha_\pi = -75°$ and $\alpha_\gamma = 150°$.

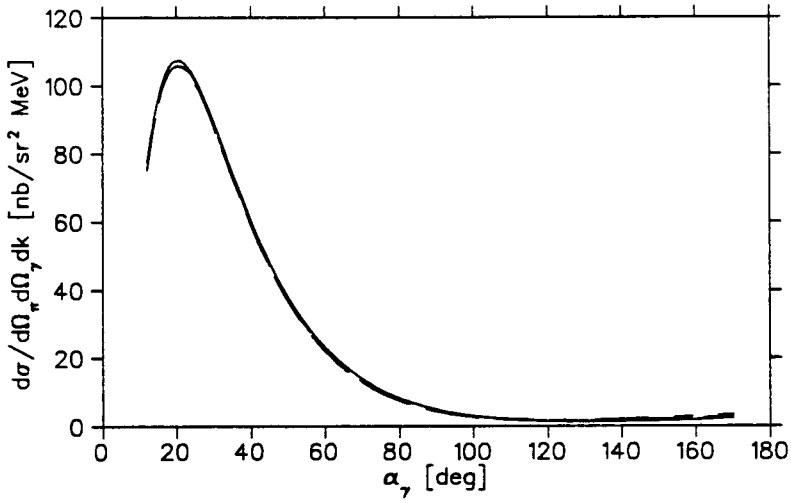

Figure 14. Predictions for the cross section as function of photon angle for $\alpha_\pi = -75°$ and $k_\gamma = 50$ MeV.

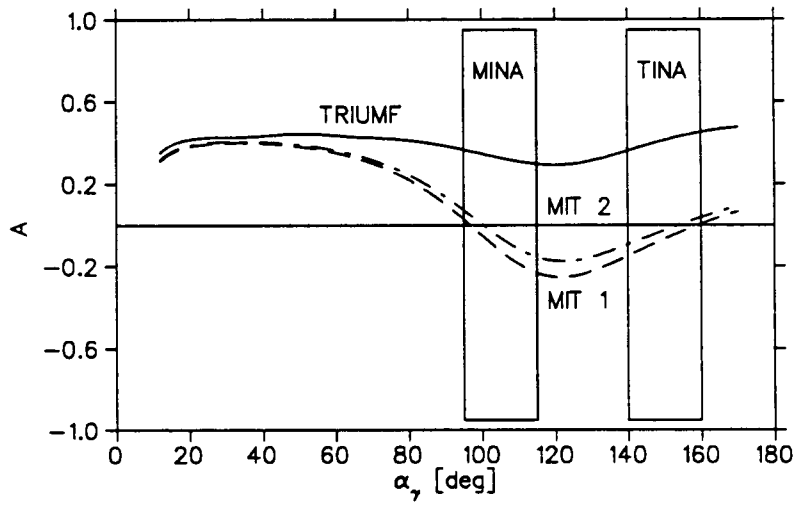

Figure 15. Predictions for the asymmetry as function of photon angle for $\alpha_\pi = -75°$ and $k_\gamma = 50$ MeV. The boxes indicate the positions and angular acceptances for the photon detectors TINA and MINA in this experiment.

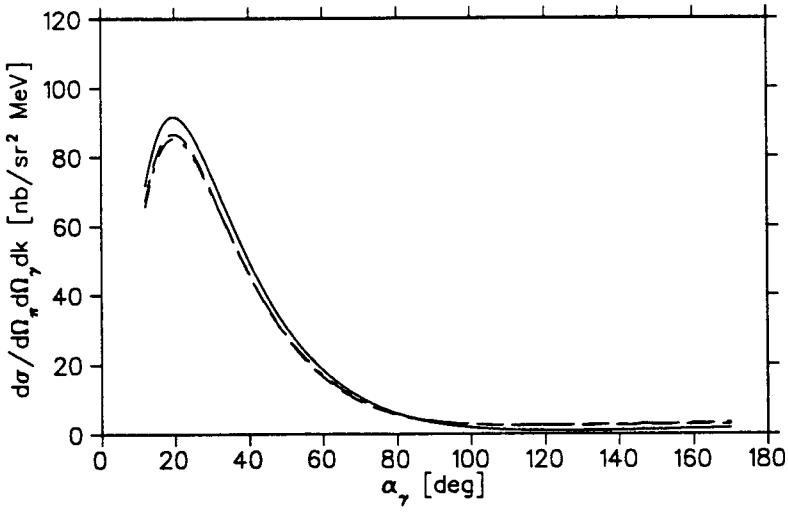

Figure 16. Predictions for the cross section as function of photon angle for $\alpha_\pi = -75°$ and $k_\gamma = 80$ MeV.

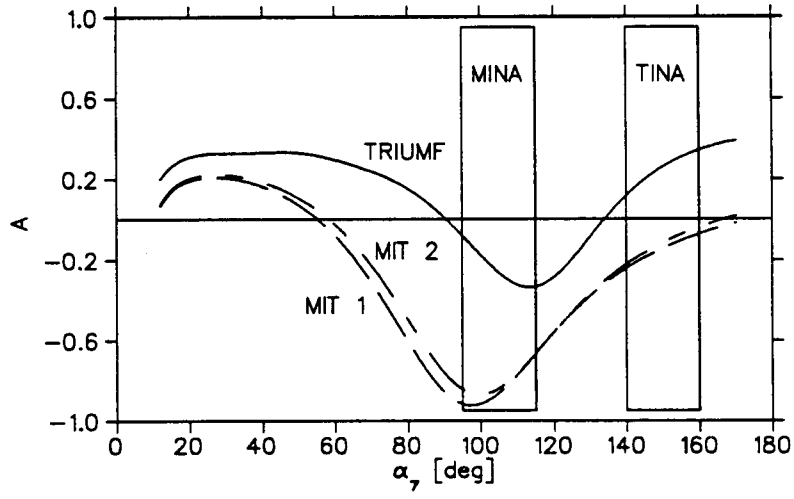

Figure 17. Predictions for the asymmetry as function of photon angle for $\alpha_\pi = -75°$ and $k_\gamma = 80$ MeV. The boxes indicate the positions and angular acceptances for the photon detectors TINA and MINA in this experiment.

Part II

Experiment

Chapter 5

Introduction

This story begins in the summer of 1986 when our group at Oregon decided to propose an experiment to measure the asymmetry in pion-proton bremsstrahlung at the TRIUMF cyclotron facility. With a growing interest among the scientists at TRIUMF and encouragement from the Experimental Evaluation Committee (EEC) a collaboration was formed in the winter of 1987 and the design and construction of detector equipment began soon afterwards. The year of 1988 was spent building.

PACMAN, which is a large dipole magnet, was chosen for use as a pion spectrometer and equipped with magnetic field clamps and drift chambers. The OSU part of the group contributed an array of plastic scintillators for the detection of protons. Extensive modifications had to be made to the TRIUMF frozen spin target and to three large NaI crystals, TINA, MINA and ALBERTA.

The experiment got its first beam time in the month of January of 1989, but technical difficulties as well as delays in the completion of the drift chambers turned this period of data taking into a prototype and development run. After a shutdown of two months, data were taken for two more weeks at the beginning of April.

The analysis has been slow and after 3 years of detective work, it is now clear that the experiment has failed. A high beam-related accidental coincidence rate together with calibration problems for two detector subsystems (the plastic scintillator array and the NaI crystals) make it impossible to extract the bremsstrahlung signal from the data.

There seems to be little point in presenting this thesis in the traditional format showing a clear path from the data to the result, given that there is no result. Instead, an attempt is made to develop generally applicable concepts from the experience of running this experiment.

Chapter 6

The Goal of the Experiment

The goal is, naturally, to carry out a measurement which has never been carried out before and which has the potential to reveal new hitherto unknown physics or to confirm or to refute existing theoretical models. Both questions, regarding uniqueness and relevance, can only be answered within the context of currently available technology and advances in physics theory.

The state of the art in the theory of pion-proton bremsstrahlung is represented by two models, denoted by MIT [41] and TRIUMF [42], respectively, which give predictions for both the cross section and the asymmetry. The results for the cross section are quite similar in both models, which is not too surprising, since in both cases the model parameters have been fitted to experimental data from a series of experiments done in the 1970s by a group from UCLA [17,29,32].

The decision to mount another experiment is based on the observation that predictions for the asymmetry are quite sensitive to the assumptions which go into the theory. This is shown in section 4.1 where results from the MIT model are compared to results from TRIUMF. In order to confirm or refute one or the other of the two models experimentally, detectors should be placed at photon angles where predictions differ the most (see figure 17, page 25). Furthermore, the wish to distinguish between two hypotheses puts limits on the allowed error of the measurement, namely

$$\delta m \leq \frac{1}{2}(m_1 - m_0)$$

δ **m** = allowed measurement error

$\mathbf{m}_{1,0}$ = values of the variable to be measured as predicted by hypothesis 1 and 0, respectively

One should realize here that **m** denotes a "measurement" which is really an average over some acceptance bin times a number associated with the resolution of the detector. In the case of bremsstrahlung, where **m** depends on five variables, this acceptance bin is given by

$$\Delta p = (\Delta\Omega_\pi)(\Delta\Omega_\gamma)(\Delta E_\gamma)$$

where $\Delta\Omega_{\pi,\gamma}$ are the solid angle acceptances per data point for pion and photon, respectively, and ΔE_γ is of the order of the photon energy resolution.

Let us look at the effect of averaging over Δp. We are concerned with

$$\begin{aligned} \sigma(p_0) &= \frac{1}{\Delta p}\int_{\Delta p} dp'\sigma(p') \\ \mathcal{A}(p_0) &= \frac{1}{\Delta p}\frac{1}{\sigma(p_0)}\int_{\Delta p} dp'\sigma(p')\mathcal{A}(p') \end{aligned} \tag{6.1}$$

with the results for our two theoretical models listed in tables 2 (for TINA, $\alpha_\gamma = 150°$) and 3 (for MINA, $\alpha_\gamma = 105°$). We compare the point calculations of $\sigma = \frac{d^5\sigma}{d\Omega_\pi d\Omega_\gamma dk}$ and $\mathcal{A}$ to the same averaged over the acceptance bin

$$\begin{aligned} \Delta\mathbf{p} = {} & (\Delta\alpha_\pi = 10°)(\Delta\beta_\pi = 10°) \\ & (\Delta\alpha_\gamma = 20°)(\Delta\beta_\gamma = 20°) \\ & (\Delta k = 10 \text{ MeV or } 20 \text{ MeV}). \end{aligned}$$

The central values are given by

$$T_0 = 265 \text{ MeV} \qquad \alpha_\pi = -75° \qquad \beta_\pi = \beta_\gamma = 0°$$

and the photon energy is listed in the tables. The cross section is calculated based on the first term in the Low expansion and the asymmetries are taken from MIT and TRIUMF model calculations. The MIT model allows for two distinct parameterizations of the elastic scattering ampitude. We have chosen to work with a set of parameters which is refered to as model 1 in reference [41].

The statistical errors for $\sigma(p_0)$ and $\mathcal{A}(p_0)$, which arise because we have used a Monte Carlo method to do the averaging over the acceptance bin, are negligible.

As one might have expected, $\sigma(p_0)$, $\mathcal{A}(p_0)$ and $\Delta\mathcal{A}$ depend on the choice of Δp and it will be shown in chapter 14 that the detector resolution also plays a role here.

For now let us choose an upper bound for the measurement error of the asymmetry $\mathcal{A}$

$$\delta\mathcal{A} \leq \frac{1}{2} |\mathcal{A}_{MIT} - \mathcal{A}_{TRIUMF}|$$

There is some freedom left for subjective judgement, of course, and the value for $\delta\mathcal{A}$ which was chosen for this experiment was

$$\delta\mathcal{A} \text{ (desired)} \leq 0.1$$

Before we end this section, we still have to ask whether our experiment is unique. In fact, while we were busy designing and building new detectors at TRIUMF, a very similar experiment was underway at the Paul-Scherer-Institute in Switzerland [44,45] to measure the asymmetry for a narrow range of pion angles. We have carefully selected our experimental configuration to complement the acceptance of the PSI experiment. The coverage of pion and photon angles for both experiments is shown in figure 18.

To summarize : the goal of this experiment is to measure the asymmetry in pion-proton bremsstrahlung with an acuraccy of

$$(\delta\mathcal{A})_{desired} \leq 0.1$$

over the following acceptance

$$\begin{aligned} \Delta\alpha_\pi &= \text{-60 ...-90 degrees} \\ \Delta\alpha_\gamma &= (105, 150) \pm 10 \text{ degrees} \end{aligned}$$

based on an analysis of available theoretical predictions.

The question now is, whether this program can be realized.

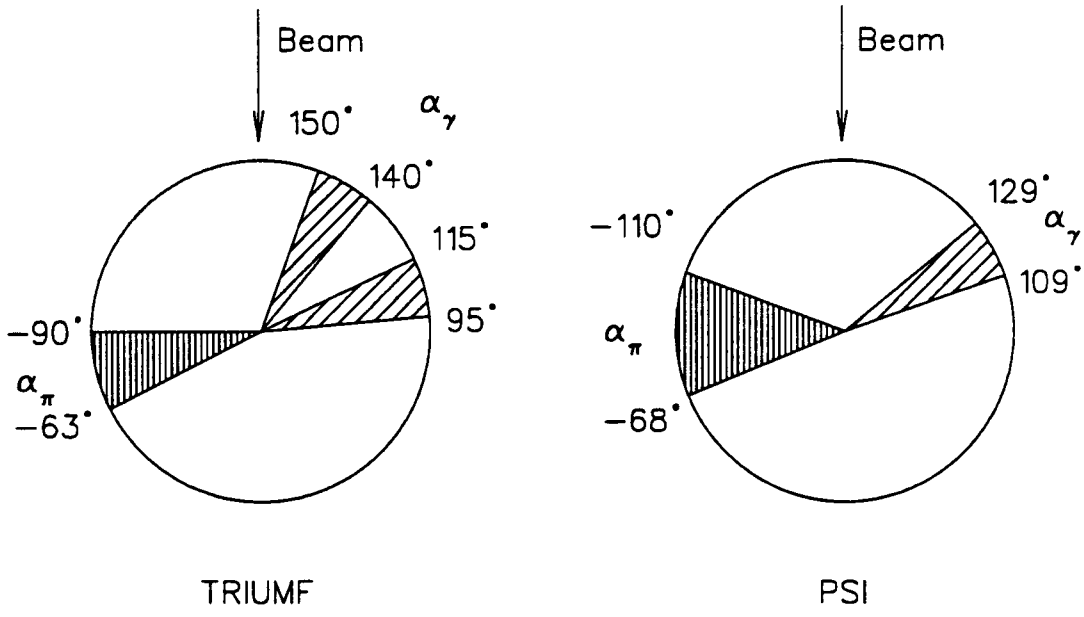

Figure 18. A comparison of the acceptance coverage for the TRIUMF and PSI experiments.

k in MeV		35	45	55	65	75	85	95	105	115	125
Point	σ	2.486	2.245	2.177	2.206	2.266	2.349	2.360	2.331	2.188	1.875
	A_{MIT}	0.184	0.008	-0.127	-0.176	-0.161	-0.125	-0.093	-0.069	-0.053	-0.045
	A_{TRIUMF}	0.439	0.421	0.400	0.362	0.298	0.217	0.143	0.089	0.057	0.041
	ΔA	-0.255	-0.413	-0.527	-0.538	-0.459	-0.342	-0.236	-0.158	-0.110	-0.086
Δk = 10 MeV	σ	2.678	2.428	2.324	2.298	2.309	2.315	2.310	2.235	2.068	1.753
	A_{MIT}	0.183	0.011	-0.121	-0.173	-0.162	-0.128	-0.095	-0.070	-0.054	-0.046
	A_{TRIUMF}	0.431	0.413	0.392	0.353	0.288	0.208	0.137	0.086	0.055	0.038
	ΔA	-0.248	-0.402	-0.513	-0.526	-0.450	-0.336	-0.232	-0.156	-0.109	-0.084
Δk = 20 MeV	σ	2.552		2.311		2.312		2.273		1.911	
	A_{MIT}	0.100		-0.147		-0.145		-0.083		-0.051	
	A_{TRIUMF}	0.423		0.373		0.248		0.112		0.047	
	ΔA	-0.323		-0.520		-0.393		-0.195		-0.098	

Table 2. The cross section and asymmetry averaged over the acceptance bin for TINA.

k in MeV		35	45	55	65	75	85	95	105	115	125
Point	σ	2.190	1.943	1.809	1.750	1.736	1.718	1.750	1.723	1.698	1.659
	A_{MIT}	0.268	0.033	-0.305	-0.663	-0.858	-0.814	-0.647	-0.474	-0.339	-0.241
	A_{TRIUMF}	0.434	0.372	0.271	0.114	-0.119	-0.422	-0.719	-0.863	-0.800	-0.627
	ΔA	-0.166	-0.339	-0.576	-0.777	-0.739	-0.392	0.072	0.389	0.461	0.386
Δk = 10 MeV	σ	2.436	2.148	1.993	1.913	1.849	1.803	1.775	1.729	1.690	1.633
	A_{MIT}	0.266	0.041	-0.278	-0.611	-0.811	-0.802	-0.662	-0.497	-0.359	-0.257
	A_{TRIUMF}	0.429	0.368	0.270	0.120	-0.100	-0.380	-0.648	-0.794	-0.769	-0.633
	ΔA	-0.163	-0.327	-0.548	-0.731	-0.711	-0.422	-0.014	0.297	0.410	0.376
Δk = 20 MeV	σ	2.290		1.953		1.826		1.752		1.661	
	A_{MIT}	0.159		-0.442		-0.806		-0.580		-0.308	
	A_{TRIUMF}	0.400		0.196		-0.238		-0.719		-0.702	
	ΔA	-0.241		-0.638		-0.568		0.139		0.394	

Table 3. The cross section and asymmetry averaged over the acceptance bin for MINA.

Chapter 7

Signal and Background

Before we get into a discussion of data analysis techniques and how this affects the design of the experiment, let us define some terms and the context within which these terms apply.

Particle physics experiments are counting experiments, meaning that the essential task is to count the number of events which satisfy a given set of conditions. Typically a beam of particles hits a designated target and the detectors surrounding the target pick up the fragments resulting from the collision (figure 19). The design of the detectors is driven by the kind of information one needs to know about the fragments. "Data analysis" then takes this information as input, subjects it to a set of conditions (kinematics, particle identification etc., collectively known as "analysis cuts") and then either accepts or rejects the event. The final result is the number of events which were accepted. The "signal" (S) is the fraction of events which were actually associated with the physics process of interest (e.g. bremsstrahlung), whereas the remaining events are associated with random (N) or kinematically similar processes (Q) (e.g. bremsstrahlung on a nucleus rather than a proton). These events can not be distinguished from the signal events based on the chosen set of conditions and are known collectively as "background".

Furthermore, we know only the probability with which a certain event can occur and therefore both the signal S and the background ($Q + N$), or rather the total count ($S + Q + N$) have to be viewed as random variables with an associated

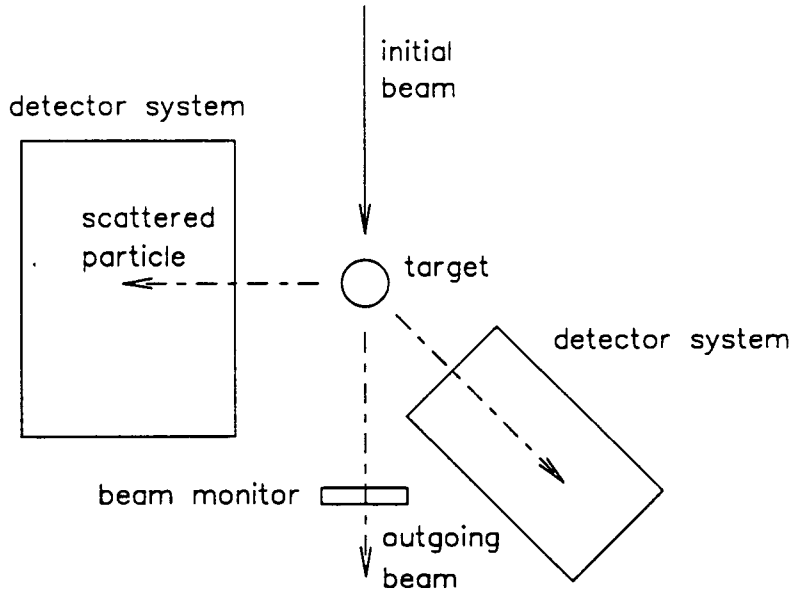

Figure 19. Layout of a typical particle physics experiment with a fixed target.

"distribution" function. In particle physics we are only interested in the "Poisson" and the "Binomial" distributions and their common limit in the case of large numbers, the "Gaussian" distribution. These distributions are discussed in references [52] and [53] along with typical applications.

The two types of background, Q and N, have different origins and therefore need to be dealt with in different ways.

It is in the nature of accidental coincidence backgrounds that the reactions involved are independent from each other. We can therefore "measure" this contribution by forming coincidences between event signatures which are "out of time", e.g. a π^+p event in coincidence with a photon which is removed in time from the π^+p event by more than some interval $\Delta\tau$. Since the sources responsible for this signature are uncorrelated, we know that the same number of events contributes to our total in-time event count $(S+Q+N)$. This is best shown by plotting the time distribution of these coincidences (figure 20). As one can see, we can determine N by analyzing the out-of-time coincidence in "exactly" the same manner as the in-time coincidences.

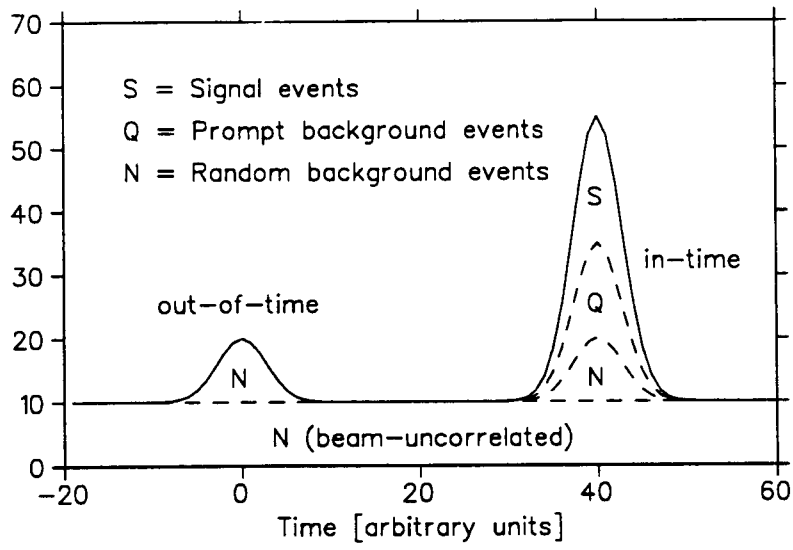

Figure 20. Time distributions for signal and background data.

Incidentally, in order to have the ability to estimate random background in this manner,

- the times of all detected particles have to be measured. The timing resolution of this measurement determines $\Delta\tau$.

- the data acquisition part of the experiment has to be designed in such a way that not only in-time coincidences but also out-of-time coincidences for all combinations of particles are accepted and stored for further analysis. In practise, this means that we consider events with a typical coincidence time $\Delta\tau_T$ which is a multiple of $\Delta\tau$ (in this experiment, we had $\Delta\tau_{\pi p} \approx \Delta\tau_{\pi\gamma} \approx 2\Delta\tau$, where $\Delta\tau = 43$ ns is a characteristic of the beam line).

The background Q, which is due to prompt processes which look like the real signal event, can not be estimated while we do the experiment. There are in general two contributions to Q :

- Reactions on the target particle, e.g. pion production ($\pi^+ p \rightarrow \pi^+ p\ \pi^0$) rather than bremsstrahlung. In the example, the kinematic signature for π^0 production can be easily distinguished from the bremsstrahlung kinematics due to

the mass of the π^0. In general this contribution to Q must be calculated.

- Reactions on various elements other than the target particle. In this experiment, our target - the TRIUMF frozen spin target (see chapter 11) - contains, besides free hydrogen, substantial amounts of helium, carbon, oxygen and heavier elements. Reactions on nuclei can easily mirror $\pi^+p \rightarrow \pi^+p\gamma$ kinematics (e.g. quasi-free bremsstrahlung). This contribution to Q "can" be measured by substituting the frozen spin target with another target which does "not" contain free hydrogen but is otherwise "equivalent". This implies that we have to repeat the bremsstrahlung experiment with a "dummy target" and provisions have to be made to make this possible.

In summary, there are two kinds of background : accidental background N, which can be measured by analysing out-of-time coincidences, and what we called kinematically similar background Q, which has to be either calculated or measured in a reference experiment with a dummy target. The amount of background $(N+Q)$ depends on how similar its signature is to the real signal event. "Similarity" here depends on the amount of information which is recorded by the experiment and the detector resolution, i.e. the accuracy with which kinematic variables are measured.

Chapter 8

Formal Definition of the Measured Cross Section and Asymmetry

The signal S can be calculated as follows :

$$\begin{aligned} S\,[\text{events}] &= F_B\left[\frac{\#}{\text{s cm}^2}\right]\cdot A\,[\text{cm}^2]\cdot t\,[\text{cm}]\cdot \rho\left[\frac{\text{g}}{\text{cm}^3}\right]\cdot N_A\left[\frac{\#}{\text{mol}}\right]/m_A\left[\frac{\text{g}}{\text{mol}}\right] \\ &\quad \cdot\overline{\frac{d\sigma}{dV}}\left[\frac{\text{cm}^2}{V}\right]\cdot \Delta V\,[V]\cdot\varepsilon(V)\cdot\Delta\tau\,[\text{s}] \end{aligned} \tag{8.1}$$

where

$[..]$	=	units associated with each quantity
F_B	=	Flux of beam particles
A	=	Target area hit by the beam
t	=	Target thickness
ρ	=	Target density, which is assumed to be constant over the target volume
N_A	=	Avogadro's number $6.022\cdot 10^{23}\frac{\#}{\text{mol}}$
m_A	=	Atomic number of the target material
$\overline{\frac{d\sigma}{dV}}$	=	Differential cross section averaged over acceptance
ΔV	=	Experimental acceptance per data point
ε	=	Experimental efficiency per data point, which might be a function of variables V (position, angle, momentum, etc.)

$\Delta\tau$ = Time interval during which data were taken by the experiment

V = the set of free variables on which the cross section depends. In the case of Bremsstrahlung, V might be chosen to be $\{ \alpha_\pi, \beta_\pi, \alpha_\gamma, \beta_\gamma, E_\gamma \}$ plus the initial beam energy and angles.

The product $F_B \cdot A \cdot t$ must be replaced for realistic conditions (where not all of these quantities are constant) by the integrated product

$$(F_B A t) = \int_A dx\, dy\, F_B(x,y)\, t(x,y)$$

assuming that the z-axis points along the direction of the beam.

In the presence of a target polarization, expression 8.1 changes to

$$S = (FAt)\,\rho\,\frac{N_A}{m_A}\,\frac{\overline{d\sigma}}{dV}\,\Delta V\,\varepsilon\,\Delta\tau\,(1+\overline{\mathcal{A}}\mathcal{P}) \tag{8.2}$$

where

$$\overline{\mathcal{A}} = \frac{\sigma_\uparrow - \sigma_\downarrow}{\sigma_\uparrow + \sigma_\downarrow}$$
$$\frac{\overline{d\sigma}}{dV} = \frac{1}{2}(\sigma_\uparrow + \sigma_\downarrow)$$

$\mathcal{A}$ is the asymmetry which we want to measure averaged over acceptance. $\sigma_\uparrow$ and $\sigma_\downarrow$ are the differential cross sections for the proton spin pointing up and down, respectively. The up-down axis is chosen normal to the scattering plane.

and

$$\mathcal{P} = \frac{M_\uparrow - M_\downarrow}{M_0}$$
$$M_0 = M_\uparrow + M_\downarrow$$

$\mathcal{P}$ is the target polarization. $M_\uparrow$ and $M_\downarrow$ are the numbers of target protons with spins pointing up and down, respectively. M_0 is the total number of free protons in the target.

If one lets $S_\uparrow = S(\mathcal{P} > 0)$ and $S_\downarrow = S(\mathcal{P} < 0)$, one gets with $P = |\mathcal{P}|$ and $P_\uparrow = P_\downarrow = P$

$$R = \frac{S_\uparrow - S_\downarrow}{S_\uparrow + S_\downarrow} = \mathcal{A}P \tag{8.3}$$

from which the quantity $\mathcal{A}$ can be determined.

Things are of course not that simple. Before we can determine $\mathcal{A}$ from a measurement of $\mathcal{P}$, $S_\uparrow$ and $S_\downarrow$, we have to discuss the remaining quantities in equation 8.2, which we have so easily dropped in equation 8.3.

In general, we have

$$\begin{aligned} S_\uparrow &= (FAt\Delta\tau)_\uparrow \, \rho_\uparrow \, \frac{N_A}{m_A} \, \overline{\frac{d\sigma}{dV}} \, \Delta V_\uparrow \, \varepsilon_\uparrow \, (1 + \mathcal{A}P_\uparrow) \\ S_\downarrow &= (FAt\Delta\tau)_\downarrow \, \rho_\downarrow \, \frac{N_A}{m_A} \, \overline{\frac{d\sigma}{dV}} \, \Delta V_\downarrow \, \varepsilon_\downarrow \, (1 - \mathcal{A}P_\downarrow) \end{aligned} \tag{8.4}$$

The asymmetry $\mathcal{A}$ now depends on many more variables and it is the task of the experimenter to measure and keep track of these quantities. This means that the accuracy of the measurement is already limited by our ability to monitor the variables appearing in equation 8.4, even before we worry about statistical errors, signal-to-background ratios and detector resolution functions.

Let's look at the bremsstrahlung experiment as a concrete example :

- F : The Flux is monitored indirectly with plastic scintillator counters. Statistical errors are negligible but systematic errors are estimated to be of the order of 1 % (which we will treat as a Gaussian error and add to the overall error in quadrature).

- $FAt\Delta\tau$: $\int_A Ft\Delta\tau \, dx \, dy = (R\Delta\tau) \cdot \mathit{constant}$. The rate is monitored as mentioned above and thus we can consider the remaining product (At) as constant.

- ρ : The target density has been measured to be $(0.59 \pm 0.004)\frac{\mathrm{g}}{\mathrm{cm}^3}$ but does not change with time. It therefore does not enter directly in the determination of $\mathcal{A}$. However, this error enters through the normalization of the empty-target run (which is needed to measure the prompt background Q).

- ΔV . is constant.

- P : $\frac{\delta P}{P}$ is estimated to be of order 4 %.

- ε : The "dead time" is the fraction of time during which the data acquisition part of the experiment is busy and cannot accept a new event. This introduces an inefficiency which is correlated with R, the beam rate, and may vary in time. Other contributions to the total ε are constant over time and cancel out in the expression for $\mathcal{A}$. The measurement error for the time-dependent part is $\frac{\delta\varepsilon}{\varepsilon} = 0.01 = 1\ \%$.

In summary, we have

$$S_{\uparrow\downarrow} = \alpha\,(R \cdot \Delta\tau)_{\uparrow\downarrow} \cdot \varepsilon_{\uparrow\downarrow} \cdot (1 \pm \overline{\mathcal{A}} P_{\uparrow\downarrow})\ .$$

where $\alpha = \frac{1}{R}(\int_A F t dA)\rho\frac{N_A}{m_A}\left(\overline{\frac{d\sigma}{dV}}\right)\Delta V$ is a constant and $\overline{\frac{d\sigma}{dV}}$ and $\overline{\mathcal{A}}$ are the theoretical predictions averaged over acceptance and detector resolution (see section 15.1).

Applying what we have learned about background, we can define our measurement of $S_{\uparrow\downarrow}$ as

$$S_{\uparrow\downarrow} = \left\{[(S+Q+N)-N] - \frac{1}{\beta}[(Q'+N')-N']\right\}_{\uparrow\downarrow} \tag{8.5}$$

where the first term indicates the subtraction of random background N and the second term does the same to the empty-target data, which allows a determination of the prompt background Q. β normalizes the empty-target run to the data-taking run and can be defined as

$$\beta = \frac{Q'}{Q} = \frac{(R\,\Delta\tau\,\varepsilon\,\rho)'}{(R\,\Delta\tau\,\varepsilon\,\rho)}$$

The measurement of $\overline{\mathcal{A}}$ is defined through

$$\overline{\mathcal{A}} \equiv A = \frac{2R}{(P_\uparrow + P_\downarrow) - (P_\uparrow - P_\downarrow)R} \tag{8.6}$$

$$R = \frac{X_\uparrow - X_\downarrow}{X_\uparrow + X_\downarrow - 2B} \tag{8.7}$$

where

$$X = \frac{S}{(R\,\Delta\tau\,\varepsilon)},\quad B = \frac{Q'}{(R\,\Delta\tau\,\varepsilon)'}\,\frac{\rho}{\rho'} \tag{8.8}$$

An expression for the error of $\mathcal{A}$, $\delta\mathcal{A}$, is derived in appendix G and leads to the upper limit

$$\begin{aligned}(\delta\mathcal{A})^2 \;\leq\; & \frac{1}{2P^2}\left\{\;\frac{1}{S_0}\left[(1+2\eta+4R_x)+2\beta\,(1+\eta+2R_x)\right]\right. \\ & +\left(1+2\eta+4\eta^2\right)\left[\left(\frac{\delta M}{M}\right)^2+\left(\frac{\delta\varepsilon}{\varepsilon}\right)^2\right] \\ & \left.+4\eta^2\left(\frac{\delta\rho}{\rho}\right)^2\;\right\} \\ & +\left(\frac{\delta P}{P}\right)^2 \\ =\; & (\delta\mathcal{A})^2_{max} \end{aligned} \tag{8.9}$$

where

$$\begin{aligned} M \;=\; (R\,\Delta\tau) \;&=\; (R\,\Delta\tau)_\uparrow = (R\,\Delta\tau)_\downarrow \\ &=\; \text{the number of beam particles on target} \\ S_0 \;&=\; \text{the expected number of events for an unpolarized target} \\ \eta \;=\; \tfrac{Q}{S_0} \;&=\; \text{kinematically similar (prompt) background} \\ R_x \;=\; \tfrac{N}{S_0} \;&=\; \text{random background for the data-taking run} \\ R'_x \;=\; \tfrac{N'}{\beta S_0} \;&=\; \text{random background for the empty-target run} \end{aligned}$$

and

$$\beta = \left(\frac{Q'}{Q}\right) = \sqrt{\frac{\eta+2R'_x}{1+\eta+2R_x}} \tag{8.10}$$

is the empty-target run normalization optimized for the most effective use of beam time $\Delta\tau_{total} \approx \Delta\tau\,(1+\beta)$ (taking flux and target density etc. as constant).

What can we learn from expression 8.9 ? Since we have already done the experiment, it simply tells us what the measurement error for the asymmetry will be. However, the designer of the experiment sees in this expression a number of complicated constraints which will have to be satisfied if the goal of the experiment $(\delta\mathcal{A}) \leq (\delta\mathcal{A})_{max} \leq (\delta\mathcal{A})_{desired} \lesssim 0.1$ is to be realized.

The values for $\left(\frac{\delta M}{M}\right)$, $\left(\frac{\delta\varepsilon}{\varepsilon}\right)$, $\left(\frac{\delta\rho}{\rho}\right)$ and $\left(\frac{\delta P}{P}\right)$, which are the monitoring errors for the beam on target, the analysis efficiency, the target density and the target po-

larization, respectively, are easily estimated. In this case we can take them directly from the bremsstrahlung experiment :

$$\begin{aligned} \left(\frac{\delta M}{M}\right) &= 0.01 \\ \left(\frac{\delta \epsilon}{\epsilon}\right) &= 0.01 \\ \left(\frac{\delta \rho}{\rho}\right) &= 0.007 \\ \left(\frac{\delta P}{P}\right) &= 0.04 \qquad\qquad P = 0.75 \end{aligned}$$

As has already been mentioned, the amount of background, η, R_x and R'_x, depends on a measure of "similarity", i.e. on the final analysis. Under certain assumptions, which are discussed in chapter 14 and appendix B, similarity as in a χ^2-fit depends directly on the detector resolution function. The above expression for $\delta\mathcal{A}_{max}$ therefore gives us design criteria for our experiment !

In order to estimate η and $R_x^{(\prime)}$, we have to look at a concrete experimental setup. Once the detector layout and the properties of the beam line and target have been studied, it is possible to identify specific background sources which will contribute to Q and N. Combined with a strategy to analyze the data, we can then calculate η and $R_x^{(\prime)}$ and draw conclusions about the required beam time $\Delta\tau$ and beam rate R.

What follows will be a brief introduction to our bremsstrahlung experiment, as it was actually designed, the M11 beam line, on which the experiment was run, and the frozen spin target. Once we have an understanding of what is involved, we will come back and identify the possible sources of background.

Chapter 9

The Experimental Setup

The detector layout for the TRIUMF bremsstrahlung experiment is shown in figure 21. It is the one with which we took data in April of 1989. This configuration was driven by a desire to work with a large three-body acceptance and all detector systems were designed from that point of view.

The TRIUMF frozen spin target (FST) [47] was equipped with a new set of Helmholtz coils which did allow access to scattering angles spanning almost 2π in the scattering plane. The magnetic field provided by these coils guaranteed a lifetime of about 200 hours for the polarization (see chapter 11 for details) which allowed us to take data undisturbed for 24 hours at a stretch. As we found out later, it also caused severe calibration problems for the photon and proton detectors, but this will be discussed in detail in chapters 18 and 19.

The pion spectrometer, consisting of the PACMAN dipole magnet equipped with field clamps and pairs of drift chambers and TOF counters for front and back, was placed as close to the target as the interaction between the two magnetic fields would allow. The two magnets exerted significant forces on each other and care had to be taken to maintain the alignment of the Helmholtz coils with respect to the target. Both magnetic fields pointed upwards, i.e. out of the scattering plane. The acceptance for the pion was measured to be 30 degrees in the horizontal (from -60 degrees up to -90 degrees relative to the beam axis) and ± 5 degrees in the vertical for this configuration. The total pathlength in the spectrometer from the entrance window of the first chamber to the exit window of the last chamber was

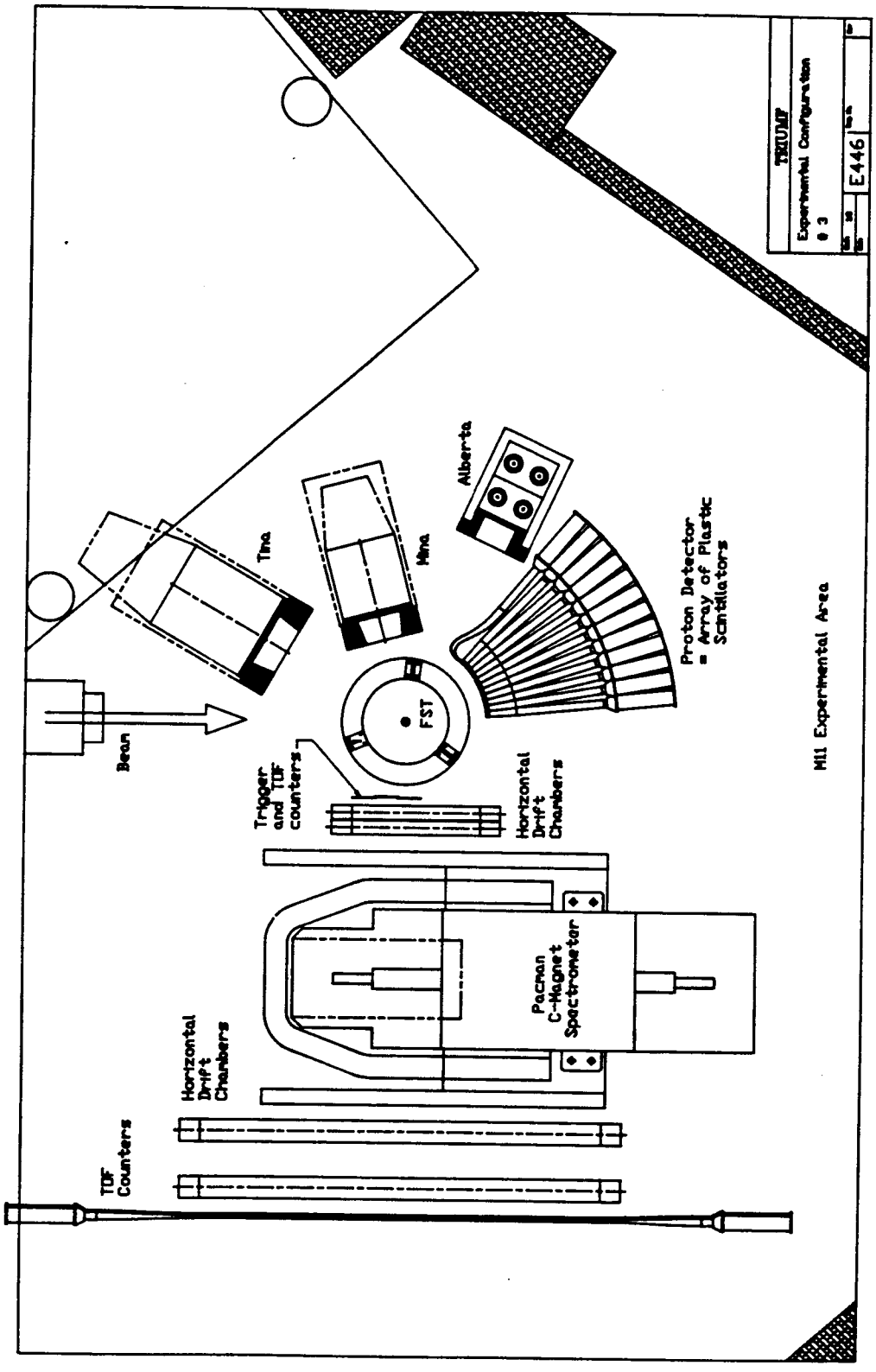

Figure 21. The detector layout for the TRIUMF bremsstrahlung experiment.

less than 200 cm which is of interest when we consider the problem of pion decay while the pion is still traversing the system.

The proton detector consisted of an array of plastic scintillator blocks, each spanning four degrees in the scattering plane and ±9 degrees in the vertical. This acceptance was carefully chosen to complement the acceptance of the pion spectrometer with respect to bremsstrahlung kinematics. The length of each block was sufficient to stop 130 MeV protons. The signal was seen by standard photomultiplier tubes mounted to the back of the detector. A single thin plastic scintillator (0.675 cm) covered the front of the whole setup to provide timing and $\frac{dE}{dx}$ information for particle identification.

Three NaI crystals (TINA, MINA, ALBERTA) served to detect the photon. The scintillation light from each crystal is recorded by photomultiplier tubes. Each detector is mounted on its own stand with suitable housing and support for electronics. All counters were equipped with lead collimators to define the angular acceptance ($\Delta\Omega_\gamma = 2\pi(1 - \cos 10°) = 0.095$ sr) and plastic scintillator paddles which served as vetos for charged particles. Notice that these veto counters cover only the one side of each detector which views the target. The other sides were not covered, which includes in particular the side which faces the beam. That side was shielded with several layers of lead blocks. Due to calibration problems, only two of the photon detectors (TINA at 150 degrees and MINA at 105 degrees) recorded useful data.

Aside from these three detector systems which measured direction and momenta of all three outgoing particles, we also had several sets of detectors to monitor the beam flux. The principles of their operation as well as some technical information will be discussed in conjunction with the beam line.

Chapter 10

The M11 Beam Line

The overall layout of the TRIUMF M11 beam line is shown in figure 22. The pions are produced by the 500 MeV primary proton beam hitting the production target T1 (12 mm beryllium). The quadrupole magnet Q9 and the dipole magnet B1 do most of the work to separate the pions from the proton beam and to select pions of the desired momentum. The accepted momentum bite can be selected by setting the slits according to the formula

$$\frac{\Delta p}{p} = \frac{\text{slit separation}}{18\text{ mm}}\%$$

where

$$p = f(\text{B1 magnetic field strength})$$

The final dipole magnet B2 serves to center the beam on target and to sweep out protons which have passed the momentum selection slits. To facilitate the latter function, it is necessary to put absorbers into the beam line to separate pion and proton momenta before they enter B2. Protons, which will lose slightly more energy in the absorber than pions, will be bent more. In the case of our experiment, this means that these protons will be bent towards the NaI detectors, in particular TINA. In order to avoid random background problems in TINA, a large amount of lead shielding had to be placed around the beam pipe. Despite the action of B1 and B2 and the absorber in the beam, there will still be protons to contaminate the beam. In our April run with a pion kinetic energy of 265 MeV at the target

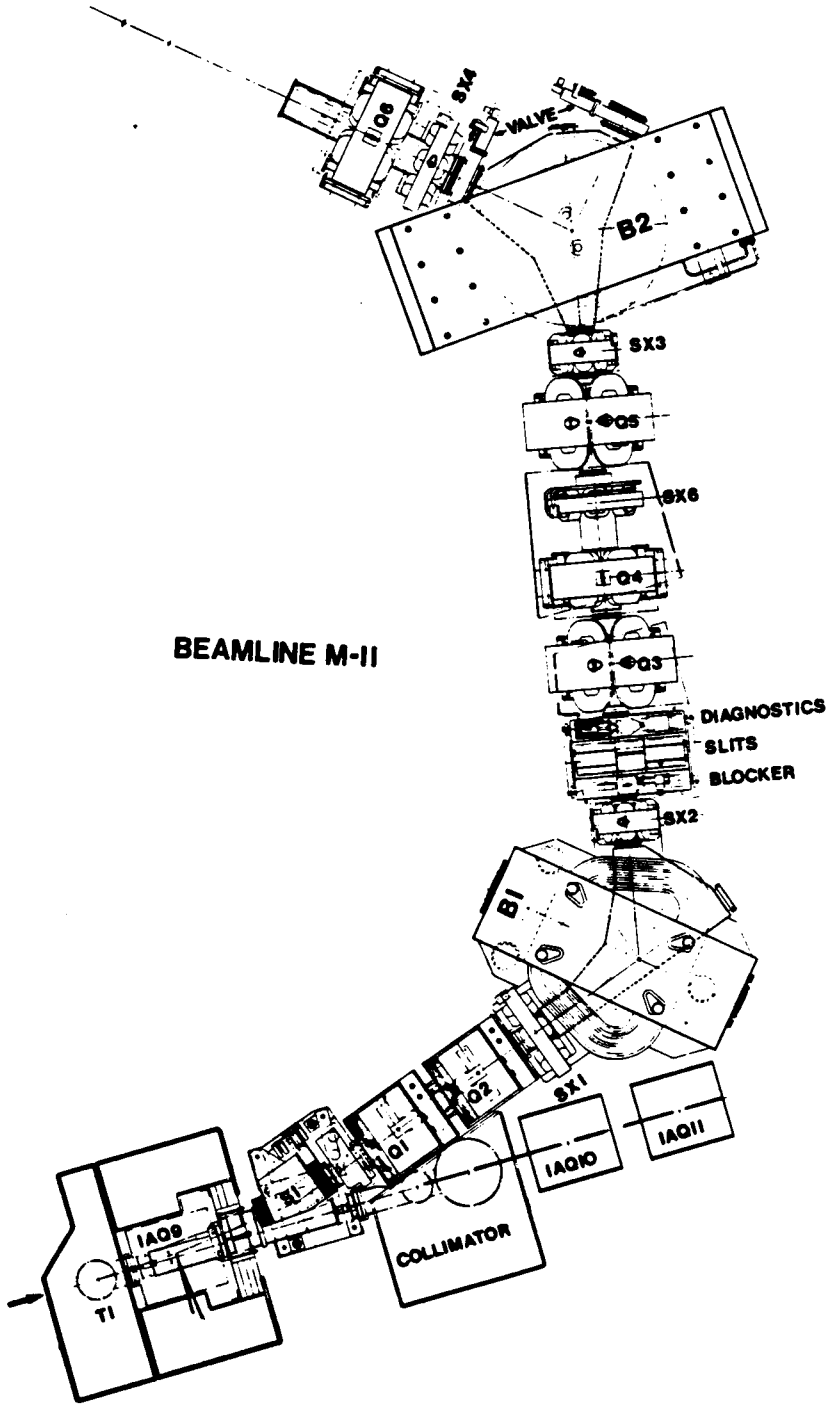

Figure 22. The TRIUMF M11 beam line.

location, a $\frac{\Delta p}{p}$ of 3 % and a 0.251 inch thick CH_2 absorber, 10 - 15 % of the beam on target were protons ($R = 15 \cdot 10^6 \frac{\pi^+}{s}$).

The whole beamline is 15.3 m long between T1 and the target location. Over this distance and at this energy about 50 % of the pions decay before they reach the target. This leads to a significant number of muons which accompany the pion beam down the beam line and form a halo that surrounds the beam. Again, a certain amount of shielding is necessary to stop these muons from causing harm to the experiment in the form of background.

A topic of particular interest to anyone designing the data acquisition part of the experiment is the time structure of the beam. The cyclotron delivers beam in pulses of 3 ns width every 43 ns. Since plastic scintillators with photomultiplier tube readout are capable of sub-ns time resolutions, the cyclotrons microstructure is a valuable tool to suppress background. In particular, in our case 43 ns is the time window in which a triple coincidence (pion, proton, photon) must occur for any bremsstrahlung event. Similarly, looking for a coincidence with any of the three particles out-of-time by 43 ns gives us a measure of the random background N (or $R_x = \frac{N}{S}$).

The maximum available M11 beam rate is given in figure 23 as a function of the pion kinetic energy for various T1 production targets.

10.1 Beam Rate Monitors

At beam rates of several MHz it is impossible to count the pions on target directly (which would have been done by placing a small scintillator barely exceeding the size of the target directly in front of the target so that it intersects the beam). Instead, several independent detector systems were used, which monitored the beam flux indirectly (see figure 24) :

- A split hodoscope, consisting of a total of four plastic scintillator paddles, intersected the beam about 200 cm downstream of the target. At this distance, the size of the beam spot has grown sufficiently large so that individual scin-

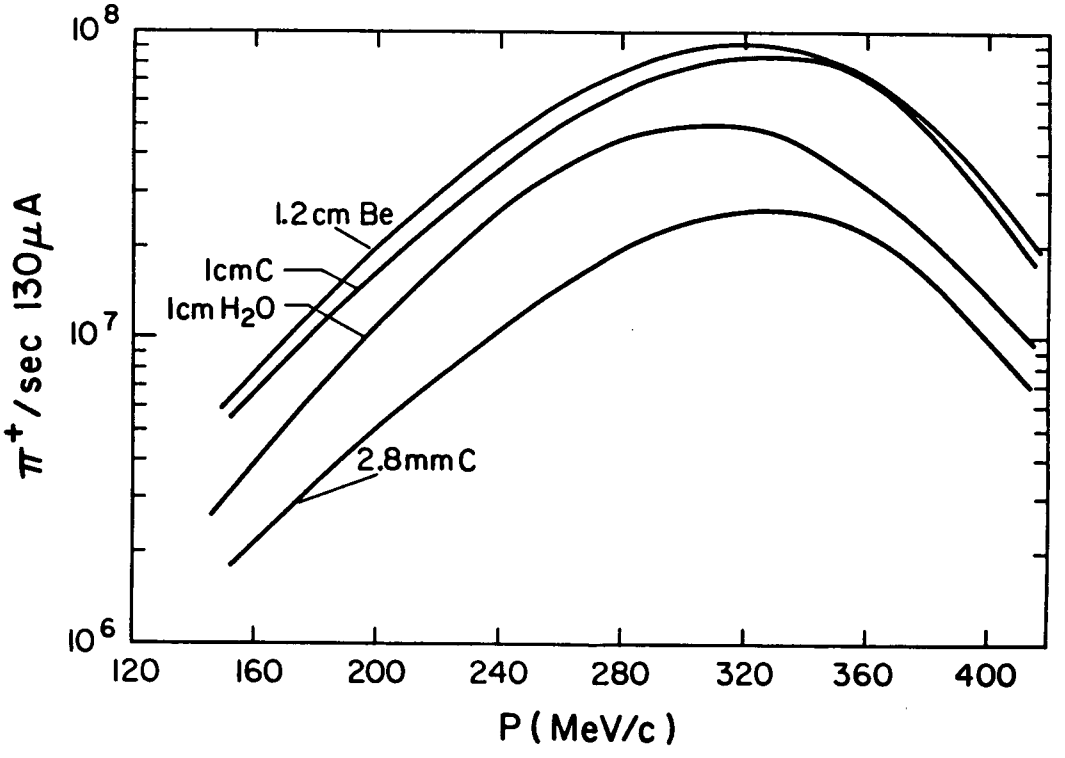

Figure 23. The maximum available M11 beam rate as function of the pion kinetic energy.

tillator paddles only see a rate of a few MHz, which is still large for this type of counter, but manageable. As a byproduct of this arrangement, one is also able to monitor the movement of the beamspot by comparing the count rate of several paddles. A movement of the beamspot can result from cyclotron operations (of order mm at the target location) or from changes in the B1/2 magnet settings (caused by human error).

- A partially active scintillator was placed about 60 cm downstream of the target. The problem of rate is handled by making the detector sensitive only over part of the total area. In this case, small holes of 1 mm diameter were drilled into a sheet of light guide material and then filled with plastic scintillator. The holes were spaced 5 mm apart in the horizontal and 15 mm apart in the vertical direction. The hole spacing is matched to the horizontal and vertical divergencies of the M11 beam, which are $\Delta\alpha = \pm 0.67°$ and $\Delta\beta = \pm 3.2°$, respectively. The ratio of the active scintillating area to the total area is 95:1. The reduction in the count rate, however, is less, about 80:1, due to the discrete sampling of the beam profile in the horizontal and vertical dimensions. This assumes, of course, that the beam spot is already big enough to cover several of these active spots. In order to avoid contributions to the count rate from random beam-uncorrelated events, in particular from activation of the light guide material, a second counter of this type is placed directly next to the first with sufficient optical shielding and put in coincidence so that only particles triggering both devices were counted. Furthermore, the electronics was set up in such a way that protons triggering the counters were rejected.

- A third set of detectors was placed around the beam pipe upstream of the target to sample the muon halo which results from pions decaying in flight. This method is, however, not very reliable due to the large amount of material which these muons have to traverse.

- In order to have at least one device which monitors the actual beam on target, we set up a telescope consisting of two small $(2.5\text{cm})^2$ - sized scintillators which

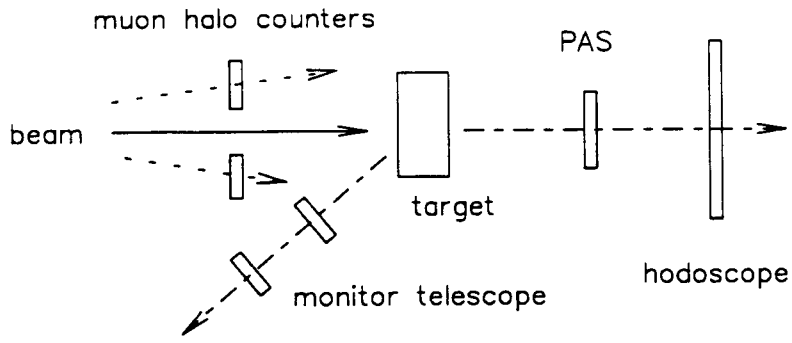

Figure 24. Schematic diagram showing the position of the beam monitors relative to the beam and the target.

were set up in coincidence to look at the target from directly below the beam line. This device looked at pions which were scattered from protons or carbon nuclei "in" the plane of polarization. The latter point is important because it guarantees that the count rate will be independent of the polarization of the target. The only drawback to this method was a low count rate of about 10 counts per minute.

The plots in figure 25 compare the performances of the beam monitoring systems to each other. A deviation from linearity indicates a time-dependence in the performance of the monitor system due to a variation in the gains or a change in the positioning of the detectors. It is our judgement that the partially active scintillator (PAS) produced the most consistent and accurate measurement and we will use it to normalize the data.

So far nothing has been said about how these detectors were calibrated, i.e. what was the actual beam rate on target ? This calibration is achieved by placing another detector directly in the beam after the beam rate has been lowered by cyclotron operators to acceptable levels for direct counting (of order 1 MHz). This procedure led to the following calibration for the PAS :

$$R_{Beam} = (79.3 \pm 2\%) \cdot R_{PAS}$$

Most of our bremsstrahlung data were taken with a pion beam rate of 15 MHz.

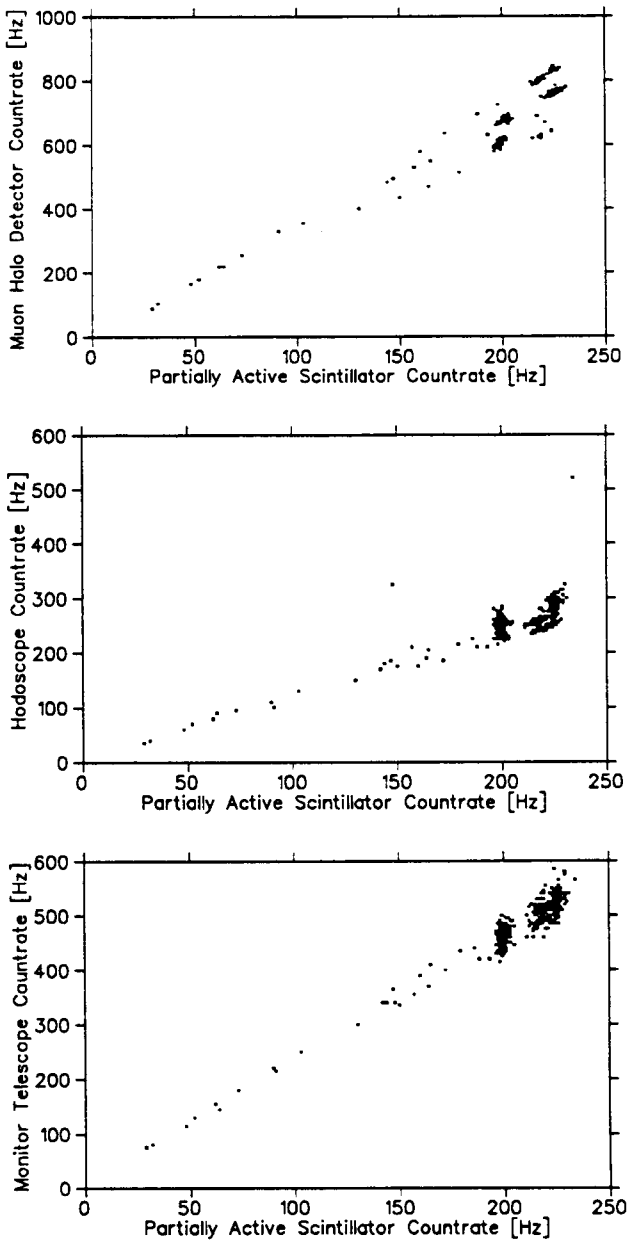

Figure 25. The performances of the beam monitors relative to each other.

Chapter 11

The TRIUMF Frozen Spin Target (FST)

The target consists of about 60 cm^3 of frozen butanol beads ($C_4H_{10}O$), 1-2 mm in diameter, cooled to 50 mK in liquid ^3He [47]. The packing fraction was measured to be 63 % which corresponds to an average butanol density of 0.59 $\frac{g}{cm^3}$. The beads are kept in a cylindrical copper cavity with 0.05 mm walls and a diameter of 40 mm. The target basket is surrounded by copper heat shields and aluminum and steel walls with diameters ranging from 44 mm to 92 mm. This adds up to 0.2 mm copper, 0.13 mm mylar, 0.13 mm steel and 1 mm aluminum. All in all the target material adds up to (by mass) 8 % free hydrogen, 4 % helium, 40 % carbon, 13 % oxygen, 17 % aluminum and 18 % copper and iron. As such, it is a very "dirty" target in that a lot of reactions can occur besides bremsstrahlung.

For the TRIUMF experiment, the hydrogen nuclei of the butanol were polarized in a $3.5 \cdot 10^3$ gauss magnetic field. Spin polarizations of typically 75 % were achieved by applying appropriate microwave frequencies of 70.580 and 70.200 GHz, respectively. The polarization was measured every 24 hours by nuclear magnetic resonance (NMR) methods just before the polarization was brought back up to its maximum value or changed sign. At the temperature of 50 mK and the given value for the magnetic field, polarization life times of typically 250 hours could be achieved. Over a 24 hour period the polarization dropped on average from 80 % to 72 %. The NMR signal was calibrated against the proton polarization signal at thermal equilibrium. The temperature measurement limited the relative accuracy of the polarization measurement to $\pm$ 2 % (= 0.04 FWHM).

With the full beam rate of order $10^7 \frac{\pi^+}{s}$ on target, the target temperature increased by a noticeable amount. Given that the polarization life time is inversely proportional to temperature to the 6th power, the operation of the target effectively limited the pion beam rate to the 15 MHz with which we took data.

Chapter 12

The Background

The search for possible background sources is based on information about the beam line, target station and detectors involved in the experiment, i.e. the task we are about to undertake presupposes a certain experiment design. A change of detectors, say, lead glass instead of NaI crystals, may remove some sources of background while introducing others which may be more damaging to the experiment. With this in mind we will now focus on the types of background which had to be considered for the bremsstrahlung experiment.

12.1 Random Coincidences

As the name implies, this background, which we denote by "N", is the result of two independent reactions which, by chance, occur at the same time and mirror the experimental signature of a true signal event. The rate of these coincidences is proportional to the product of the reaction rates, R_1 and R_2, times the timing resolution $\Delta\tau$. Two events will have to be separated from each other in time by at least $\Delta\tau$ before they can be identified as distinct events experimentally.

$$R_{accidental} = R_1 \cdot R_2 \cdot \Delta\tau \tag{12.1}$$

Accidental coincidences of more than two events are typically unimportant since $R_{accidental}$ will be proportional to some power of $\Delta\tau$ ($R^n \propto \Delta\tau^{n-1}$ for a n-fold

coincidence). The rate of accidental events must of course be compared to the signal rate, and, for very rare processes, n-fold accidentals may become important.

For this experiment, we can identify the following sources of random background :

- Elastic or inelastic π^+p scattering in coincidence with a random "photon".

  A "photon" here is an event which left some energy in the NaI detectors but "not" in the plastic scintillator paddles which serve as charged particle veto. Sources of "photons" are

  - Neutral or charged particles which enter the detector from the side of the beam. These may be muons from the decay of beam pions or secondary particles which originate from stopping protons in the lead shielding after they have been deflected from the pion beam by the magnet B2 (see M11 beam line).
  - π^+ induced π^0 production which is dominated by $\pi^+n \rightarrow \pi^0p$ on a bound neutron.
  - Charge-exchange reactions on nuclei leading to the detection of a neutron in the NaI detector.
  - Electrons from pions or muons which enter the NaI crystal and stop there, followed by the decays $\pi \rightarrow \mu\nu$, $\mu \rightarrow e\nu\bar{\nu}$. Only electrons leave a significant amount of energy in the detector.
  - π^+ - induced nuclear excitations where the excited nucleus decays back to the ground state by emission of a photon or neutron.

  The energy spectrum for πp"γ" coincidences can be determined experimentally by selecting π^+p events which are consistent with elastic scattering. The results are shown in figure 26. The random "photon" energy spectrum can be fitted to an empirical function of the form

$$\frac{dR}{dE_\gamma\, d\Omega_\gamma} = \alpha e^{-\beta k}[(\text{s MeV sr})^{-1}] \tag{12.2}$$

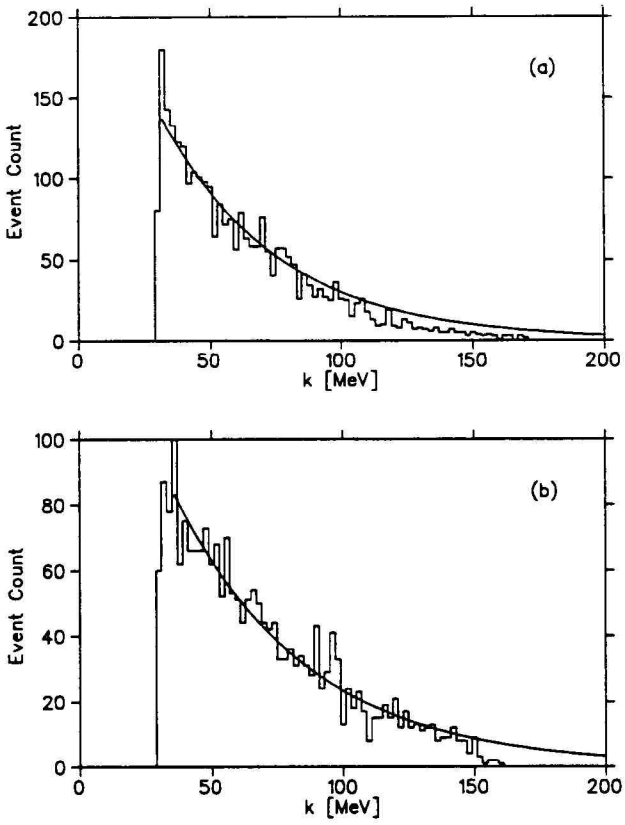

Figure 26. The energy spectrum for random photons. (a) for TINA, (b) for MINA. The solid line represents the exponential fit to the energy dependence.

Detector	α [(s MeV sr)$^{-1}$]	β [MeV^{-1}]
TINA	2800	$2.23 \cdot 10^{-2}$
MINA	1620	$1.98 \cdot 10^{-2}$

Table 4. α and β, which parameterize the random photon spectrum, for the two detectors TINA and MINA.

where α and β are listed in table 4.

The elastic π^+p scattering + random "photon" contribution can easily be eliminated as a background by reconstruction of kinematics. However, quasi-free scattering on a bound proton which is knocked out of the nucleus as a result, or elastic π^+p scattering with a loss of visible energy during the detection of either pion or proton, is a serious source of background, since the random "photon" can make up for the missing energy. In the case of quasi-free scattering, the missing energy is equal to the binding energy of the proton plus the energy that was left with the remaining nucleus in the form of nuclear excitation. An elastically scattered pion may look like a pion of less energy due to large angle coulomb scattering on material in the spectrometer or by decaying before it leaves the spectrometer. A proton can lose visible energy by undergoing a nuclear reaction before it is stopped in the plastic scintillator - a phenomenon known as "reaction tail", since it adds a low energy tail to the detector resolution function. In all cases the π^+p"γ" event may end up looking like a bremsstrahlung event.

- A nuclear reaction leading to a $\pi\gamma$ or $p\gamma$ signature in coincidence with a third particle (p or π, respectively).

$$\pi^+N \rightarrow \gamma pN' + \text{random } \pi$$

$$\pi^+N \rightarrow \pi^+N^* \rightarrow \pi^+\gamma N + \text{random } p$$

Due to the large angles at which we placed the NaI-detectors TINA and MINA, this is an unlikely source of background. We can get experimental evidence to support this conjecture by looking at the time and energy spectrum of "random protons", given a coincidence between a pion and a photon. One can see in figure 27 that the protons are all in time with the $\pi\gamma$ coincidence, leaving a negligible number of counts in the off-time window.

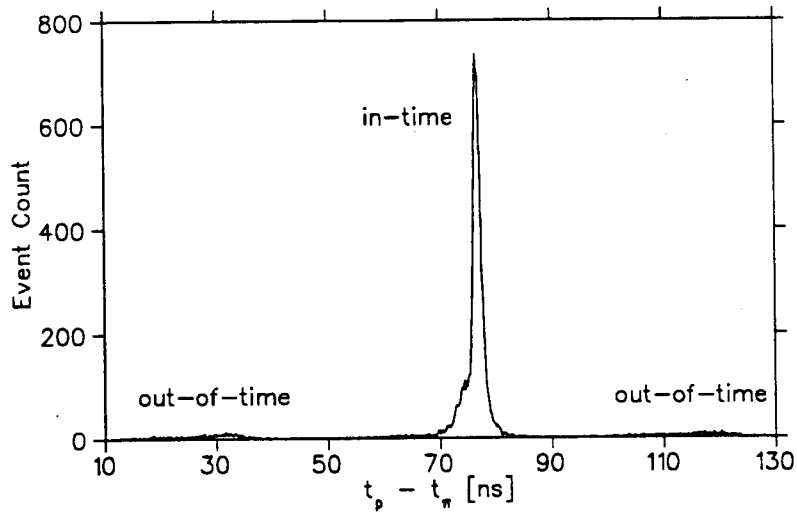

Figure 27. Time distribution of protons in random coincidence with a $\pi\gamma$ event.

12.2 Prompt Background

The prompt background "Q" consists of ($n \geq 3$)-body reactions which have a kinematic signature similar to bremsstrahlung :

- π^0 production

$$\pi^+ p \rightarrow \pi^+ p \pi^0, \;\; \pi^0 \rightarrow \gamma\gamma$$

The mass of the third neutral particle in $\pi^+ p \rightarrow \pi^+ p$ *Neutral* can be reconstructed with information on the π and p kinematics. This background can then easily be removed owing to the large mass of the π^0. As a matter of fact, for the pion and photon angles accessible in this experiment, no protons make it into our detector and this background does not exist.

- Quasi-free proton knockout followed by nuclear γ - decay.

$$\pi^+ N \rightarrow \pi^+ p N'^*, \;\; N'^* \rightarrow N'\gamma$$

The photon is distributed uniformly over 4π which leads to a suppression of $\frac{\Delta\Omega_\gamma}{4\pi} \approx 10^{-2}$ for this process. Furthermore, the branching ratio for nuclear γ - decay versus particle emission becomes exceedingly small for large excitation energies.

Target Material	*Proton Binding Energy*
Carbon	16.0 MeV
Oxygen	12.1 MeV
Iron	9.0 MeV
Aluminum	8.3 MeV
Copper	7.2 MeV

Table 5. Proton binding energy for various nuclei which are present in the target.

- Quasi-free bremsstrahlung

$$\pi^+ N \rightarrow \pi^+ p \gamma N'^*$$

The kinematics for this process will be smeared out relative to bremsstrahlung through the momentum distribution of the proton inside the nucleus. The most direct signature for this process is a missing energy

$$E_{miss} = T_0 - T_\pi - T_p - k$$

equal to the proton binding energy, whereas $E_{miss} = 0$ for bremsstrahlung.

Having identified the various sources of background we should now quantify their contributions to η and R_x of equation 8.9 on page 43. This can of course not be done without discussing in some detail our strategy for analyzing the data. In particular, we will have to introduce finite resolutions for all the kinematic variables which we aim to measure.

Chapter 13

The Analysis Strategy

The bremsstrahlung reaction

$$\pi^+ + p \longrightarrow \pi^+ + p + \gamma$$

is described by nine variables - momentum (p) and directon (α, β in spherical coordinates with the z-axis pointing out of the scattering plane) for the three final state particles, respectively - given the momentum and direction of the initial pion beam. Five of those variables are free parameters, whereas the other four are determined by energy and 3-momentum conservation. The five free parameters are traditionally chosen to be E_γ, α_γ, β_γ, α_π and β_π. Our proposal is to measure the full set of kinematic variables

$$E_\gamma, \alpha_\gamma, \beta_\gamma, q_\pi, \alpha_\pi, \beta_\pi, T_p, \alpha_p, \beta_p$$

where

$$\begin{aligned} E_\gamma &= \text{the photon energy} \\ q_\pi &= \text{the scattered pion momentum} \\ T_p &= \text{the scattered proton kinetic energy} \end{aligned}$$

and to use the constraints on the four dependent variables - q_π, T_p, α_p, β_p - to reduce the background. This program will be carried out in he following stages :

1. Particle Identification

   First, of course, we have to know that we are dealing with a pion, a proton and a photon.

- The Pion

  The spectrometer measures the momentum of the pion by following its track through a magnetic field. We have the following relations :

  $$\text{momentum} \propto (\text{bend angle})^{-1} \propto \text{mass/time-of-flight(TOF)}$$

  We can get an indication of the mass of the particle by plotting the TOF through the spectrometer against the bend angle which can be determined from chamber data (appendix C). This has been done for typical data on the frozen spin target and the results are shown in figure 28a. Figure 28b shows the same data plotted as a function of the angle in the (TOF,α_{bend})-plane. The particles which are analysed by the spectrometer can be clearly identified as pions or protons.

- The Proton

  The proton detector provides not only a measurement of energy by stopping the proton in blocks of plastic scintillator, but also a measurement of the differential energy loss $\frac{dE}{dx}$ through the thin scintillator covering the front of the whole assembly. We can use the knowledge of one - the energy - to predict the other - $\frac{dE}{dx}$ - under the assumption that the particle entering the detector is a proton. If the hypothesis is correct, the prediction will agree with the measurement. Figure 29 shows the ratio $\frac{dE}{dx}\Big)_{measured} / \frac{dE}{dx}\Big)_{predicted}$ for a typical data sample for the hypotheses of dealing with a proton (29a) and a pion (29b).

  Notice that the figures show a long tail towards small numbers. This is a representation of the reaction tail and comes from protons which interacted with nuclei in the scintillator before they were fully stopped. These reactions are inelastic and lead to a loss of visible energy, i.e. the energy which is measured is less than the energy of the incident proton. The cross section for nuclear reactions goes up with proton energy and thus this phenomenon becomes more important in the higher energy regime (for us this means $E_p > 100$ MeV).

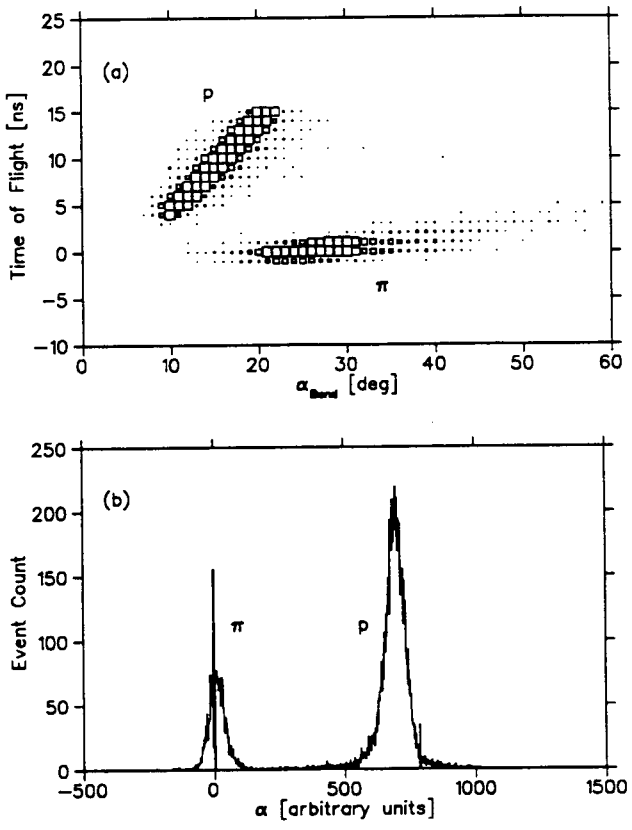

Figure 28. Particle identification with the pion spectrometer based on the relation between the time-of-flight (TOF) and the bend angle for a given track. Figure (a) shows the TOF plotted against the bend angle, figure (b) shows the projection of figure (a) onto the origin, i.e. the angle in the (TOF,α_{bend}) - plane.

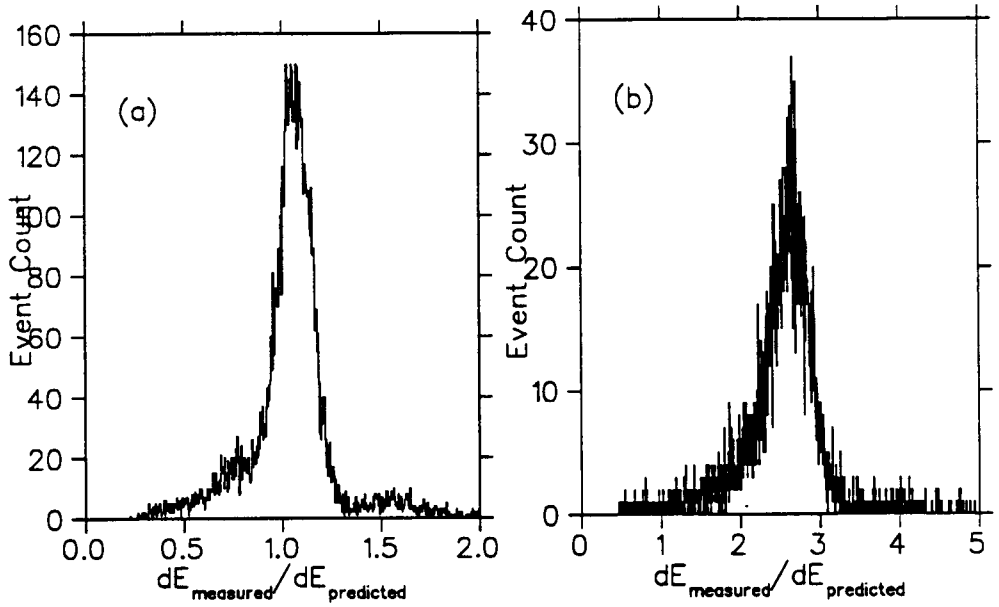

Figure 29. Particle identification with the proton detector based on energy and differential energy loss information. We plot $dE_{measured}/dE_{predicted}$ for the hypothesis of looking at (a) a proton and (b) a pion. The correct hypothesis will result in a peak at a ratio of 1.

- The Photon

  The distinction between neutral and charged particles entering the NaI detectors from the direction of the target can be made based on the information in the veto counters. A hit clearly identifies a charged particle. Figure 30 shows the distribution of $(t_{Veto} - t_{NaI})$ for a typical data sample and indicates the time window which has been set in our data analysis for the identification of charged particles. Events which fall outside of this window are interpreted as accidental hits, uncorrelated to the NaI signal. The identification of the neutral particle as a photon or neutron has to be achieved through methods which utilize information outside of the photon detector in conjunction with hypotheses about the original process (e.g. missing energy in conjunction with a bremsstrahlung hypothesis).

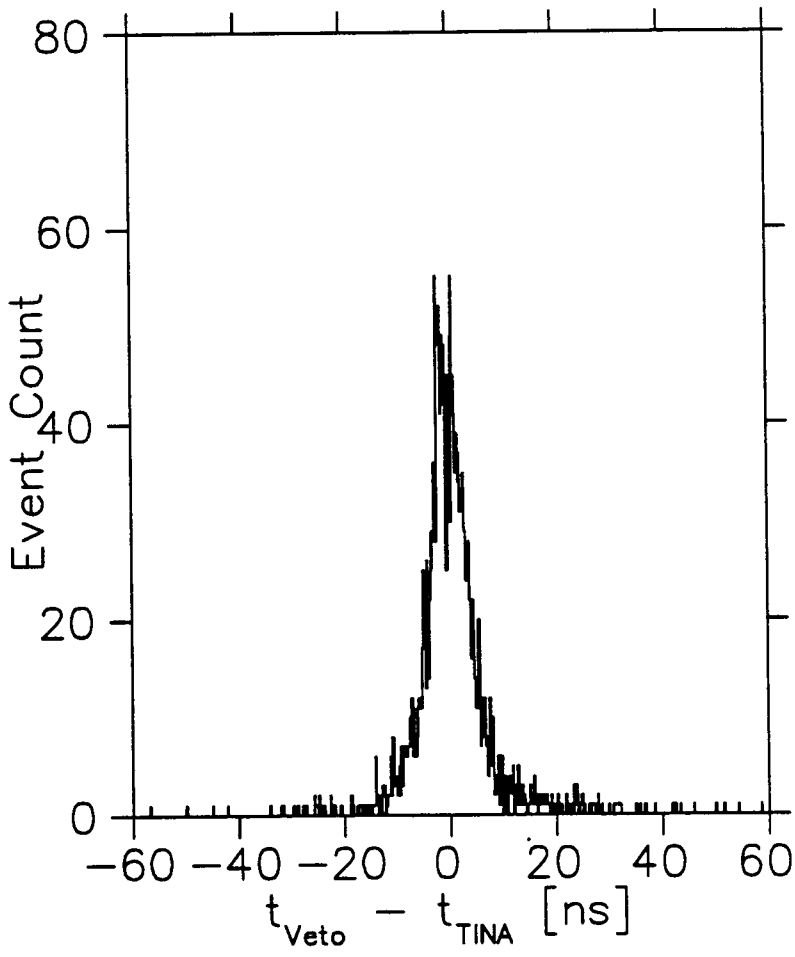

Figure 30. Neutral/charged particle identification with the photon detectors based on timing information from the charged particle veto counters.

2. Elastic Scattering

   There are only two free kinematic variables for elastic π^+p scattering - the pion angles relative to the beam, α_π and β_π. All other variables - q_π, T_p, α_p, β_p - are constrained by energy and momentum conservation and any combination of them can be used to identify elastic π^+p scattering. Some typical event distributions are shown in figure 31.

3. Bremsstrahlung

   After we have convinced ourselves that the event signatures for a 3-particle coincidence are those of a pion, a proton and a photon, and the measured kinematic variables have survived our rejection criteria for elastic π^+p scattering, we have to face the possibility that this might be a bremsstrahlung event. The next step is determined by how much background $(Q + N)$ there is. If it is small and the signal is clearly identified, we can apply our background subtraction procedures and begin calculating cross-sections and/or asymmetries. Otherwise, some form of background suppression is needed, the most powerful of which is a χ^2-analysis on all of the measured variables. The principles of this kind of analysis are introduced in the next section and developed into a tool in appendix B.

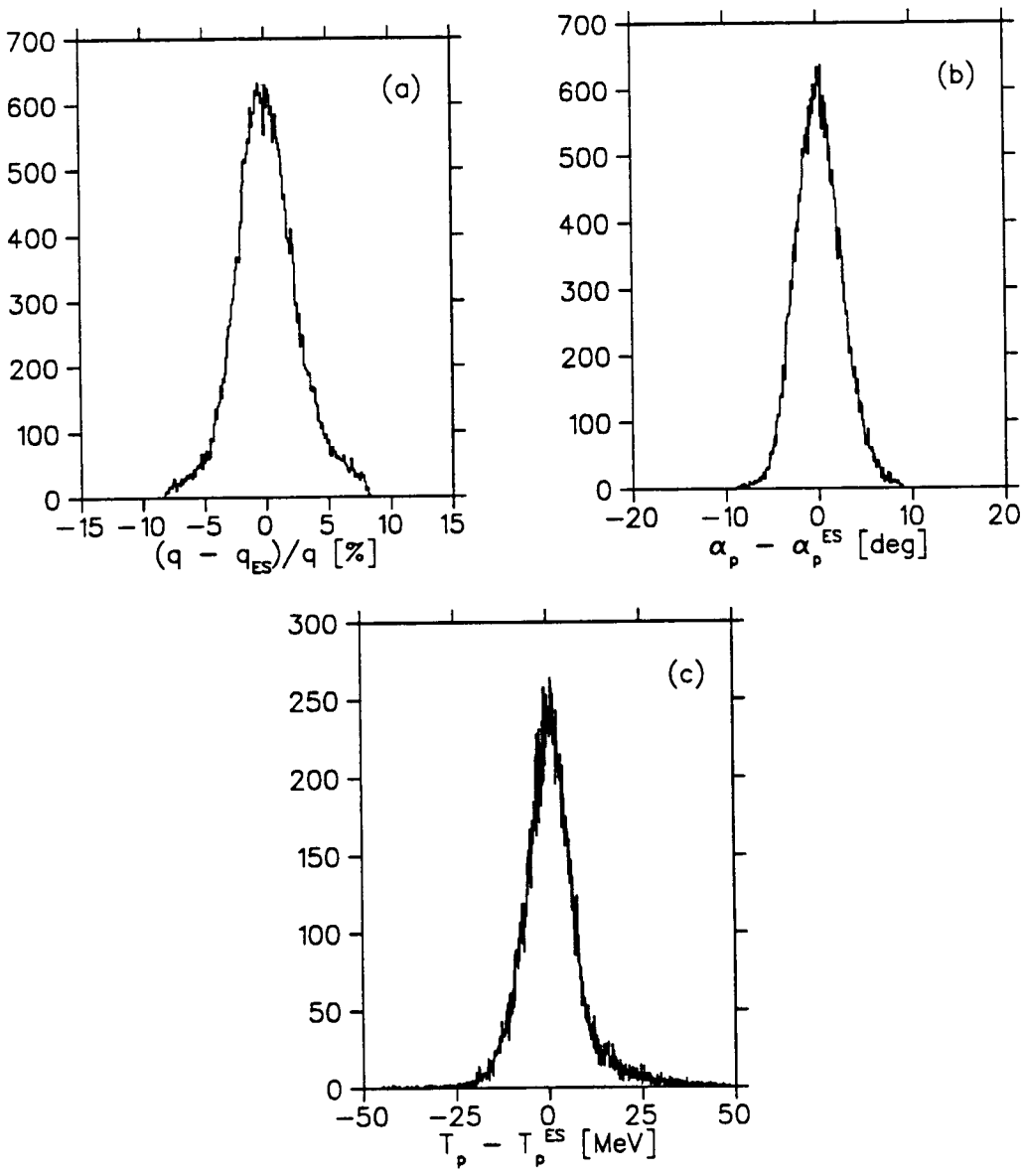

Figure 31. Typical event distributions for elastic $\pi^+ p$ scattering data on the frozen spin target. (a) $\frac{\delta q}{q}$, (b) $\alpha_p - \alpha_p^{ES}$, (c) $T_p - T_p^{ES}$.

Chapter 14

The Analysis Model

The goal of this discussion is to show the connection between detector parameters, in particular the measurement resolution, and the results which can be expected from a full analysis of the data with respect to a certain hypothesis (e.g. bremsstrahlung kinematics).

Let us describe a "measurement $\mathbf{m}$" as a vector of N variables m_i, $i = 1 \ldots N$, where m_i are momenta, angles and such. This measurement is the result of an event which has occured in the detector. We might have predicted that the momenta and angles we should have measured are given by the set of numbers e_i, $i = 1 \ldots N$. For a large number of these events the measurements $\mathbf{m}$ will be randomly distributed around the actual events $\mathbf{e}$ with a distribution function $P(\mathbf{m}|\mathbf{e})$. This function can also be interpreted as the conditional probability of making a measurement $\mathbf{m}$ given that the "event $\mathbf{e}$" has occured. We will call $P(\mathbf{m}|\mathbf{e})$ the "detector resolution function" because it will be a function of the "mean standard deviations σ_i, $i = 1 \ldots N$" which characterize each measurement m_i and must be considered as design parameters for the detector.

Since we can calculate the number of events $\rho(\mathbf{e})$ which should occur during a time interval Δt and for a given beam rate and target thickness, we can determine the number of measurements $\mathbf{m}$, $\rho(\mathbf{m})$:

$$\rho(\mathbf{m}) = \int P(\mathbf{m}|\mathbf{e})\rho(\mathbf{e})\, d\mathbf{e}$$

Out of $\rho(\mathbf{m})$ events, only a fraction $P(\mathbf{m}|\mathrm{T})$ will be accepted by the data acquisition system and stored for further analysis. We will assume here that $P(\mathbf{m}|\mathrm{T})$ is equal to 1 for every measurement $\mathbf{m}$ which was caused by an event of interest $\mathbf{e}$. Before we go on, we should distinguish between signal and background :

$$\rho_S(\mathbf{m}) = \int P(\mathbf{m}|\mathbf{e})\rho_S(\mathbf{e})\, d\mathbf{e}$$

$$\rho_B(\mathbf{m}) = \int P(\mathbf{m}|\mathbf{e})\rho_B(\mathbf{e})\, d\mathbf{e}$$

The goal of the data analysis is to reduce ρ_B over ρ_S by making a judgement on how similar the measurement $\mathbf{m}$ is to the hypothesis $\mathbf{e}_S$ = a signal event. If the measure of similarity exceeds a certain bound, the measurement $\mathbf{m}$ is rejected. Mathematically, we have to

- associate the measurement $\mathbf{m}$ with the hypothesis $\mathbf{e}_S$: $\mathbf{m} \rightarrow \mathbf{e}_S$. In a χ^2-analysis, this is accomplished by performing a least-squares fit which associates the measurement $\mathbf{m}$ to that particular hypothesis $\mathbf{e}_S$ which has most likely caused $\mathbf{m}$.
- define a measure of similarity $\lambda = \lambda(\mathbf{e}_S|\mathbf{m})$. In a χ^2-analysis, this is simply $\chi^2(\mathbf{e}_S|\mathbf{m})$.
- reject any measurement for which $\lambda(\mathbf{e}_S|\mathbf{m}) > \lambda_0$.

It is straightforward to define the number of events which survive the full analysis :

$$S = \rho_S(\mathbf{e}_S) = \int_{\mathbf{m}\rightarrow\mathbf{e}_S} d\mathbf{m}\, \Theta(\lambda(\mathbf{e}_S|\mathbf{m})) \int d\mathbf{e}\, P(\mathbf{m}|\mathbf{e})\rho_S(\mathbf{e})$$

$$B = \rho_B(\mathbf{e}_S) = \int_{\mathbf{m}\rightarrow\mathbf{e}_S} d\mathbf{m}\, \Theta(\lambda(\mathbf{e}_S|\mathbf{m})) \int d\mathbf{e}\, P(\mathbf{m}|\mathbf{e})\rho_B(\mathbf{e})$$

which simply amounts to summing up all measurements $\mathbf{m}$ which have been associated with $\mathbf{e}_S$ and which have passed the similarity cut

$$\Theta(\lambda(\mathbf{e}_S|\mathbf{m})) = \begin{cases} 0 & \text{for } \lambda > \lambda_0 \\ 1 & \text{for } \lambda \leq \lambda_0 \end{cases}$$

These awkward looking expressions are developed further in appendix B and it is shown there, furthermore, that the similarity measure λ is directly related to the detector resolutions σ_i, $i = 1 \ldots N$.

With this, S and B above reduce to functions of detector design parameters (i.e. the σ_i). We are now able to calculate η ($= \frac{B}{S}$ for $B = Q$) and R_x ($= \frac{B}{S}$ for $B = N$).

Chapter 15

Quantitative Results for Prompt and Accidental Background

The development of the analysis strategy in chapter 13 is based on a knowledge of the bremsstrahlung kinematics and an understanding of the dominant sources of background. If we follow this strategy, we can be sure to find bremsstrahlung events in the data sample. However, we can not yet guarantee success for the experiment.

We have to know, whether the signal can be separated from the background, which kinematic variables are most instrumental in suppressing the background, and how much effort has to be put into the design of the detectors, which measure those variables. A general methodology to study these issues is based on the results derived in appendix B and we apply it in this chapter to the bremsstrahlung experiment. The end result will be an analysis strategy which is fault-tolerant, since it is based on an understanding of how the data analysis is affected by finite measurement resolutions and possible detector failures.

The questions we would like to answer are the following :

- How does the inclusion of a finite detector resolution parameterized by the vector $\vec{\sigma} = \{ \sigma_i, i = 1 \ldots N \}$ affect the relation between measured and calculated cross sections and asymmetries ? Do we retain the ability to distinguish between different theoretical models ?

- How important are the prompt (η) and accidental (R_x) backgrounds ? How much beam time do we need in order to satisfy the bound on $\delta\mathcal{A}$, the error of the asymmetry measurement (equation 8.9), given the results for η and R_x ?

- How do we have to change the design parameters of our experiment in order to reduce η and R_x ?
- Can we save development costs by changing design parameters in a manner which leaves η and R_x constant ?
- How fault-tolerant is our detector design ? Can we afford to lose resolution in any of the detector arms ? What happens if a detector component fails entirely ?

We will answer these questions for the following special case :

- The bremsstrahlung cross section $\frac{d^5\sigma}{dE_\gamma d\Omega_\gamma d\Omega_\pi}$ is calculated from equation 2.5, which is the classical result (i.e. the first term in a Low expansion of the cross section) because it has proved to be a very good description of experimental data. The asymmetries are taken from programs which have been developed by the groups from MIT and TRIUMF.
- We have two sources of background : quasi-free bremsstrahlung (QFBS) as an example of a prompt background and quasi-free scattering (QFS) in coincidence with a random "photon" (see section 12.1 on accidental background) as an example of a background which contributes to R_x. The QFBS and QFS cross sections are taken from a calculation based on the impulse approximation. The results are normalized to experimental data [48].
- The nominal set of kinematic variables which are measured is

$$\{q_0, q_\pi, \alpha_\pi, \beta_\pi, T_p, \alpha_p, \beta_p, E_\gamma, \alpha_\gamma, \beta_\gamma\}$$

We furthermore assume that α_π and β_π are measured precisely, i.e. $\sigma_{\alpha_\pi} = \sigma_{\beta_\pi} = 0$ (this is justified in chapter 17, where we study the performance of the pion spectrometer).

- The mean standard deviations σ_i are taken from experiment and will serve as a concrete example.

$$\sigma = \frac{1}{2.355}\{0.03\,q_0, 0.045\,q_\pi, 0, 0, 10\,\mathrm{MeV}, 6°, 18°, 10\,\mathrm{MeV}, 20°, 20°\}$$

The factor of 2.355 in this expression relates the standard deviation σ to the measured full-width-half-maximum value, FWHM = 2.355 σ.

15.1 Cross Sections and Asymmetries Averaged over Acceptance and Detector Resolution

The quantities $\overline{\frac{d\sigma}{dV}}$ and $\overline{\mathcal{A}}$ which will be measured by the experiment can be expressed in terms of the calculated cross section $\frac{d\sigma}{dV}$ and asymmetry $\mathcal{A}$ as follows :

$$\overline{\frac{d\sigma}{dV}} = \frac{\int_{\Delta V} dV' \int dV \, \mathcal{D}_0(p'|p) \frac{d\sigma}{dV}}{\int_{\Delta V} dV' \int dV \, \mathcal{D}_0(p'|p)} \tag{15.1}$$

$$\overline{\mathcal{A}} = \frac{\int_{\Delta V} dV' \int dV \, \mathcal{D}_0(p'|p) \frac{d\sigma}{dV} \mathcal{A}}{\int_{\Delta V} dV' \int dV \, \mathcal{D}_0(p'|p) \frac{d\sigma}{dV}} \tag{15.2}$$

where

$dV^{(\prime)}$	is the unit volume in the parameter space on which the cross section is defined, e.g. $dV = dE_\gamma d\Omega_\gamma d\Omega_\pi$
ΔV	is the acceptance volume into which data will be binned
p, p'	are points in the 5-dimensional parameter space V
$\mathcal{D}_0(p'\|p)$	is a weight function (see appendix B) which contains information on the analysis strategy and detector resolution

We get back our earlier results from chapter 6, a simple averaging over the bin size ΔV, for an infinitely high detector resolution, $\sigma_i \rightarrow 0$, in which case $\mathcal{D}_0$ turns into a delta function $\delta(p' - p)$.

The ratio between averaged and calculated quantities $\overline{X(p_0)} \,/\, X(p_0)$ depends not only on the bin size and detector design but also on the particular model which was used to calculate X (i.e. predictions for cross sections and asymmetries).

We list results for the point calculations, averages over acceptance with infinite detector resolutions and averages over acceptance with finite detector resolutions in tables 6 (TINA) and 7 (MINA) for

$$\begin{aligned} \alpha_\pi &= -75^\circ & \beta_\pi &= 0^\circ \\ \alpha_\gamma &= 105^\circ \text{ (MINA)} & \beta_\gamma &= 0^\circ \\ \alpha_\gamma &= 150^\circ \text{ (TINA)} \end{aligned}$$

$$\begin{aligned} \Delta\mathbf{p} &= (\Delta\alpha_\pi = 10^\circ) \cdot (\Delta\beta_\pi = 10^\circ) \cdot \\ &\quad (\Delta\alpha_\gamma = 20^\circ) \cdot (\Delta\beta_\gamma = 20^\circ) \cdot \\ &\quad (\Delta k = 10 \text{ MeV}) \end{aligned} \tag{15.3}$$

and

$$\mathcal{D}_0(p'|p) = \mathcal{D}_0(x) = e^{-x}. \tag{15.4}$$

We have employed a Monte Carlo method to implement the averaging of cross sections and asymmetries over the acceptance and the detector resolution. This gives rise to statistical uncertainties of the order of 2 %.

k in MeV		35	45	55	65	75	85	95	105	115	125
Point	$d\sigma$	2.486	2.245	2.177	2.206	2.266	2.349	2.360	2.331	2.188	1.875
	A_{MIT}	0.184	0.008	-0.127	-0.176	-0.161	-0.125	-0.093	-0.069	-0.053	-0.045
	A_{TRIUMF}	0.439	0.421	0.400	0.362	0.298	0.217	0.143	0.089	0.057	0.041
	ΔA	-0.255	-0.413	-0.527	-0.538	-0.459	-0.342	-0.236	-0.158	-0.110	-0.086
$\Delta p(0)$	$d\sigma$	2.678	2.428	2.324	2.298	2.309	2.315	2.310	2.235	2.068	1.753
	A_{MIT}	0.183	0.011	-0.121	-0.173	-0.162	-0.128	-0.095	-0.070	-0.054	-0.046
	A_{TRIUMF}	0.431	0.413	0.392	0.353	0.288	0.208	0.137	0.086	0.055	0.038
	ΔA	-0.248	-0.402	-0.513	-0.526	-0.450	-0.336	-0.232	-0.156	-0.109	-0.084
$\Delta p(\sigma)$	$d\sigma$	2.568	2.363	2.187	2.291	2.269	2.339	2.291	2.233	2.084	1.874
	A_{MIT}	0.161	0.024	-0.124	-0.167	-0.165	-0.125	-0.095	-0.069	-0.054	-0.046
	A_{TRIUMF}	0.433	0.419	0.388	0.357	0.287	0.219	0.144	0.091	0.056	0.042
	ΔA	-0.272	-0.395	-0.512	-0.524	-0.452	-0.344	-0.235	-0.160	-0.110	-0.086

Table 6. The cross section and asymmetry averaged over the acceptance bin and detector resolution for TINA.

k in MeV		35	45	55	65	75	85	95	105	115	125
Point	$d\sigma$	2.190	1.943	1.809	1.750	1.736	1.718	1.750	1.723	1.698	1.659
	A_{MIT}	0.268	0.033	-0.305	-0.663	-0.858	-0.814	-0.647	-0.474	-0.339	-0.241
	A_{TRIUMF}	0.434	0.372	0.271	0.114	-0.119	-0.422	-0.719	-0.863	-0.800	-0.627
	ΔA	-0.166	-0.339	-0.576	-0.777	-0.739	-0.392	0.072	0.389	0.461	0.386
$\Delta p(0)$	$d\sigma$	2.436	2.148	1.993	1.913	1.849	1.803	1.775	1.729	1.690	1.633
	A_{MIT}	0.266	0.041	-0.278	-0.611	-0.811	-0.802	-0.662	-0.497	-0.359	-0.257
	A_{TRIUMF}	0.429	0.368	0.270	0.120	-0.100	-0.380	-0.648	-0.794	-0.769	-0.633
	ΔA	-0.163	-0.327	-0.548	-0.731	-0.711	-0.422	-0.014	0.297	0.410	0.376
$\Delta p(\sigma)$	$d\sigma$	2.450	2.078	1.979	1.933	1.789	1.780	1.718	1.721	1.709	1.646
	A_{MIT}	0.247	0.048	-0.269	-0.605	-0.808	-0.791	-0.659	-0.500	-0.352	-0.263
	A_{TRIUMF}	0.423	0.373	0.274	0.121	-0.101	-0.384	-0.652	-0.810	-0.771	-0.655
	ΔA	-0.176	-0.325	-0.543	-0.726	-0.707	-0.407	-0.007	0.310	0.419	0.392

Table 7. The cross section and asymmetry averaged over the acceptance bin and detector resolution for MINA.

15.2 Results for Prompt and Accidental Backgrounds and Estimates of the Required Beam Time

The tables 8 (TINA) and 9 (MINA) list the results for η (the prompt background, equation B.15) and R_x (the accidental background, equation B.16) for the bin size and central values which were defined in the last section (equation 15.3) and for

$$N = 8, \quad n = 4, \quad \beta = 0.5123, \quad \mathcal{D}(x) = e^{-\frac{1}{2}\beta x}. \tag{15.5}$$

The results can be summarized as follows

$$\begin{array}{lllll} \text{TINA}: & \eta & \leq & 0.4 \cdot 10^{-3} & \qquad \text{MINA}: \quad \eta \leq 1.5 \cdot 10^{-3} \\ & R_x & \leq & 1.0 & \qquad R_x \leq 0.5 \end{array}$$

which leads us to conclude that

- η is consistent with zero, i.e. there is no prompt background. Consequently, we do not have to worry about the complexities of an empty-target run. The results from the PSI experiment [44] are consistent with this conclusion.
- The accidental background is most important at low photon energies and becomes negligible at energies above 100 MeV. This is expected, since the random photon spectrum is described by an exponential function while the bremsstrahlung spectrum follows a $\frac{1}{k}$ behaviour.
- The accidental background is substantial and a representative value is given by $R_x = 1.0$.

The upper bound on $\delta\mathcal{A}$ for $\eta = 0$ reads (see appendix G)

$$(\delta\mathcal{A})^2_{desire} \overset{\eta=0}{\geq} \frac{1}{2P^2}\left\{\frac{1}{S_0}(1+4R_x) + \left(\frac{\delta M_0}{M_0}\right)^2 + \left(\frac{\delta\epsilon}{\epsilon}\right)^2\right\} + \left(\frac{\delta P}{P}\right)^2$$

with

$$S_0 = (R\,\Delta t)\cdot 0.02\,\frac{\text{events}}{\text{MHz h nb}}$$

for the acceptance bin

$$\Delta\mathbf{p} = (10\text{MeV})_\gamma (2\pi[1-\cos 10°])_\gamma (10° \cdot 20°)_\pi$$

k in MeV	35	45	55	65	75	85	95	105	115	125
$\eta \cdot 10^3$	0.16	0.20	0.10	0.21	0.39	0.07	0.02	0.02	0.01	0.02
R_x	0.92	0.76	0.69	0.25	0.35	0.15	0.08	0.06	0.01	0.00

Table 8. Results for prompt and accidental background for TINA.

k in MeV	35	45	55	65	75	85	95	105	115	125
$\eta \cdot 10^3$	1.54	0.20	0.45	0.16	0.22	0.12	0.10	0.27	0.06	0.01
R_x	0.49	0.39	0.49	0.21	0.19	0.24	0.16	0.10	0.06	0.01

Table 9. Results for prompt and accidental background for MINA.

and $\rho = 0.08 \frac{\mathrm{g}}{\mathrm{cm}^3}$, $\varepsilon = 0.5$, $m_A = 1$, $\int Ft\, dA = 0.755 \cdot 5\mathrm{cm}$, $\frac{d\sigma}{dp} = 1 \frac{\mathrm{nb}}{\mathrm{MeV\ sr}^2}$, $\left(\frac{\delta M_0}{M_0}\right) = 0.01$, $\left(\frac{\delta \varepsilon}{\varepsilon}\right) = 0.01$, $\left(\frac{\delta P}{P}\right) = 0.04$, and $(\delta \mathcal{A})_{desired} = 0.1$. With these data we find the following bound on $(R\,\Delta t)$:

$$\begin{aligned} (R\,\Delta t) &\geq 5400\,(1 + 4R_x)\ \mathrm{MHz\ h} \\ &\geq 27000\ \mathrm{MHz\ h} \end{aligned}$$

which must be compared to our proposal of

$$(R\,\Delta t) = 15\ \mathrm{MHz} \cdot 300\ \mathrm{h} = 4500\ \mathrm{MHz\ h}.$$

The large discrepancy between the two numbers forces us to accept a larger value for $\delta \mathcal{A}$,

$$\delta \mathcal{A}(4500\ \mathrm{MHz\ h}, R_x = 1.0) \approx 0.23,$$

whereas a value of $R_x \approx 0$ would allow us to keep $\delta \mathcal{A}$ at

$$\delta \mathcal{A}(4500\ \mathrm{MHz\ h}, R_x = 0.0) \approx 0.11.$$

These results indicate the importance of keeping R_x small.

Index i	1	2	3	4	5	6	7	8
$\mathbf{p}_i$	q_0	q	T_p	α_p	β_p	α_γ	β_γ	k
$D_{\sigma_i} R_x$ (MINA)	0.31	0.33	1.00	0.006	0.22	0.07	0.09	0.63

Table 10. The dependence of the accidental background-to-signal ratio on the detector resolution. The index i labels the set of kinematic variables **p** and the corresponding measurement resolutions $\sigma_{\mathbf{p}_i} = \sigma_i$.

15.3 Ways to Reduce the Accidental Background

We will study the dependence of R_x on the detector resolutions σ_i with the help of the derivatives of R_x with respect to the σ_i, $D_{\sigma_i} R_x$, as defined in equation B.19.

$$\begin{aligned} D_{\sigma_i} R_x &\equiv \frac{1}{R_x} \cdot \sigma_i \cdot \frac{\partial}{\partial \sigma_i} R_x \\ \frac{\Delta R_x}{R_x} &= \sum_i \left(\frac{\Delta \sigma_i}{\sigma_i} \right) D_{\sigma_i} R_x \end{aligned}$$

In order to keep the process simple, we will look at one detector, MINA, and one acceptance bin only, namely

$$\begin{aligned} \alpha_\pi &= -75^\circ & \Delta\alpha_\pi &= 10^\circ \\ k &= 75 \text{ MeV} & \Delta k &= 10 \text{ MeV} \\ \alpha_\gamma &= 105^\circ & \Delta\alpha_\gamma &= 20^\circ \, . \end{aligned}$$

The value of R_x for this bin is (see previous section)

$$R_x(\text{MINA}) = 0.19.$$

The results are listed in table 10. The gradients $D_{\sigma_i} R_x$ are generally small (of order 0.1), indicating that none of the measurements (at current detector resolutions) serve to substantially reduce R_x, i.e. bremsstrahlung and quasi-free scattering can not be distinguished effectively.

Our ability to suppress the quasi-free background is characterized by the missing energy $T_{miss}^{\pi p \gamma} = T_0 - T_\pi - T_p - k$. The resolution in this variable must be smaller than the proton binding energy inside the nucleus, before cuts on kinematic

a	R_x	$D_{\sigma_i}R_x$ $i=1$	2	3	4	5	6	7	8
		p_i q_0	q	T_p	α_p	β_p	α_γ	β_γ	k
1.0	0.19	0.31	0.33	1.00	0.006	0.22	0.07	0.09	0.63
0.9	0.14	0.29	0.44	1.12	0.008	0.27	0.10	0.15	0.60
0.8	0.088	0.44	0.39	1.11	0.011	0.12	0.11	0.35	0.72
0.7	0.053	0.46	0.41	1.18	0.014	0.40	0.24	0.65	0.86
0.6	0.025	0.35	0.31	1.03	0.019	0.46	0.21	1.33	1.09
0.5	0.009	0.47	0.14	0.57	0.021	0.31	0.23	2.49	1.83
0.4	0.002	0.06	2.33	0.86	0.047	0.47	0.13	3.28	1.85
0.3	$2.5 \cdot 10^{-5}$	1.73	-0.55	0.004	0.047	1.62	0.88	9.58	6.53

Table 11. The dependence of R_x and $D_{\sigma_i}R_x$ on the overall resolution of the detectors.

variables will become effective. This is not the case for the present detector resolution. In table 11 we study the behaviour of R_x and $D_{\sigma_i}R_x$ as the overall detector resolution is scaled down, i.e. $\vec{\sigma} = a\vec{\sigma}_0$, where $\vec{\sigma}_0$ is the standard set of detector resolutions.

We find that

- R_x drops rapidly to zero at values of the scale parameter $a \leq 0.5$. This indicates that the present missing energy resolution must be reduced by a factor of two before we can reject quasi-free scattering events.

- the importance of the photon energy and angle measurements grows ($D_{\sigma_i}R_x$ becomes large) as a becomes small, even though the photon is a random photon and its kinematics is *not* related to the pion or proton energies. This is an effect which is induced by the full χ^2-analysis which we have employed so far. Quasi-free scattering events are removed from the hypersurface of signal events in the space of measurables due to the binding energy and the momentum distribution of the proton inside the nucleus. As the missing energy resolution becomes smaller, the fact that we measure the kinematics

Index i	1	2	3	4	5	6	7	8
$\mathbf{p}_i$	q_0	q	T_p	α_p	β_p	α_γ	β_γ	k
R_{xi}	0.45	1.06	1.26	0.16	0.19	0.17	0.17	1.04

Table 12. The sensitivity of the accidental background-to-signal ratio to detector failure.

of all three particles in the bremsstrahlung reaction becomes significant and the gain of useful information is mirrored in the behaviour of $D_{\sigma_i} R_x$.

15.4 Fault Tolerance

The gradients $D_{\sigma_i} R_x$ give us information on how an improvement or a deterioration of the detector resolution affects the background-to-signal ratio. It is equally important to study the effect of a total detector failure. In other words, we want to know what happens to R_x if we are unable to perform the measurement of one of the kinematic variables. Our toolbox from appendix B allows us to find answers to this question.

We will calculate R_x for the case, where the measurable $\mathbf{p}_i$ can not be determined. We will denote this value of R_x by R_{xi} in order to indicate which variable is not being measured. The results are listed in table 12. The model parameters (see equation 15.5) change from

$$N = 8, \quad n = 4, \quad \beta = 0.5123$$

to

$$N = 7, \quad n = 4, \quad \beta = 0.5705.$$

As one might have expected, R_x grows by a large factor (≈ 6) for the loss of any energy measurement k, q, or T_p. The momenta of the pion and proton are the most important from this point of view.

For the case of "no photon energy measurement", we have

$$R_x \quad = \quad 0.19 \quad \longrightarrow \quad 1.04$$

Index i	1	2	3	4	5	6	7
p_i	q_0	q	T_p	α_p	β_p	α_γ	β_γ
$D_{\sigma_i} R_x$	-0.10	0.07	0.66	0.05	0.04	0.01	-0.01
R_{xi}	1.64	1.06	5.50	0.98	1.10	0.99	0.98

Table 13. The sensitivity of the background-to-signal ratio to detector resolution and detector failure for the case of "no photon energy measurement".

which implies a substantial loss of discriminatory power against random background.

It will be argued in chapter 19 that the photon energy measurement is unreliable. We have just seen that this "failure" will increase the random background by a substantial amount, and it will be instructive to study the "no photon energy" scenario more closely. We have repeated the calculations of $D_{\sigma_i} R_x$ and R_{xi} for this case. The results are listed in table 13 and we can draw the following conclusions :

- The gradients $D_{\sigma_i} R_x$ have become very small (with the exception of $D_{\sigma_{T_p}} R_x$). This is expected, since we have lost experimental information.
- The failure of another detector component leaves R_x constant with the exception of the proton energy measurement. A loss of T_p increases the random background contribution by a factor of 5 to a value of $R_x = 5.5$.

We can conclude from this excercise that in the event of a failure to measure the photon energy, the proton energy becomes the most important piece of information in the suppression of the random background.

Chapter 16

Summary

We have seen the issues which come up in what is typically called "doing your homework". It involves a balance between the desire to do an interesting physics experiment and the restrictions imposed by technological limitations. We have introduced the kinds of background which need to be considered and how they can be dealt with experimentally. This in turn defines the accuracy of the measurement which can be achieved by the experiment. Tools have been developed to evaluate the background reliably and to relate the physics objective to design parameters of the experiment, in particular to the detector resolution function. We have been able to identify critical measurements and develop a fault-tolerant analysis strategy.

Part III

Detector Development

The next chapters concern themselves with the design and performance of the pion, proton and photon detector subsystems. An attempt is made to show how the demands on measurement resolution are translated into design specifications, or, if this should not be possible, how the chosen detection mechanism puts limits on the achievable resolution. We will also discuss the complications which were introduced by the magnetic field provided by the Helmholtz coils around the target.

Chapter 17

The Pion Spectrometer

The centerpiece of the pion spectrometer (figure 32) is PACMAN, a large dipole magnet with a pole size of 68 cm in width and 86 cm in length. The pole gap was set to 12 inches ($\approx$ 30 cm) for our experiment. The magnet is able to provide magnetic fields of up to $15 \cdot 10^3$ gauss at the center of the pole, but we were running it at a moderate $4 \cdot 10^3$ gauss. The spectrometer is completed by adding time-of-flight (TOF) counters and drift chambers which will measure the time and direction of the pion track before and after the magnetic field region. The extent of the magnetic field was limited by field clamps to essentially the size of the pole. This is not to say that the fringe field, which extends beyond the field clamps, can be entirely neglected. Before we go into technical details, we should discuss the principles on which spectrometer data are analysed and, in particular, develop a connection between achievable momentum resolution and design parameters.

17.1 The Tracking Model

The information which is measured directly is position and time. The latter serves to identify the particle (see chapter 13, page 64) and to reject background, while the position measurements describe the pion track.

A positively charged pion of momentum p in a uniform magnetic field of strength B follows a circular path with radius r :

$$r\,[\mathrm{cm}] = \frac{1}{0.29979}\,\frac{p\,[\mathrm{MeV/c}]}{B\,[10^3\,\mathrm{gauss}]} \tag{17.1}$$

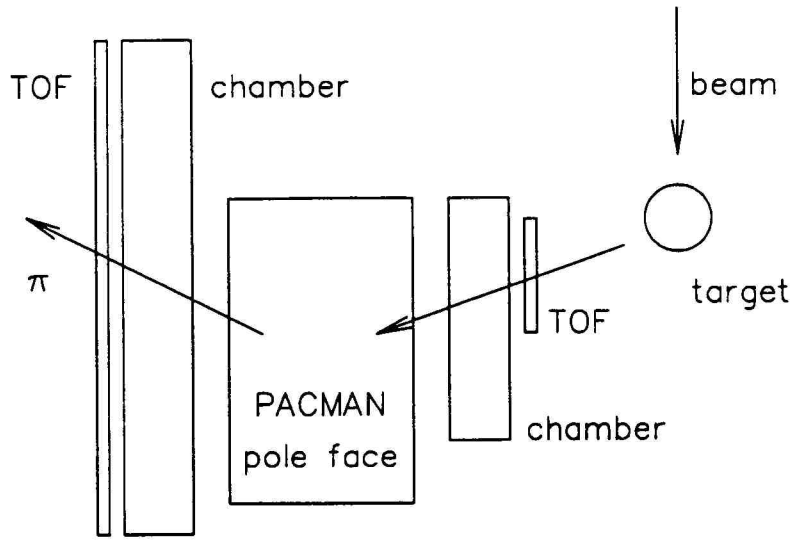

Figure 32. A schematic of the PACMAN dipole magnet.

where we have assumed that the direction of the magnetic field is normal to the direction of motion of the pion. For a non-uniform magnetic field, the path of the pion is a more complicated function of momentum.

The pion track through the spectrometer will be described by the vector of chamber coordinates

$$\vec{x} = \vec{f}(\vec{p})$$

It is to be compared to the set of position measurements $\vec{m}$ which can be expressed as

$$\vec{m} = \vec{f}(\vec{p_0}) + \vec{\varepsilon} \tag{17.2}$$

where $\vec{p_0}$ is the true momentum of the particle and $\vec{\varepsilon}$ are Gaussian measurement errors (in the absence of multiple scattering). An estimate of $\vec{p_0}$ can be obtained by minimizing the expression

$$R^2 = \sum_i \frac{[m_i - f_i(\vec{p})]^2}{\sigma_i} \tag{17.3}$$

where the σ_i are the mean standard deviations for each position measurement. This is simply a least-squares fit, and its solution, the momentum $\vec{p}$ for which R^2 is a minimum, is a measurement of the true momentum $\vec{p_0}$.

The central piece of this analysis is obviously $\vec{f}(\vec{p})$, the "track model", which predicts the track for any momentum $\vec{p}$. In cases where the magnetic field is mostly constant, $\vec{f}(\vec{p})$ can be derived from first principles. In general though, $\vec{f}(\vec{p})$ is expanded in suitable basis functions (often Chebycheff polynomials) and the expansion coefficients are fitted to tracks of known momentum. These tracks are either the result of an experimental calibration procedure or of calculations where the particle's path is numerically traced through the magnetic field. In the latter case, the dependence of the magnetic field on position must be known.

One example of such a track model is developed in appendix D and its performance is discussed there in detail.

For the purposes of this chapter, we note that the bend angle is given in general as

$$\alpha_B = 0.29979 \, \frac{1}{p} \int B \, dl \tag{17.4}$$

where

p	is the pion momentum
$\int B \, dl$	is the line integral over the magnetic field $\vec{B}$ normal to $\vec{p}$ along the path of the pion.

If we assume that $\int B \, dl$ is given to us, say in terms of $\vec{f}(\vec{p})$, we will find for the momentum resolution of the spectrometer

$$\left(\frac{\delta p}{p}\right) = \left(\frac{\delta \alpha_B}{\alpha_B}\right)$$

where $\delta\alpha_B$ is the measurement error for the bend angle. There are two contributions to the error $\delta\alpha_B$:

$\delta\alpha_x \propto \left(\frac{\delta x}{d}\right)$	is the error in α_B induced by the error in position. d is the distance over which such position measurements are made.

$\delta\alpha_{MS} \propto \frac{1}{\beta p}\sqrt{\frac{L}{L_R}}$ is the uncertainty in α_B due to multiple coulomb scattering (MS). L is the path length of the track, L_R the radiation length of the medium through which the particle moves (mostly air), p is the momentum of the particle and β the velocity of the particle divided by c, the speed of light.

The two contributions add in quadrature.

$$(\delta\alpha_B)^2 = (\delta\alpha_x)^2 + (\delta\alpha_{MS})^2 \qquad \left(\frac{\delta p}{p}\right)^2 \approx \left(\frac{\delta\alpha_B}{\alpha_B}\right)^2 \tag{17.5}$$

It is possible to display the dependence of the resolution $\frac{\delta p}{p}$ on the momentum p explicitly (recall that $\alpha_B \propto B\overline{L}/p$, where $B\overline{L}$ is the mean of $\int B\, dl$) :

$$\begin{aligned}\left(\frac{\delta p}{p}\right)^2 &\approx \frac{1}{\alpha_B^2}\left[\left(a\frac{\delta x}{d}\right)^2 + \frac{\overline{L}}{L_R}\left(b\frac{1}{\beta p}\right)^2\right] \\ &= \left(\frac{c}{B\overline{L}}\right)^2\left[a^2\left(\frac{\delta x}{d}\right)^2 p^2 + b^2\frac{\overline{L}}{L_R}\left(1+\frac{m^2}{p^2}\right)\right] \\ &= f\left(B\overline{L}, \frac{\delta x}{d}, \frac{\overline{L}}{L_R}, p\right)\end{aligned} \tag{17.6}$$

where a, b and c are normalization constants and m is the mass of the particle.

This expression does have a minimum at $p = p_{min}$, which is a function of the parameters. The design of the spectrometer, which is constrained by the desired momentum resolution and acceptance as well as available resources, thus entails choices for $B\overline{L}$, δx, d, L_R and p_{min}.

17.2 The Drift Chambers

The principal drift chamber cell is sketched in figure 33, which shows the cathode plane and anode and cathode wires. A charged particle traversing the cell causes ionization along its path. The freed electrons accelerate towards the anode and cause the development of an avalanche. The sudden appearance of electrical charge can be seen as a voltage signal which travels down the length of the anode wire and is eventually detected and amplified with appropriate electronics. The time between

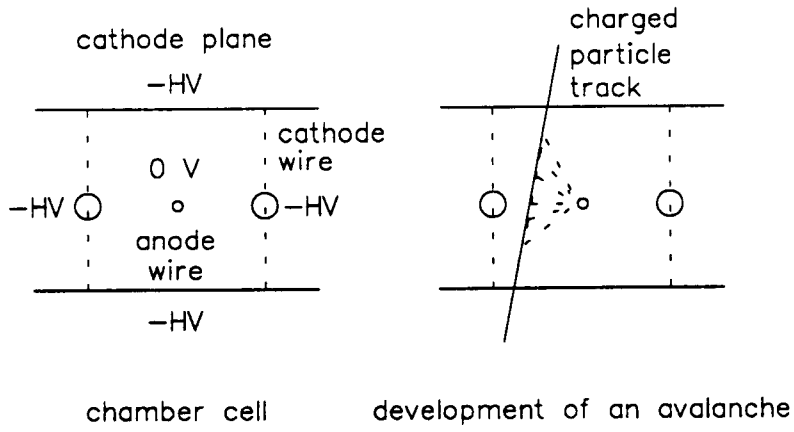

Figure 33. Principle mode of operation for a drift chamber cell.

the passing of the charged particle and the formation of the signal on the anode wire is of order 100 ns and depends on the drift velocity of electrons in the chamber gas. A measurement of this time relative to a reference signal, which is provided by the time-of-flight counters, allows us to deduce the distance between the track and the anode wire. In order to determine both direction and position of the track in one plane uniquely, we need hits in several cells as shown in figure 34. Notice that the cells in planes z_1 and z_3 are shifted relative to planes z_2 and z_4 by one half cell size. This is necessary in order to resolve the "left-right ambiguity". Since one cell measures only distance, we need information from other cells to determine on which side of the anode wire the particle went by. Staggering the cells in the manner shown above provides that information.

The geometry of our cell is square, which implies that the electric field in the corners is slightly smaller than between wires. This can be seen by looking at the distribution of drift times from tracks which only hit the corner of a cell, compared to more direct hits (see figure 35). As a consequence, care has to be taken in how hits are associated to form tracks as well as in how timing information is transformed into position information. Since these operations are quite specific to the type of chamber, we will discuss them in appendix C.

The dimensions of the chambers and their performance in terms of spatial

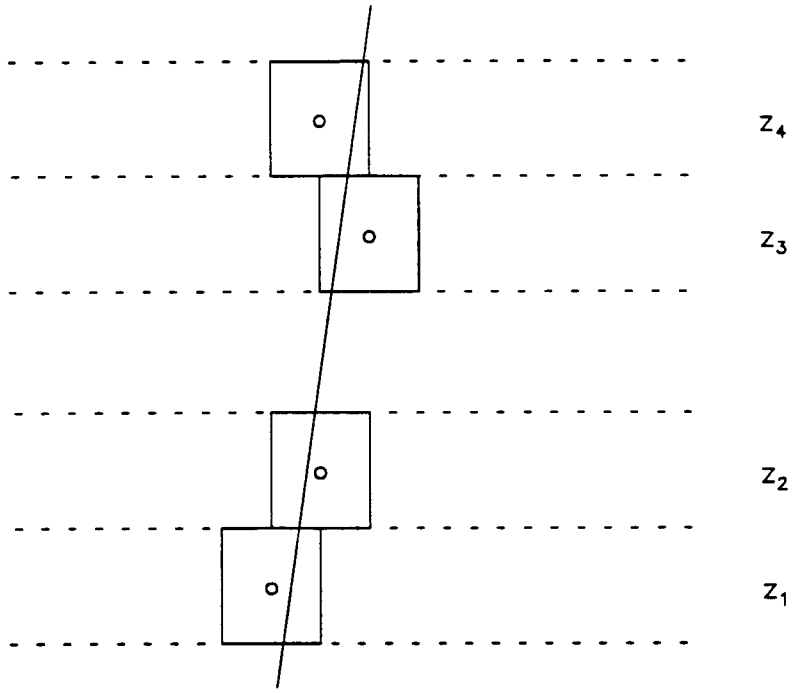

Figure 34. Typical hit pattern for a complete measurement of track position and direction.

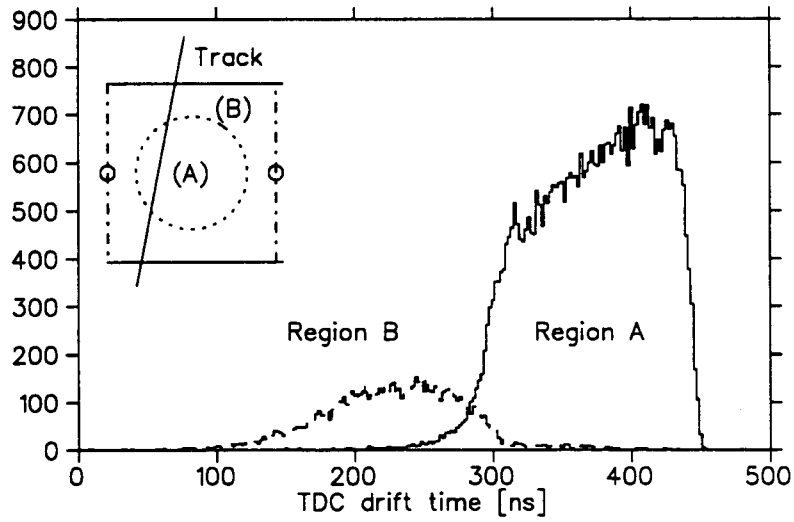

Figure 35. Distribution of drift times for direct (solid line) and grazing (dashed line) hits.

Chambers	*front*	*back*
Size = active area	Δx : 60 cm	Δx : 200 cm
	Δy : 20 cm	Δy : 60 cm
High Voltage	1.62 kV	1.72 kV
Cell size = anode wire spacing	1.2 cm	2.0 cm
$d = b + 2a = z_4$ - z_1	10.9 cm	30.8 cm
$a = z_2$ - $z_1 = z_4$ - z_3	2.4 cm	2.0 cm
$b = z_3$ - z_2	6.1 cm	26.8 cm
Position resolution δx	0.4 mm	0.7 mm
Angular resolution $\delta\alpha = f(\delta x, d, a)$	0.26°	0.14°
Efficiency per plane	x : 0.988	w : 0.983
	y : 0.977	v : 0.979
Overall track finding efficiency	0.73	

Table 14. Dimensions of the drift chambers and their performances in terms of resolution and efficiencies.

resolution δx and efficiencies are summarized in table 14.

The front chambers measure coordinates x and y, whereas the back chambers measure w and v, which are obtained by rotating x and y by 45 degrees. Each coordinate requires that at least three out of four planes show a hit. A full pion track consists of at least 12 and at most 16 hits (4 coordinates x, y, w, v times 3 or 4 hits per coordinate). The efficiencies per plane are based on how many events show 3-hits-out-of-4 compared to 4-hits-out-of-4. The overall track finding efficiency is based on an analysis of elastic pion-proton scattering events.

17.3 The Performance of the Pion Spectrometer

The acceptance of the spectrometer for pions of momentum p and scattering angle α (we consider only events which can be traced back to the target) can be calculated

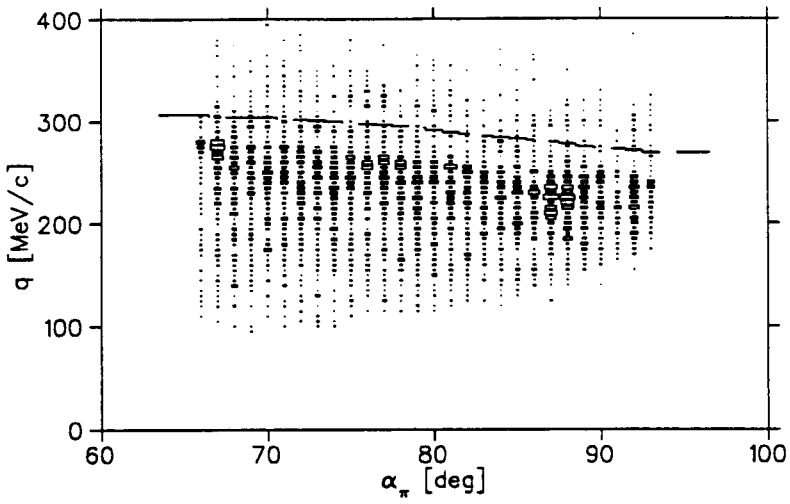

Figure 36. Acceptance of the pion spectrometer in the variables p and α.

on the basis of our track model which is discussed in appendix D. The result is shown in figure 36. The dashed line identifies elastic pion-proton scattering events.

Appendix D also discusses the momentum resolution $\frac{\delta q}{q}$ which has been achieved with this spectrometer and our version of the track model. We can measure an effective pion momentum resolution by looking at tracks from elastic $\pi^+ p$ scattering events. The momentum of those pions is defined in terms of the initial pion energy T_0 and the measured pion scattering angle α_π. The resulting momentum resolution, which includes the intrinsic momentum resolution of the spectrometer, the uncertainty in T_0, $\frac{\delta q_0}{q_0}$, and the uncertainty in α_π, $\delta\alpha_\pi$, is given by

$$\left(\frac{\delta q}{q}\right)_{ES} = \frac{q - q_{ES}}{q_{ES}} = 4.3\ \%\ \text{FWHM}$$

The resolution is constant over the acceptance of the spectrometer.

The momentum of the pion is also needed to trace the track back to its origin in the target, since the frozen spin target magnetic field is not small. The distribution of vertices in the target projected onto the beam axis is shown in figure 37. The error on the position of the vertex is estimated to be less than 3 mm FWHM.

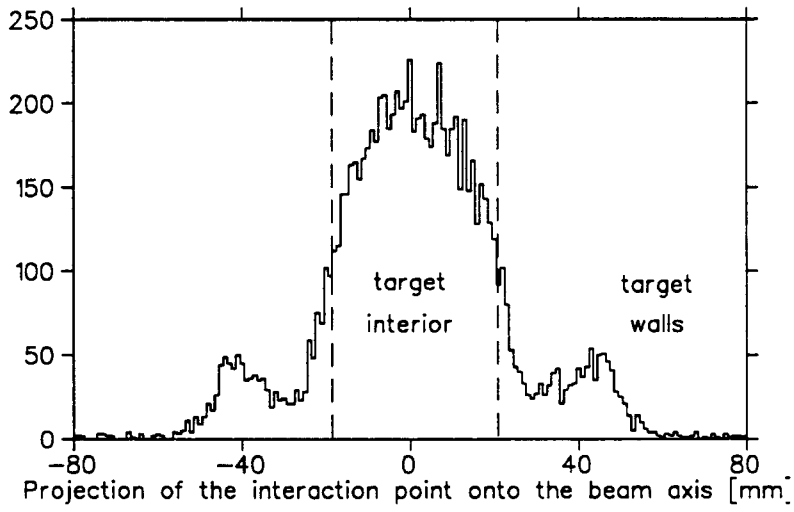

Figure 37. Distribution of vertices for the frozen spin target.

Chapter 18

The Proton Detector

The proton detector provides a good example of how a seemingly small oversight - a 30 gauss magnetic field at the position of the detector - can turn into a big problem for the data analysis.

In general, working with plastic scintillators is a straightforward procedure. The principal detection mechanism is the transformation of energy lost through ionization into visible light. A particle of charge ze and mass m (much larger than the electron mass) moving through a medium with incident speed βc, dissipates energy principally via interactions with the electrons of the medium. The mean rate of energy loss per unit pathlength x is given by the Bethe-Bloch equation

$$\frac{dE}{dx} = \frac{DZ_{med}\rho_{med}}{A_{med}} \left(\frac{z}{\beta}\right)^2 \left[ln\left(\frac{2m_e\gamma^2\beta^2c^2}{I}\right) - \beta^2\right] \tag{18.1}$$

where

D = $4\pi N_A r_e^2 m_e c^2 = 0.3070$ MeV cm^2/g

m_e = the mass of the electron

ρ_{med} = the density of the medium

Z_{med} = the charge number of the atoms in the medium

A_{med} = the atomic number of the atoms in the medium

I characterizes the binding energy of the electrons of the medium

and where we have neglected atomic and relativistic corrections.

In a plastic scintillator, a fraction of this energy serves to excite certain complex molecules which then decay back to the ground state via the emission of a photon. The amount of light per unit pathlength follows [49]

$$\frac{dL}{dx} \propto \frac{dE}{dx} \left[1 + kB \left(\frac{dE}{dx} \right) + C \left(\frac{dE}{dx} \right)^2 \right]^{-1} \tag{18.2}$$

where the non-linear dependence on the energy loss $\frac{dE}{dx}$ describes saturation effects in the scintillator. The light is then detected with a photomultiplier tube which returns a signal which, in turn, is measured with an analog-to-digital converter (ADC) (see appendix E). The total amount of energy lost in the scintillator is related to the ADC measurement by

$$\begin{aligned} E &= E(L) \\ L &= \alpha \, (\text{ADC} - \text{Pedestal}) \end{aligned} \tag{18.3}$$

where $E(L)$ is obtained by integrating equations 18.1 and 18.2 simultaneously, α is a gain factor to be determined experimentally and the "pedestal" is the output of the ADC which corresponds to no signal from the photomultiplier tube.

Since the detection process is statistical in nature (with a Poisson distribution), the resolution of the measurement is given by

$$\frac{\delta E}{E} = A \frac{1}{\sqrt{E}}$$

where A depends on how the light is collected and guided to the phototube and on the operating parameters of the phototube.

The proton detector for the bremsstrahlung experiment is sketched in figure 38. The total energy of the proton coming from the target is measured by plastic scintillator blocks which span 4 degrees in the horizontal plane and $\pm$ 9 degrees in the vertical plane and which are long enough (14 cm) to stop protons of 135 MeV kinetic energy. The 0.675 cm thick counter in front of the array serves to measure the differential energy loss $\frac{dE}{dx} \approx \frac{\Delta E}{\Delta x}$ which will be used to identify the particle as a proton (see chapter 13 section 1 on page 64).

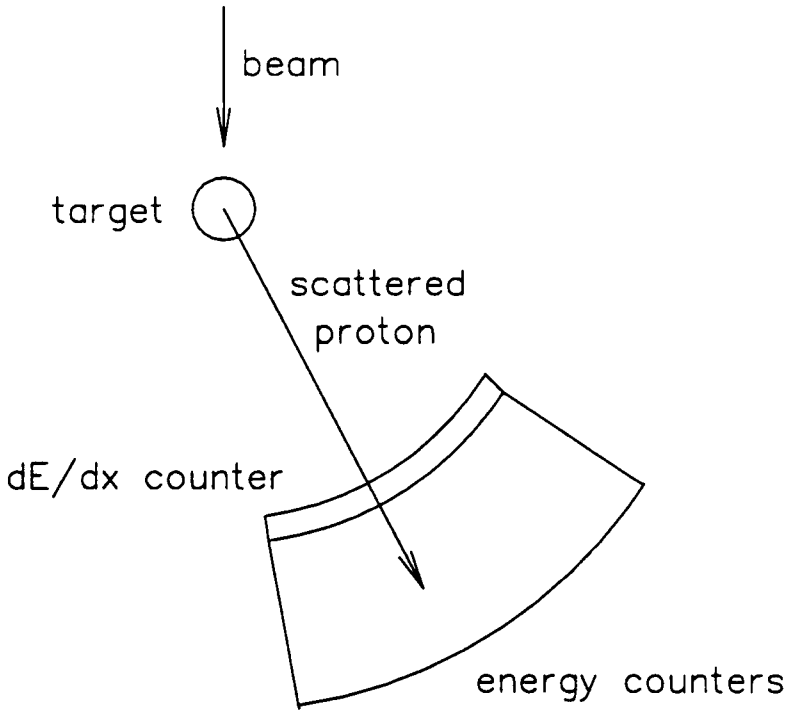

Figure 38. Schematic view of the proton detector.

18.1 The Problem

The measurement of the proton energy requires the knowledge of the calibration constant in equation 18.3. This number must be determined experimentally and furthermore, as is shown in appendix E, it is not really a constant but depends on operating conditions (count rate, high voltage, temperature, time). What is typically done, and what has been done in this experiment as well, is to set aside a period of beam time dedicated to the measurement of α - called calibration - and operating conditions are monitored at regular intervals during the remaining time.

We were aware in this experiment of the value of the magnetic field at the position of the phototube - about 30 gauss, which is very large for this application. So additional magnetic shielding was a[illegible]led and the phototubes were mounted in a particular position relative to the fie[illegible] direction (see appendix E) to lessen the effect of the magnetic field on tube operations. As far as diagnostic data available during the running of the experiment were concerned, the detector seemed to work

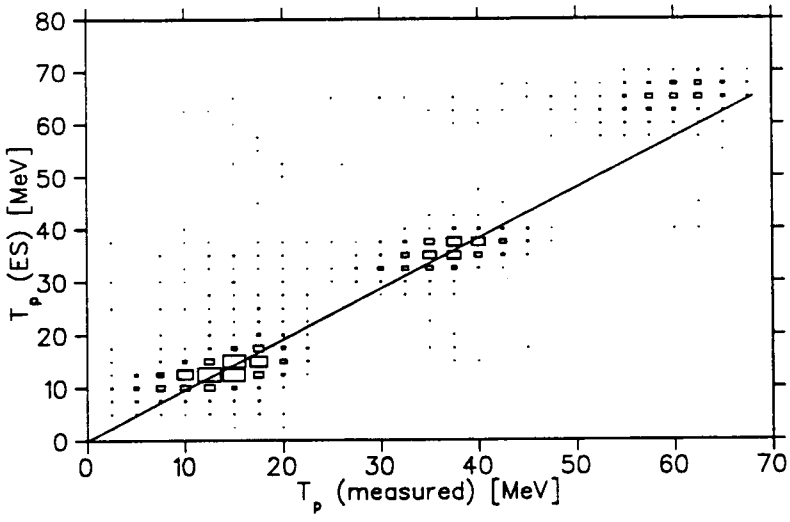

Figure 39. Evidence for the energy-dependence in the gain for the proton detector based on elastic $\pi^+ p$ scattering data off the liquid hydrogen target. The solid line represents a linear relationship between measured and expected proton energy.

well.

However, it became clear later in the off-line data analysis - after the experiment was completed - that the magnetic field had not just affected the overall gain but that the response of the detector now depended on energy as well, i.e. the gain α was a function of energy rather than a constant. This is demonstrated with data in figure 39. Since this effect only became clear after the detector had been taken apart for storage, an energy-dependent calibration had to be found based on the data alone.

We will look at this procedure in some detail because it shows how an apparently trivial application can become a very non-trivial analysis problem.

The data taken with the frozen spin target contain two classes of events (among others), which form the basis for the calibration :

- Elastic pion-proton scattering, which allows us to calculate the kinematics at the interaction point. Unfortunately, the angle of the proton is limited to the range 30 – 50 degrees by the acceptance of the pion spectrometer.

Furthermore, the range of proton energies is also limited, this time by the angular width of a given telescope (which was 4 degrees). Elastic scattering can provide a calibration at only one energy $L^{ES}_{calculated}$ per telescope for the five (of eleven) telescopes which see elastically scattered protons.

- Pion absorption on a nucleus $\pi\mathcal{N} \rightarrow ppX$, where X can be anything. This reaction, which comprises 60 % of all the data taken on the frozen spin target, produces protons with energies from zero up to $\approx$ 100 MeV over the full angular range of the proton detector. The energy of the proton at the interaction point cannot, however, be calculated from available kinematical data. These events will be the basis for a self-consistent calibration procedure.

The calibration procedure is based on the observation that the variable PPID, which was used earlier for particle identification,

$$\text{PPID} = \frac{dL_{measured}}{dL(L_{measured})} = \frac{\alpha_0\, dL(L_{proton})}{dL(L_{measured})} \tag{18.4}$$

is supposed to be a constant. L is the amount of light seen by the plastic scintillator detectors (recall equations 18.2 and 18.3), dL stands for the amount of light seen by the $\frac{dE}{dx}$ counter (which is the thin plastic scintillator counter covering the proton detector), and α_0 is the gain calibration for the same counter. Experimentally, PPID turns out to be a function of $L_{measured}$, which leads us to conclude that

$$L_{measured} \neq L_{proton}$$

We can define L_{proton} by reversing the above argument :

$$L_{proton} = dL^{-1}\left(dL(L_{measured})\, H(L_{measured})\right) \tag{18.5}$$

where $H(L_{measured})$ is taken directly from experimental data (from a plot of PPID against $L_{measured}$) and $dL(L_{measured})$ is defined in appendix F.

It is necessary to check this procedure on the following observations :

- The behaviour of PPID(L, L') for small L' is given by

$$\lim_{L' \rightarrow 0} \left\{ \text{PPID}(L, L') \equiv \frac{\alpha_0\, dL(L)}{dL(L')} \right\} = \alpha_0 \tag{18.6}$$

and independent of L', i.e. independent of the gain α which we don't know (recall $L' = \alpha(\text{ADC} - \text{Pedestal})$). The limit applies to all telescopes.

- We can form another variable based on elastic scattering data alone :

$$\text{CPID} \equiv \frac{dL_{measured}}{dL(L^{ES}_{calculated})} = \alpha_0 = \frac{\alpha_0\, dL(L^{ES}_{proton})}{dL(L^{ES}_{calculated})} \tag{18.7}$$

We did claim before that $L^{ES}_{calculated}$ can be reliably calculated. This statement has to be modified.

The proton travels a few mm up to a few cm in the frozen spin target which is quite dense ($0.59\ \frac{\text{g}}{\text{cm}^3}$). At small energies the energy loss in the target becomes substantial and it is necessary to know the interaction point well. A systematic error in the determination of the beam position on target, z_0, leads to a corresponding systematic error in $L^{ES}_{calculated}$ and an energy dependence in the variable $\text{CPID}(L^{ES}_{calculated})$.

After many attempts to define the interaction point consistently and without bias, we have settled on the following procedure. The pion track points back to the vertex. We also know the proton angle for elastic scattering and can define the vertex by intersecting the pion and proton tracks. This procedure depends on a knowledge of the FST magnetic field which bends the proton by up to 6 degrees. Figure 40 shows that z_0 varies over time by a few mm. This is quite consistent with the properties of the beam line.

We can define α_0 by looking at CPID for large proton energies. The uncertainty in z_0 will have a small effect on $L^{ES}_{calculated}$ and CPID will be very close to 1. In practice, we have defined α_0 based on CPID for $T_p > 50$ MeV. The result is shown in figure 41. It is obvious that α_0 also varies with time.

Given a clear understanding of the elastic scattering data, we can deduce another constraint on the proton energy calibration :

$$\lim_{L_{ES}\to\infty}\left\{\text{CPID} \equiv \frac{\alpha_0\, dL(L_p)}{dL(L^{ES}_p)}\right\} = \alpha_0 = \lim_{L'\to 0}\left\{\text{PPID} \equiv \frac{\alpha_0\, dL(L_p)}{dL(L')}\right\} \tag{18.8}$$

The first of these observations is confirmed by the data. However, the second is not, as is shown in figure 42.

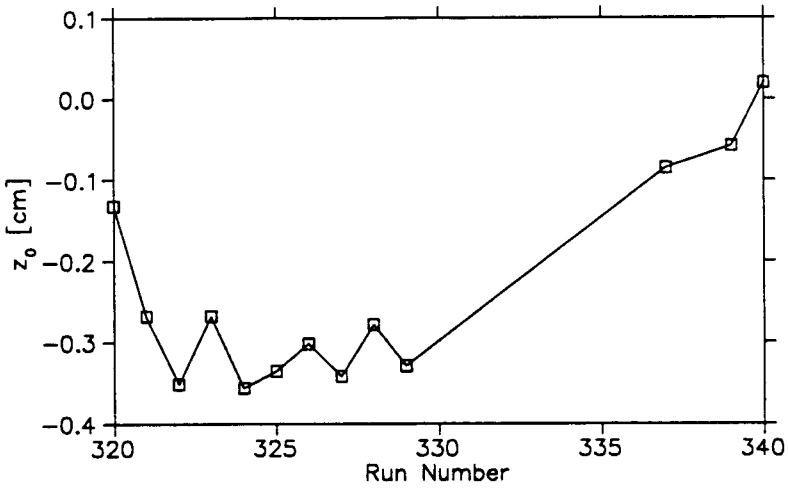

Figure 40. The position of the beam spot on target as a function of run number.

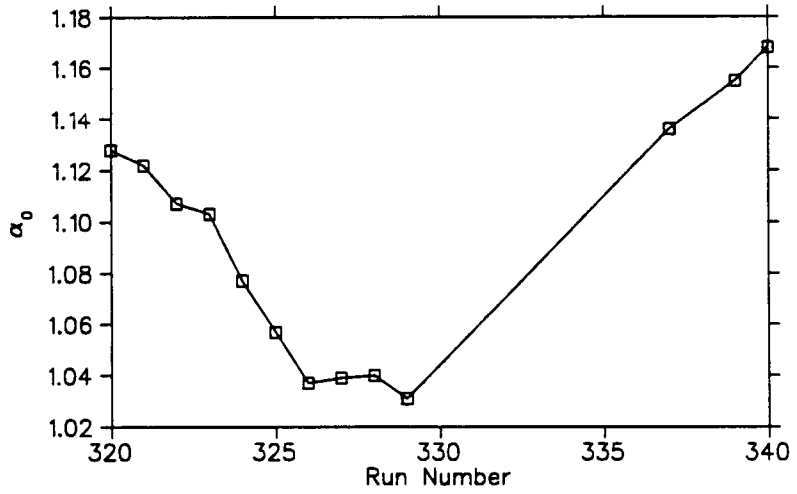

Figure 41. The $\frac{dE}{dx}$ gain constant α_0 as a function of run number.

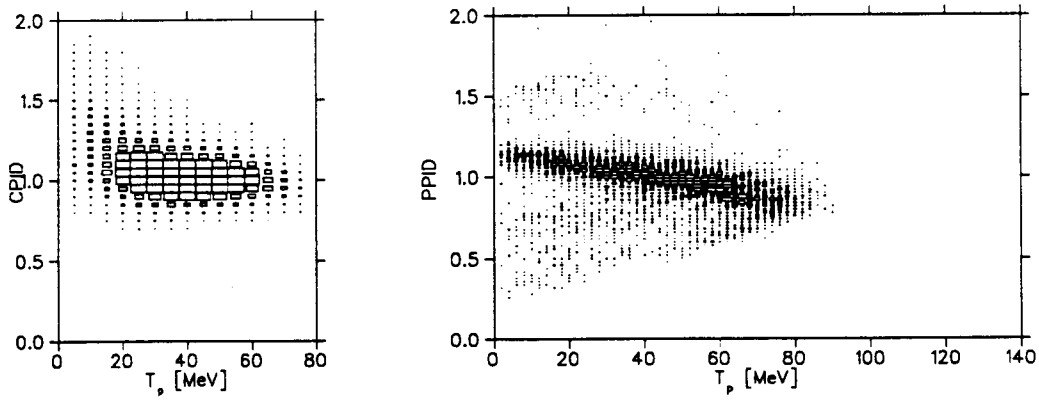

Figure 42. Experimental evidence for the inconsistency between CPID and PPID.

Let us summarize :

- α_0 is fixed by the high-energy behaviour of CPID(L').
- The non-linear response for the total energy becomes linear at small energies (i.e. small signals) given our understanding of phototube operations (appendix E).
- PPID(0) $> \alpha_0$, which is inconsistent with equation 18.8.

In order to match the CPID and PPID behaviour, we are forced to conclude that the response of the $\frac{dE}{dx}$ counter is *underestimated at low energies.*

There are two possible explanations :

- The $\frac{dE}{dx}$ measurement also suffers from a non-linear response. The qualitative behaviour is shown in figure 43.
- The calculation of the energy lost in the $\frac{dE}{dx}$ counter as a function of the total energy is based on tables which summarize all available measurements on $\frac{dE}{dx}$ for a wide range of proton energies. The errors on these data points can be as large as 10 % at low energy and systematic errors of that size could explain the discrepancy between CPID and PPID (this is another reason why α_0 is defined in terms of CPID($T_p > 50$ MeV)).

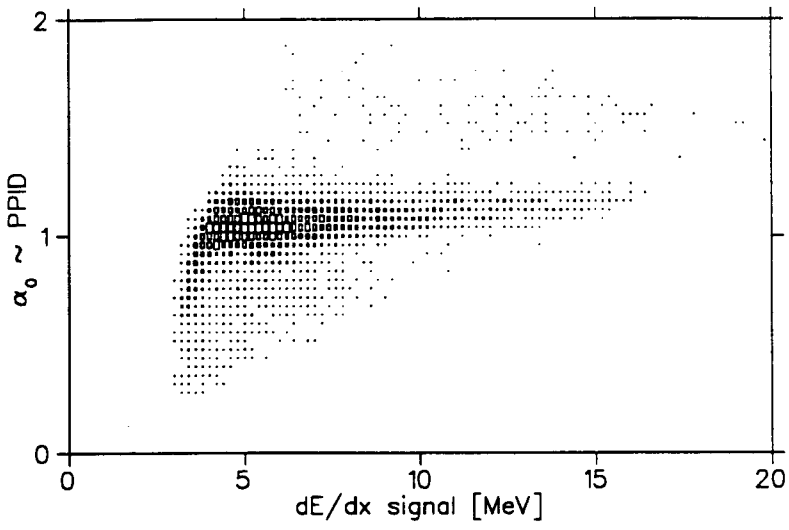

Figure 43. Qualitative behaviour of a possible non-linear response in the $\frac{dE}{dx}$ measurement.

In the absence of firm evidence for one or the other of these hypotheses, the following algorithm has been adopted as proton energy calibration :

$$z_0 \equiv f(\overline{\alpha_\pi}, \overline{\alpha_p}) \quad \text{based on elastic scattering data}$$
$$\alpha_0 \equiv f(\text{CPID}) \quad \text{at large } L_p^{ES}$$

$$\text{PPID}(L') = H(L') = \begin{cases} 1 & \text{for } L' \leq 30 \text{ MeV} \\ \text{PPID}(L') & \text{for } L' > 30 \text{ MeV} \end{cases}$$

$$L_p = dL^{-1} \{dL(L')\ H(L')\}$$

We have already seen that z_0 and α_0 change over time. So does $H(L')$! At L' = 100 MeV this variation can be as large as 10 %. The achieved energy resolution can only be estimated based on elastic pion-proton scattering data.

$$\frac{\delta E}{E} \approx \frac{2.5\ \%}{\sqrt{E\,[\text{GeV}]}} \tag{18.9}$$

Chapter 19

The Photon Detectors

The principles of operations are similar to those for the proton detector, except that now our scintillator is a NaI crystal instead of organic molecules. The light yield is about a factor of three larger than for plastic scintillator, and the signal has a decay time of order 300 ns.

The long decay time of the signal requires large ADC integration times (of order 600 ns), which has important consequences for the control of pile-up and baseline shifts (appendix E). In the bremsstrahlung experiment, not much time was spent dealing with this issue due to the expected low count rate. As it turned out though, the unanticipated large background rate of random "photons" (see section 12.1) did cause sizeable variations in the baseline, as is shown in figure 44. What is plotted is the distribution of ADC values for TINA for events which were triggered by some other detector, i.e. we are looking at the pedestal. One would expect to see an ADC value corresponding to zero input signal. High count rates in conjunction with a slowly decaying signal broaden the pedestal. Since the shift in the pedestal for any given event cannot easily be measured, the broadening will contribute to the energy resolution of the detector. The tails of the distribution in figure 44 extend up to the highest energies measured in this experiment. Such a large shift in random coincidence with an inelastic $\pi^+ p$ scattering event can look like a good bremsstrahlung signature and must therefore be considered as a source of background.

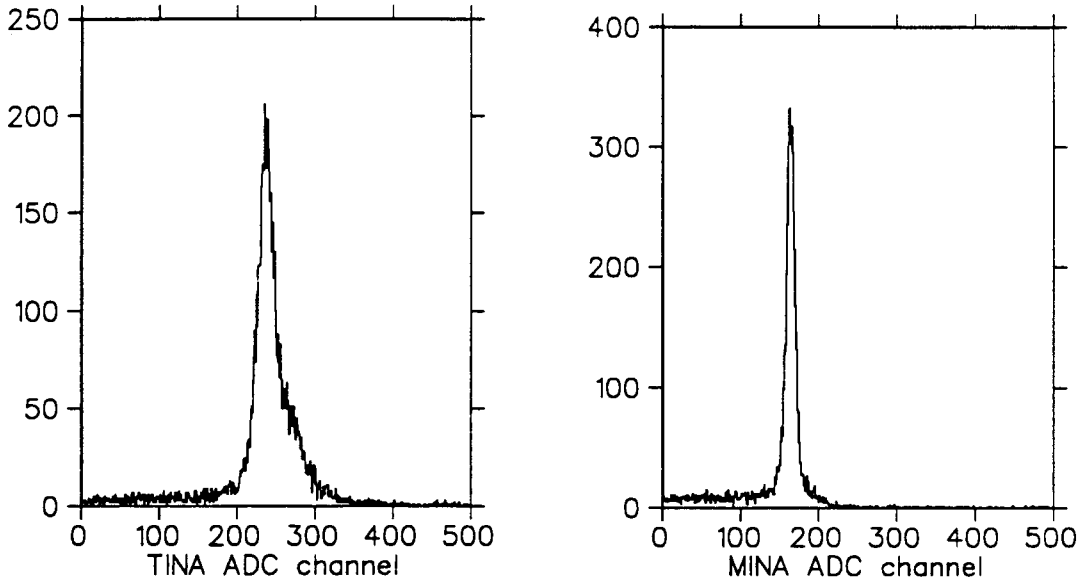

Figure 44. The width of the pedestal indicates the amount of pile-up one has to worry about.

The NaI detectors are calibrated with photons coming from the reactions of negative pions stopped in a liquid hydrogen target.

$$\pi^- p \rightarrow \pi^0 n, \quad \pi^0 \rightarrow \gamma\gamma \tag{19.1}$$

$$\pi^- p \rightarrow \gamma n \tag{19.2}$$

The resulting spectrum is shown in figure 45. The energy calibration of the detector is typically based on photons from the reaction 19.2, since their energy is well defined (E_γ = 129 MeV). The large background in the spectrum is due to electrons which contaminate the π^- beam and scatter off material around the target or air into the detector (without setting off the veto counter in front of the NaI detector).

A non-zero magnetic field is a much bigger problem for NaI detectors than it is for plastic scintillator detectors. The photo tubes have to be mounted against the backside of the crystal with the photo cathodes touching the surface for good light collection (i.e. no light guides). This makes it difficult to shield effectively against magnetic fields, unless, as was done in this experiment, the whole detector is encased in a steel box.

We made attempts to monitor the gain of the photon detectors with a refer-

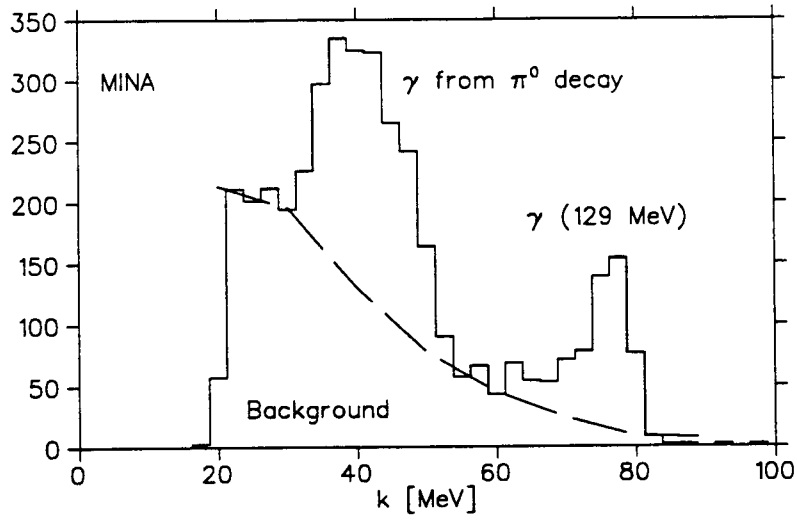

Figure 45. Photons coming from the reactions of a π^- stopping in a liquid hydrogen target.

ence signal provided by small LED's mounted close to the photo tubes. Technical difficulties and a high count rate causing pile-up and a possible change in gain lead us to doubt the validity of the π^- based energy calibration. As in the case of the proton detector, we had to look for other means to define the energy of the photons. The tool which will give us this energy calibration is, once again, the relation between total energy and the $\frac{dE}{dx}$ measurement for a proton entering the detector. The reaction which gives us these protons is pion absorption on a nucleus :

$$\pi^+ \mathcal{N} \rightarrow ppp\mathcal{N}'$$

Figure 46 shows the distribution of the equivalent of PPID (equation 18.4) for MINA as a function of the measured proton energy. The lack of a dependence of this variable on energy gives us the gain calibration with an estimated systematic error of less than 10 %.

The real problem with the photon detectors is that the two ways of calibrating the energy, $\pi^- p \rightarrow \gamma n$ and PPID(L_p, L), result in gain constants which differ by a factor of 2 ! Such a big loss in gain between the π^- run on the LH_2 target and the data-taking runs on the frozen spin target suggests that the detectors must have been operating under extreme conditions (high magnetic fields, background

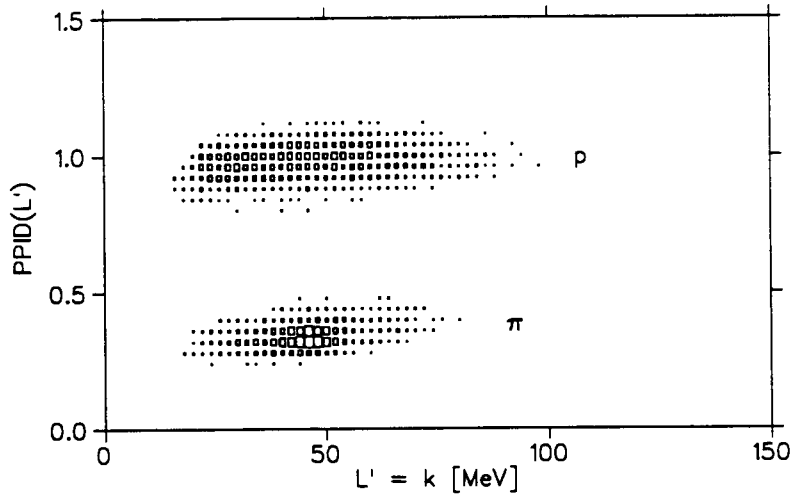

Figure 46. PPID(L') implemented for the photon detector MINA.

rates, average signal current). The uncertainty on the photon energy measurement is therefore unknown.

Part IV

Analysis

The analysis of the data, which is to follow in the next chapters, is based on the kinematics of hypothetical reaction mechanisms "at the interaction point" inside the target.

It is assumed that

- all detectors are properly calibrated,
- all particles are properly identified,
- the measured kinematic variables are well defined and have been projected back to the interaction point (i.e. the tracks have been traced through the frozen spin target magnetic field back to the target and energy losses have been taken into account).

We are therefore in a position to directly compare the experimental observables with the predicted kinematic variables.

The cuts which have been applied to the data up to this point are listed in appendix A.

Chapter 20

Pion-Proton Elastic Scattering

About one third of all the data on the frozen spin target was based on a pion-proton double coincidence which was scaled down by a factor of $2^7 = 128$, i.e. only every 128th coincidence was written to magnetic tape. The distributions of events in the measured variables $\frac{q-q^{ES}}{q}$ and $(\alpha_p - \alpha_p^{ES})$ are shown in figures 47 and 48, where the elastic kinematic variables - q^{ES} and α_p^{ES} - are functions of the initial beam energy T_0 and the pion scattering angle α_π only. The data clearly show an elastic contribution with tails coming from quasi-free scattering.

The elastic $\pi^+ p$ scattering cut, which will later also be applied to the bremsstrahlung candidates, is defined as

$$\mathrm{DG4} \equiv \sqrt{\left(\frac{\frac{\delta q}{q}}{2.355\sigma_q}\right)^2 + \left(\frac{\delta\alpha_p}{2.355\sigma_{\alpha_p}}\right)^2} \leq 1.5 \qquad (20.1)$$

The distribution of events in this variable is shown in figure 49.

Given this selection criterion, we can immediately look at kinematic variables which might be of interest to the bremsstrahlung analysis :

- The missing energy $T_{miss}^{\pi p} = T_0 - T_\pi - T_p$ which should be equal to the photon energy k for bremsstrahlung data. The resolution $\delta T_{miss}^{\pi p}$ for elastic scattering will give a lower bound on the resolution for the equivalent variable for bremsstrahlung, $T_{miss}^{\pi p\gamma} = T_0 - T_\pi - T_p - k$.

- The longitudinal momentum balance PL along the direction of the photon, i.e. along an axis pointing to the center of the photon detector.

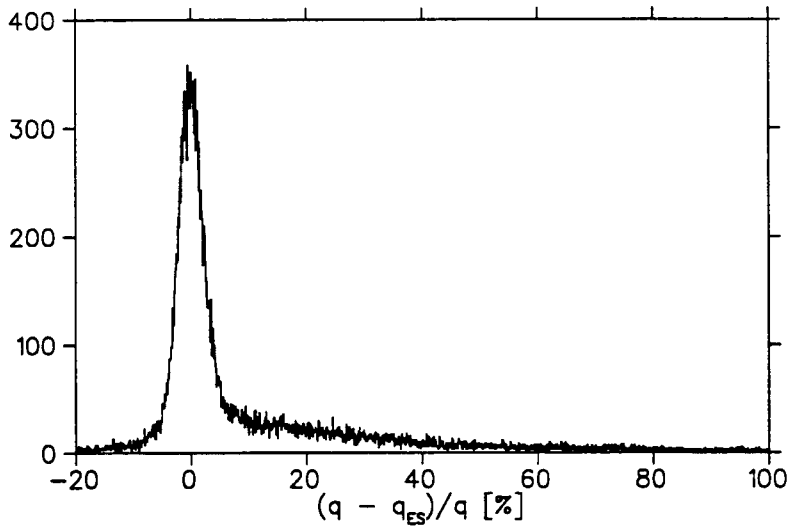

Figure 47. The distribution of $\left(\frac{\delta q}{q}\right)_{ES}$ based on events with a pion-proton coincidence.

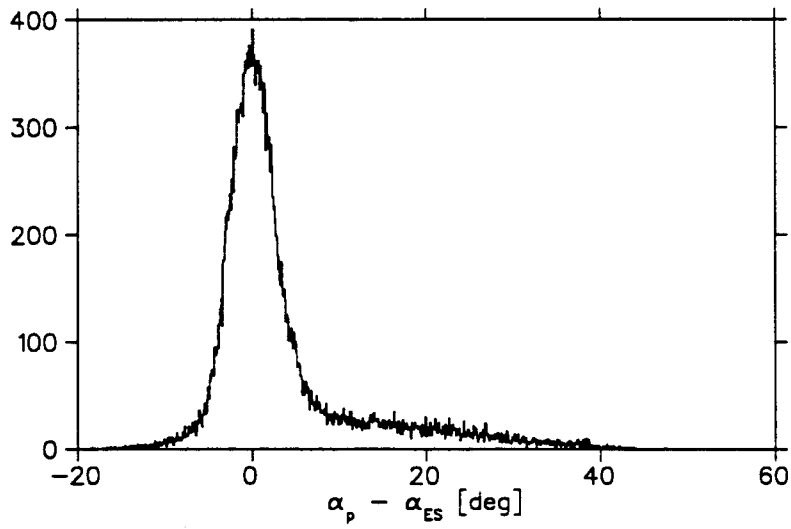

Figure 48. The distribution of $(\alpha_p - \alpha_p^{ES})$ based on events with a pion-proton coincidence.

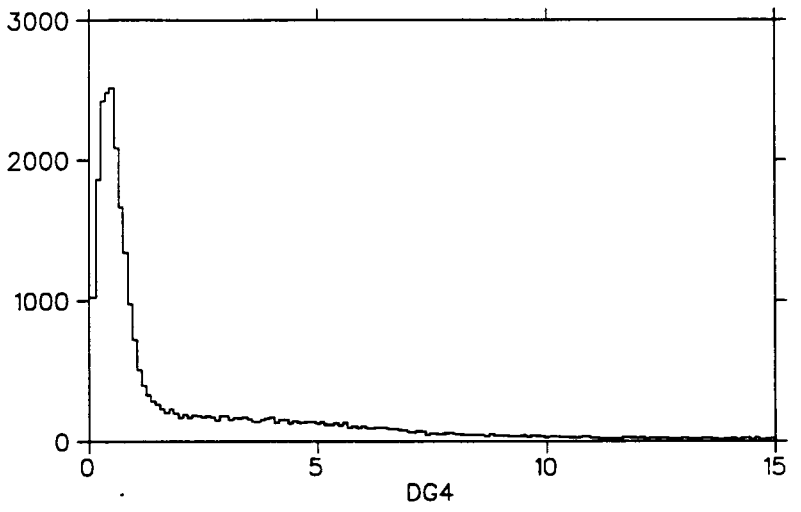

Figure 49. The distribution of DG4 based on events with a pion-proton coincidence.

- The transverse momentum balance PT normal to the direction of the photon.
- The mass of the target particle

$$\mathrm{MTGT}_{\pi p} = \sqrt{(E_0 - E_\pi - E_p)^2 - (\vec{p}_0 - \vec{p}_\pi - \vec{p}_p)^2} - m_p$$

The distributions for those variables are shown in figure 50 for elastic $\pi^+ p$ data and they will set the scale for an analysis of the bremsstrahlung data.

It is straightforward to determine the asymmetry $\mathcal{A}$ for elastic pion-proton scattering following the developments in appendix G. The random background N_x turns out to be negligible and we have set it to zero. The data tapes (labeled by run numbers) which were utilized for this analysis are listed in table 15. The measured asymmetry is listed as a function of the pion scattering angle α_π in table 16 and compared to the theoretical prediction (see figure 51). The theoretical calculations are based on a phase shift analysis from reference [54]. The acceptance bin is $\Delta\alpha_\pi = 2°$.

We can conclude from the results that we were able to accurately measure the elastic pion-proton scattering asymmetry with this experiment and that there will be no experimental bias in the determination of the bremsstrahlung asymmetry.

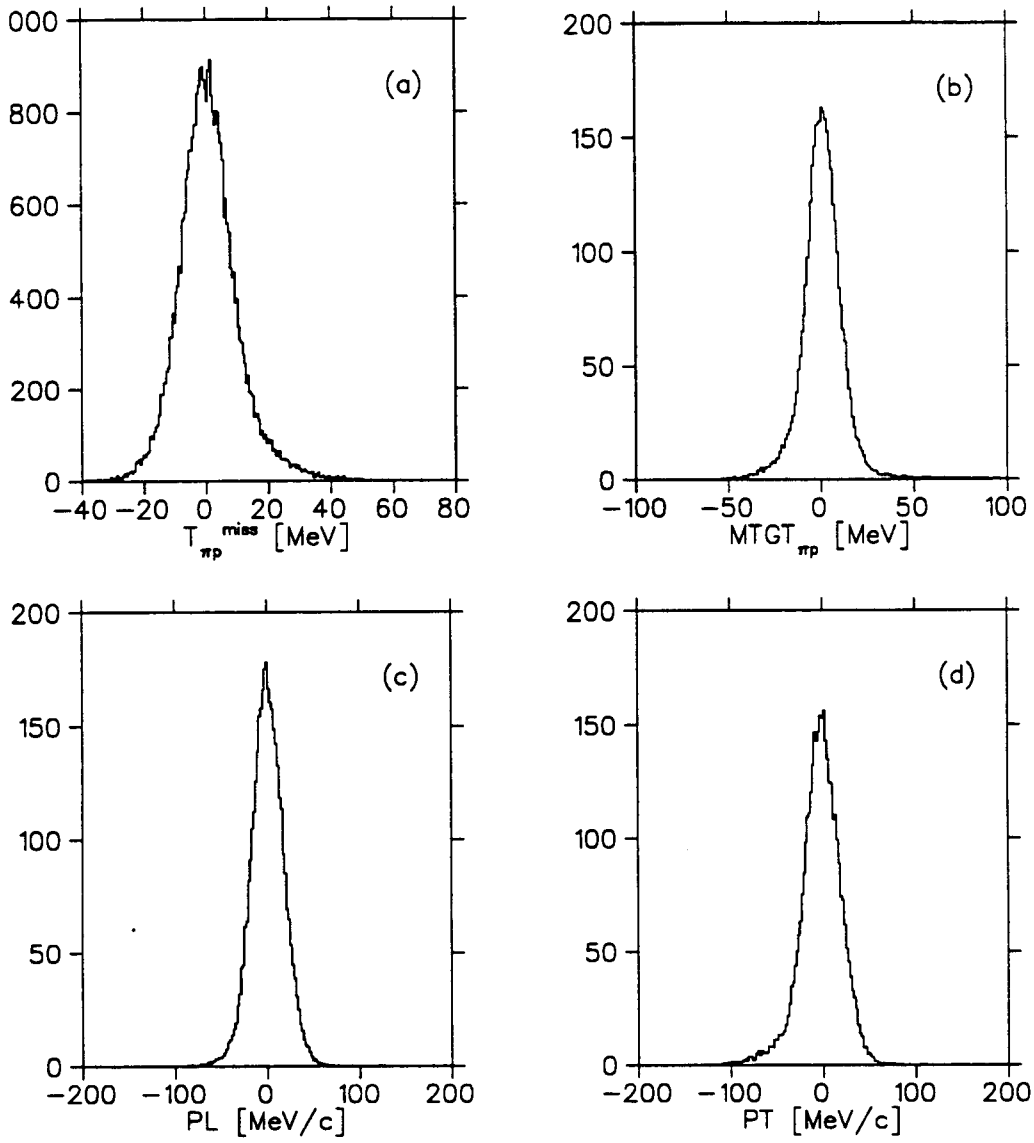

Figure 50. Distributions of events for variables, which are of interest to the bremsstrahlung analysis, based on elastic $\pi^+ p$ scattering data. (a) $T^{\pi p}_{miss}$, (b) $\mathrm{MTGT}_{\pi p}$, (c) PL, (d) PT.

Run number	$\mathcal{P}$ [%]	M_0 [MHz h]	ϵ
$\frac{1}{2}$ R 324	-75.7	10.1	0.999
$\frac{1}{2}$ R 325	-75.3	9.8	0.990
$\frac{1}{2}$ R 326	-74.9	9.9	0.989
$\frac{1}{2}$ R 327	-74.5	9.8	0.987
R 328	-74.1	20.1	0.994
R 329	-73.8	12.6	1.000
R 337	+74.6	24.4	1.013
R 339	+73.0	24.1	1.028
R 340	+72.2	22.8	1.035

Table 15. List of data runs which are utilized for the determination of the elastic pion-proton asymmetry. The factor of $\frac{1}{2}$ indicates data tapes which were only partially analyzed (simply a matter of convenience), $\mathcal{P}$ is the target polarization, $M_0 = R_0\,\Delta t$ is the number of beam particles on target and ϵ is the analysis efficiency normalized to the average $\bar{\epsilon} = 0.515$ (see appendix A).

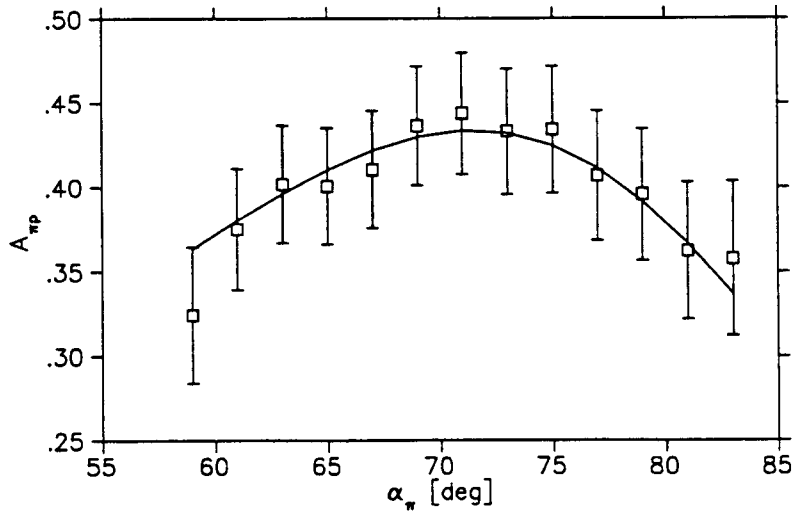

Figure 51. Results for the elastic pion-proton scattering asymmetry. The solid line represents the theoretical prediction.

α_π	$\mathcal{A}_{exp} \pm \delta\mathcal{A}$	$\mathcal{A}_{theor}$	$\left(\frac{d\sigma}{d\Omega}\right)_{theor} \left[\frac{mb}{sr}\right]$
59°	0.324 ± 0.04	0.363	6.26
61°	0.375 ± 0.04	0.380	5.63
63°	0.402 ± 0.04	0.396	5.08
65°	0.401 ± 0.04	0.410	4.59
67°	0.411 ± 0.04	0.422	4.16
69°	0.436 ± 0.04	0.430	3.80
71°	0.444 ± 0.04	0.434	3.49
73°	0.433 ± 0.04	0.432	3.23
75°	0.434 ± 0.04	0.425	3.01
77°	0.407 ± 0.04	0.411	2.84
79°	0.396 ± 0.04	0.392	2.71
81°	0.362 ± 0.04	0.367	2.61
83°	0.358 ± 0.05	0.337	2.54

Table 16. Results for the elastic pion-proton scattering asymmetry.

Chapter 21

Bremsstrahlung

The analysis of the bremsstrahlung data starts off with a review of the performances of the various detector systems with respect to the analysis strategy outlined in chapter 13.

1. The event $\pi \cdot p \cdot X$ has been defined, where X is a charged or neutral event in the photon detectors. A πp"γ" candidate is defined as a πpX event with no energy deposited in the photon veto counter. However, due to a large beam-related count rate in the photon detectors, a large fraction of the πp"γ" events is expected to be random background.

2. The pion momentum and the proton angle define elastic $\pi^+ p$ scattering events. Those events are removed with the analysis cut DG4 (see the last chapter) and the remaining πp"γ" candidates must be identified as inelastic $\pi^+ p$ scattering events.

3. The bremsstrahlung analysis depends on the knowledge of all kinematic variables. We have calibration problems with

   - the proton energy. Even though the calibration procedure is well-defined, a systematic uncertainty of up to 10 % is possible which, furthermore, may be a function of time.

   - the photon energy. Extreme operating conditions for the detector cast doubt on the energy measurement. The overall gain is known with a

systematic uncertainty of up to 10 %. However, variations in the gain due to fluctuations in the count rate might be much larger.

With these uncertainties in the energy measurements, it becomes crucial to approach the analysis from several different directions in order to ensure that $\pi p\gamma$ events have been identified properly.

The analysis which follows is based on the data runs which have been listed in table 17. We only look at MINA events, since this detector sees less random background than TINA. The expected number of signal events in MINA is given by

$$S_0 = 0.02 \frac{\text{events}}{\text{MHz h nb}} \cdot 265 \text{ MHz h} \cdot \int_{30\,MeV}^{130\,MeV} \sigma \, dk \approx 100.$$

Of those events, approximately 30 have a photon energy above 80 MeV.

The kinematic variables, which have been defined in the last chapter for elastic scattering, have their analogs for the bremsstrahlung reaction :

$$\begin{aligned} T_{miss}^{\pi p\gamma} &= T_0 - T_\pi - T_p - k \\ \text{MTGT}_{\pi p\gamma} &= \sqrt{(T_0 - T_{pi} - T_p - k)^2 - \left(\vec{p}_0 - \vec{p}_\pi - \vec{p}_p - \vec{k}\right)^2} - m_p \\ \text{PL, PT} &= \text{longitudinal and transverse momentum balance with respect to the direction of the photon} \end{aligned}$$

The corresponding distributions of events are shown in figure 52. The full-width-half-maximum values for these distributions are compared to the ones for elastic scattering in table 18. The results suggest that the random background is dominated by quasi-free $\pi^+ p$ scattering.

An indication of whether there are signal events in the data sample is given by a comparison of the photon energy spectra for in-time and out-of-time events (recall chapter 7). The two contributions are shown in figure 53. An excess of events in the in-time spectrum is clearly visible.

In an attempt to identify these candidates as bremsstrahlung events, the same spectrum has been plotted for three different cuts on the variable $\text{MTGT}_{\pi p\gamma}$ (see figure 54). The results are inconclusive in that it is not obvious which cut singles out bremsstrahlung events as opposed to random background.

Run number	$\mathcal{P}$ [%]	M_0 [MHz h]	ϵ
R 320	-77.5	21.1	1.017
R 321	-77.0	20.9	1.013
R 322	-76.5	20.1	0.987
R 323	-76.1	19.6	0.986
R 324	-75.7	20.1	0.999
R 325	-75.3	19.7	0.990
R 326	-74.9	19.8	0.989
R 327	-74.5	19.7	0.987
R 328	-74.1	20.1	0.994
R 329	-73.8	12.6	1.000
R 337	+74.6	24.4	1.013
R 339	+73.0	24.1	1.028
R 340	+72.2	22.8	1.035
Sum/Average		265.0	1.003

Table 17. List of data runs which are utilized for the analysis of the bremsstrahlung data. This list represents about 35 % of the data on the frozen spin target which can be analyzed with the present set of detector calibrations and about 20 % of all the bremsstrahlung data.

Variables	[*Units*]	$\pi p_{elastic}$	$\pi p_{inelastic}$	*Bremsstrahlung*
FWHM($T_{\pi p}$)	[MeV]	18		
FWHM(PL)	[MeV/c]	41	213	232
FWHM(PT)	[MeV/c]	36	159	130
FWHM(MTGT)	[MeV]	20		122

Table 18. A comparison between the full-width-half-maximum values for the kinematic variables $T_{\pi p}$, PL, PT, and MTGT for elastic and inelastic scattering data.

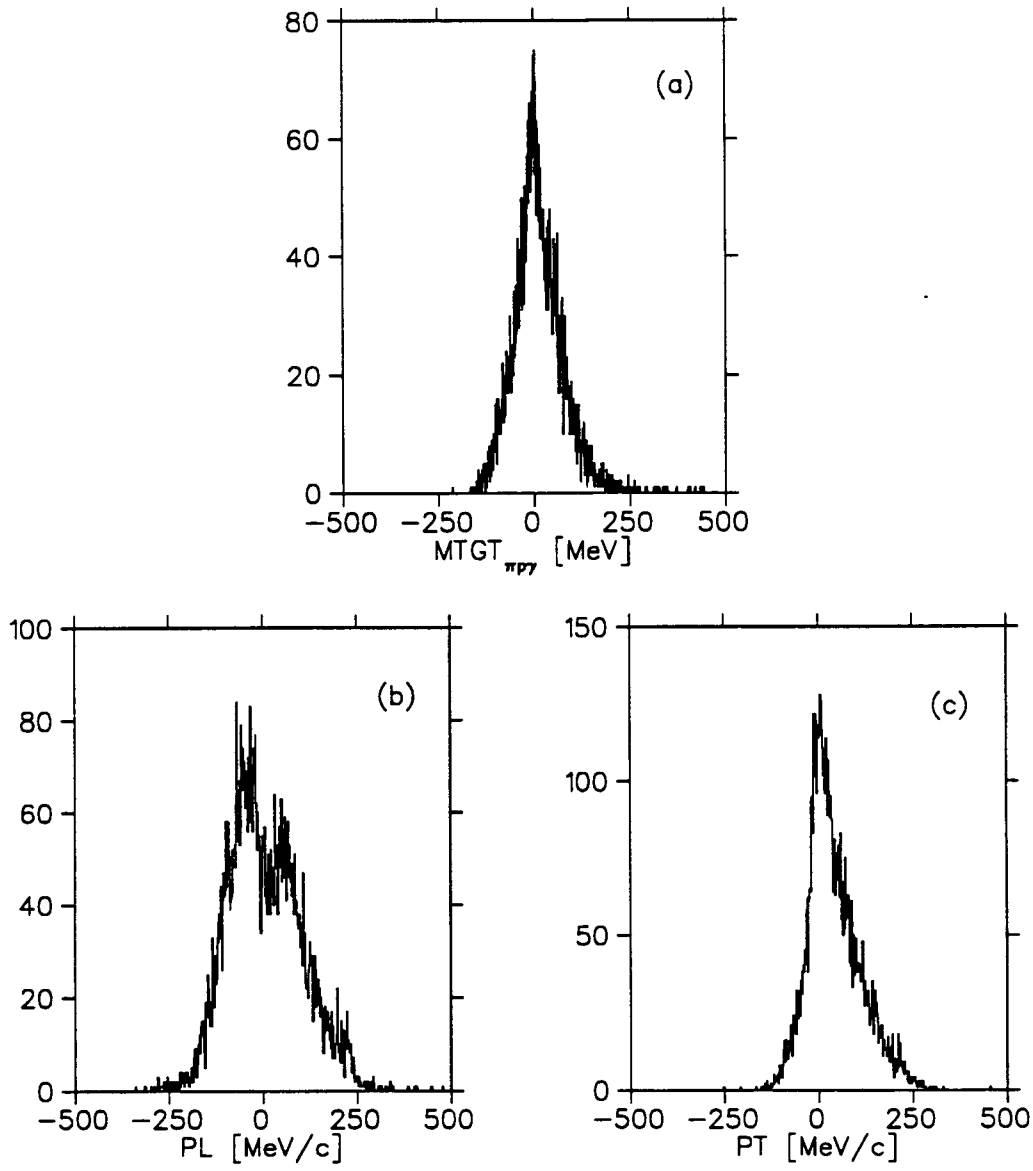

Figure 52. Distributions of events for variables, which are of interest to the bremsstrahlung analysis, based on bremsstrahlung data. (a) MTGT$_{\pi p\gamma}$, (b) PL, (c) PT.

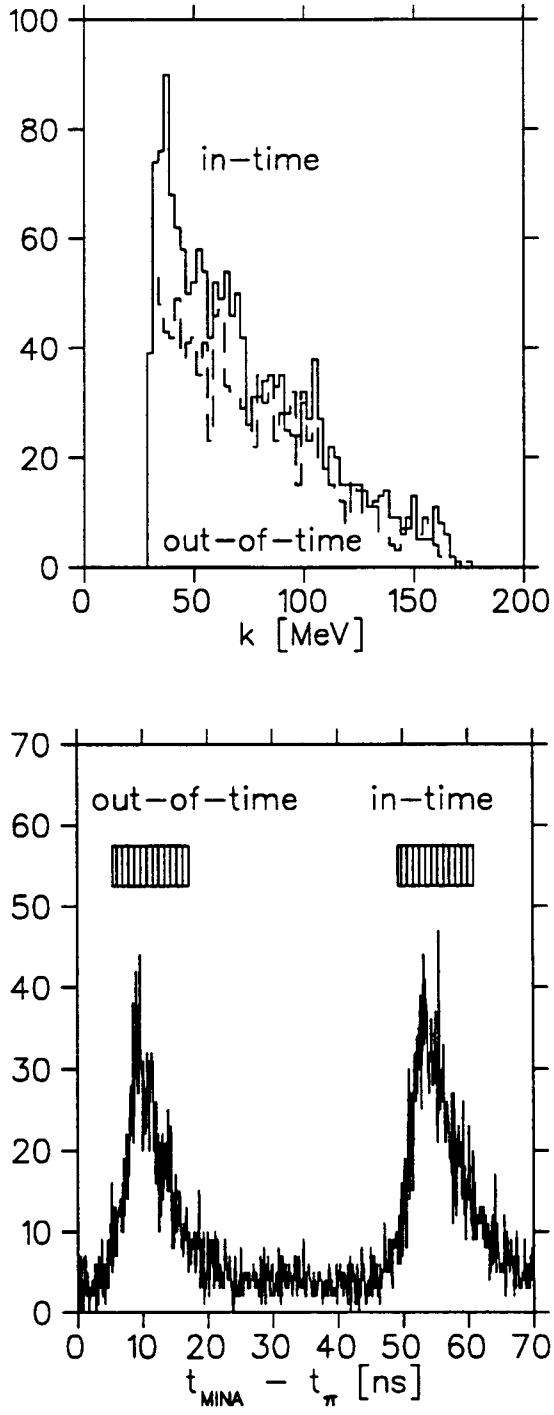

Figure 53. The distribution of bremsstrahlung candidates in the photon energy. Data are taken from the detector MINA. (a) The solid line is the in-time spectrum, the dashed line is the out-of-time spectrum. The corresponding time windows are defined in figure (b).

Data samp	$(S+N)$	N	S	$\frac{S}{N}$
before the PL cut	1701	1296	411	0.32
after the PL cut	891	581	310	0.53

Table 19. The signal-to-noise ratio $\frac{S}{N}$ before and after the PL cut.

The longitudinal momentum balance along the direction of the photon gives us some handle on the background. The balance PL must be positive for any real signal event. This behaviour is demonstrated for pion absorption on a nucleus $\pi\mathcal{N} \rightarrow ppp\mathcal{N}'$, where one proton enters the photon detector. The distribution of these events in the variable PL is shown in figure 55. There are no events with PL < 0, which implies that a corresponding cut can be safely applied to the bremsstrahlung candidates. The evidence that this cut does indeed suppress the background is shown in table 19, where we show the in-time and out-of-time counts before and after this PL-cut. The signal-to-noise ratio $\frac{S}{N}$ does improve by a factor of 2. However, what does not improve is the qualitative behaviour of the variable MTGT and the effectiveness (or lack thereof) of cutting on it. The analogous results to figure 54 are shown in figure 56.

Our inability to identify the signal suggests that MTGT is kinematically not well defined, i.e. there could be a systematic bias originating from the uncertainties in the photon energy calibration, which spreads out the signal into a wide peak and makes it indistinguishable from the background distribution. The alternative is to look for variables which *do not* depend on the photon energy. Such a variable is given by

$$\text{BPS} = \sqrt{(T_0 - T_\pi - T_p)^2 - (\vec{p}_0 - \vec{p}_\pi - \vec{p}_p)^2} = m_\gamma^2. \qquad (21.1)$$

The distribution of events in BPS is shown in figure 57. There is *no* evidence for an excess of events around BPS $= 0$, which would indicate the presence of bremsstrahlung events.

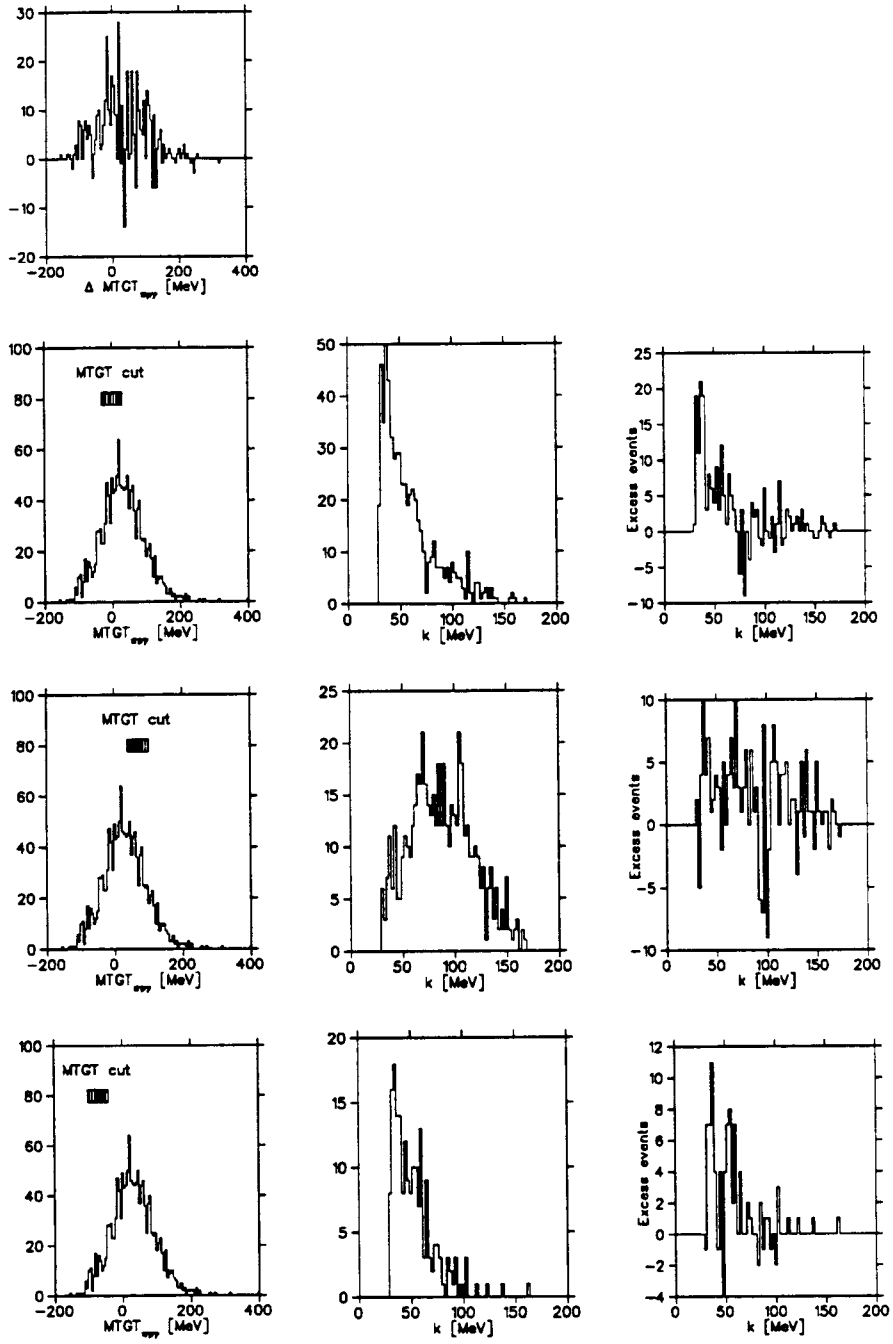

Figure 54. The in-time and out-of-time photon energy spectra are subjected to cuts on the variable MTGT. The top graph shows the excess of events in the variable MTGT for the detector MINA. The bottom graphs show the response of the in-time and out-of-time energy spectra to various cuts on that variable. Column one : the distribution in the variable MTGT before cuts, column two : the in-time photon energy spectrum after a cut on MTGT, column three : excess events in the energy spectrum (in-time - out-of-time)

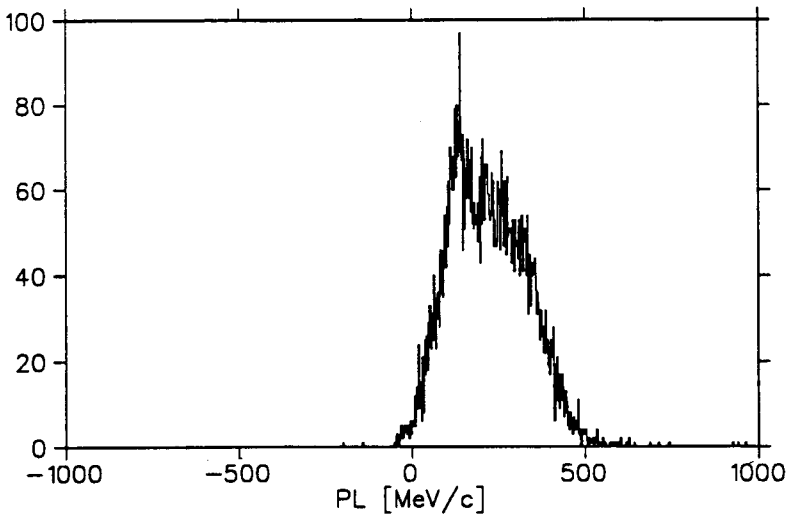

Figure 55. Distribution of events in the variable PL for pion absorption events with one proton entering the photon detector.

Let us summarize :

- There is evidence for an excess of events in the in-time photon energy spectrum. We have studied many kinematically similar variables such as the longitudinal momentum balance along the axis of the photon (PL) and the missing energy ($T^{\pi p}_{miss}$) and have found the same excess of events in the in-time spectra.
- Any further attempt to suppress the background based on kinematic variables such as MTGT and BPS has been unsuccessful.

The same results have been obtained from a full χ^2-analysis of the events with and without the photon energy as a free variable. The least-squares fit has not lead to a unique identification of the bremsstrahlung candidates. Distributions of the χ^2-variable for events for the in-time window and what is left over, after the out-of-time events have been subtracted, are shown in figure 58.

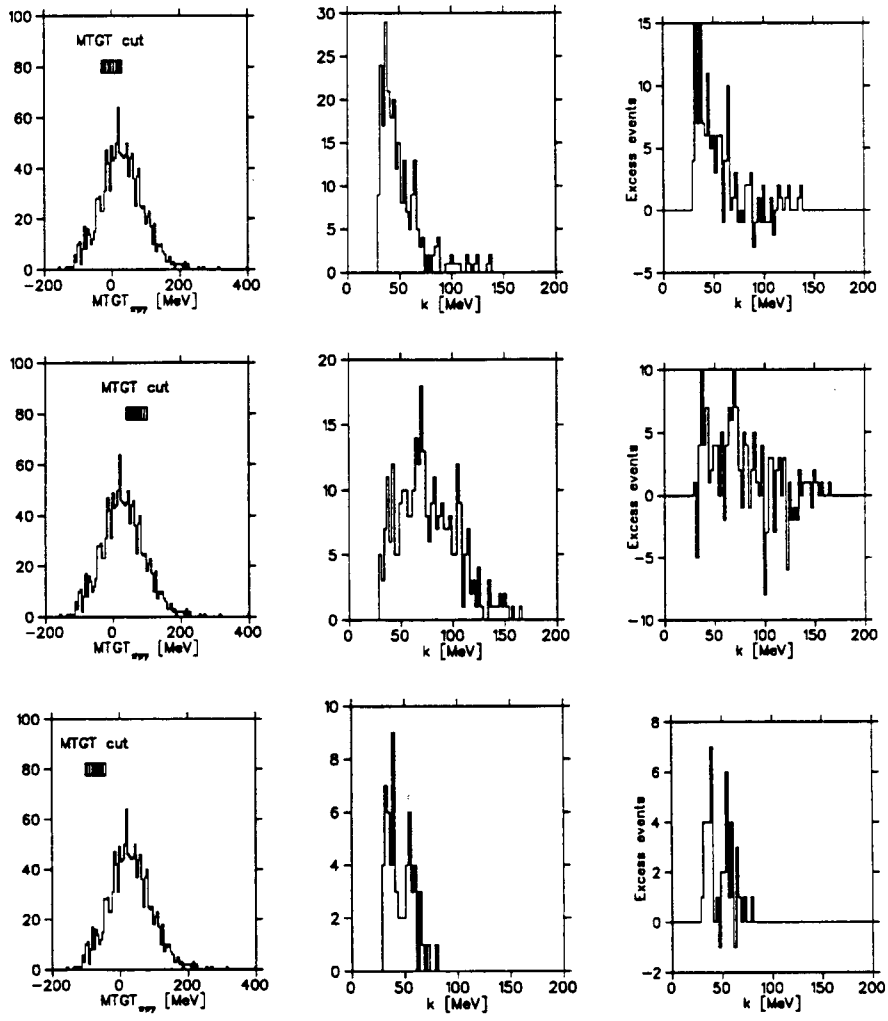

Figure 56. The in-time and out-of-time photon energy spectra are subjected to cuts on the variable MTGT and PL. Column one : the distribution in the variable MTGT before cuts, column two : the in-time photon energy spectrum after cuts on MTGT and PL, column three : excess events in the energy spectrum (in-time - out-of-time)

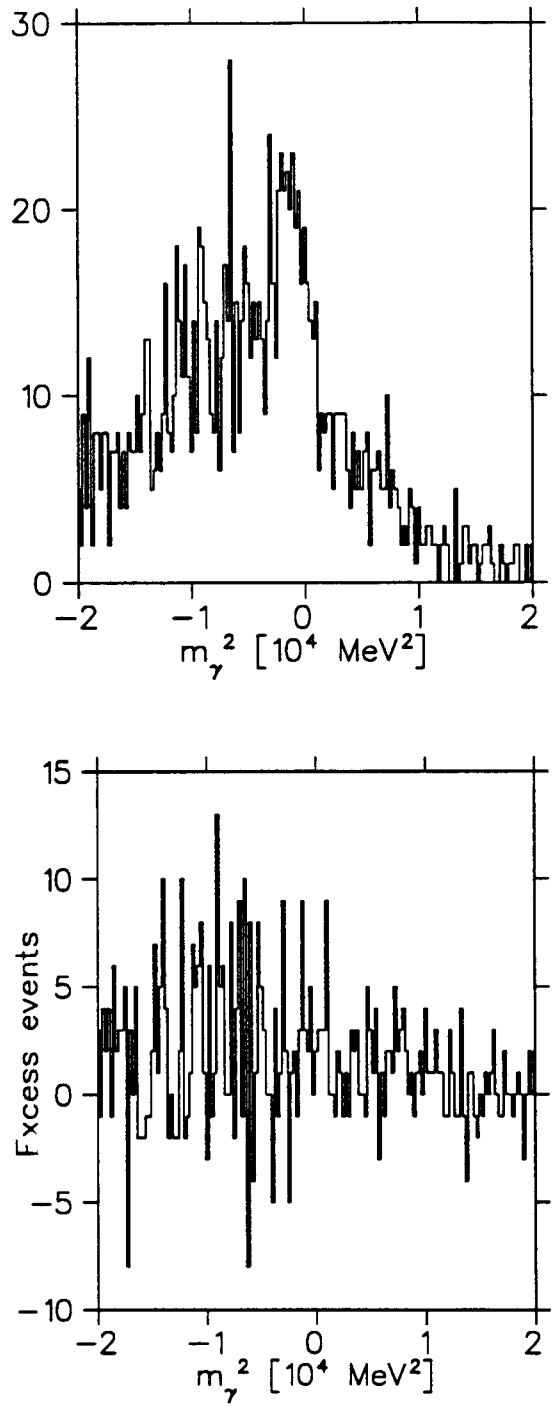

Figure 57. The tribution of events in the variable BPS. The top graph shows events in the in-time bin after a cut on PL, the bottom graph shows excess events after a subtraction of the random background (out-of-time events).

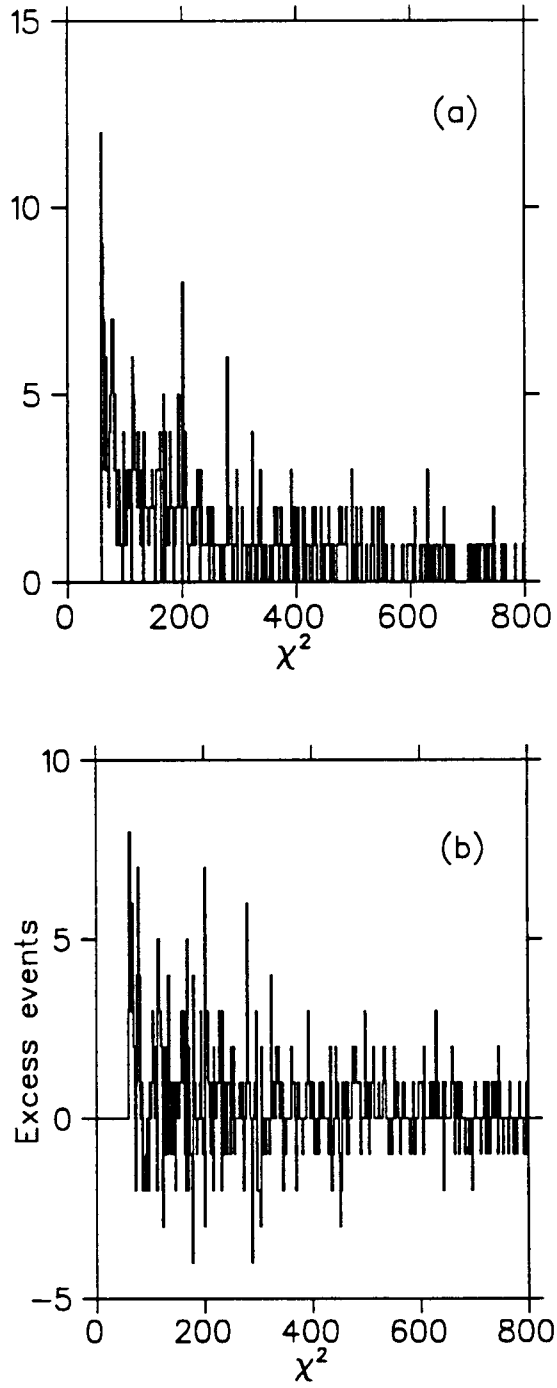

Figure 58. The distribution of the χ^2-variable. (a) shows the spectrum of in-time events, (b) shows the excess of events.

Chapter 22

Summary

The analysis of the bremsstrahlung data has failed to lead to a unique identification of bremsstrahlung events. It is therefore impossible to extract values for the asymmetry.

The principal causes for the difficulties in the analysis are

- the extreme conditions under which the photon detectors were operated. It not only lead to a change in the overall gain of the device relative to the prerun calibration, but possibly also to large short term gain fluctuations which can not be estimated.

- the lack of a reliable energy calibration for the proton detector. In principle, the measurement of the pion and proton energies and angles is sufficient to identify bremsstrahlung events. In practice, this has become impossible due to the poor energy resolution of the detector and the non-negligible systematic uncertainty in the calibration.

The design of this experiment was *not* based on a fault-tolerant analysis strategy, i.e. the importance of the proton and photon energy measurements in the face of finite detector resolutions and possible failures was not recognized until after the experiment was completed. The technical difficulties mentioned above were thus not anticipated. If they would have been anticipated, one would either have avoided them through changes in the design of the detectors, or looked for

and provided other means of analyzing the bremsstrahlung data. Furthermore, the background turned out to be dominated by accidental coincidences with random photons. We have shown that cuts on the available kinematic variables do not effectively suppress this background unless the resolution in the missing energy is reduced by a factor of two (see section 15.3). Again, if this had been recognized, before the experiment was run, one could have tried to apply additional shielding to the photon detectors and reduce the random background in this manner.

A future experiment must evolve around a fault-tolerant analysis strategy which includes proper calibration procedures and monitoring techniques for all the experimental observables, which can be identified as critical measurements.

Bibliography

[1] F. E. Low, Phys. Rev. **110**, 974 (1958)

[2] H. Feshbach, D. R. Yennie, Nucl. Phys. **37**, 150 (1962)

[3] S. L. Adler and Y. Dothan, Phys. Rev. **151**, 1267 (1966)

[4] T. H. Burnett and N. M. Kroll, Phys. Rev. Lett. **20**, 86 (1968)

[5] Saul Barshay and Tsu Yao, Phys. Rev. **171**, 1708 (1968)

[6] A. Kondratyuk and L. A. Ponomarev, Yad. Fiz. **7**, 111 (1982) [Sov. J. Nucl. Phys. **7**, 82 (1968)]

[7] R. D. Peccei, Phys. Rev. **176**, 1812 (1968)

[8] Charles Picciotto, Phys. Rev. **185**, 1761 (1969)

[9] T. H. Burnett, Phys. Rev. **D1**, 3098 (1970)

[10] R. Baier, L. Pittner, P. Urban, Nucl. Phys. **B27**, 589 (1971)

[11] W. E. Fischer and P. Minkowski, Nucl. Phys. **B36**, 519 (1971)

[12] L. M. Nath, B. Etemadi, J. D. Kimel, Phys. Rev. **D3**, 2153 (1971)

[13] Harold W. Fearing, Phys. Rev. **C6**, 1136 (1972)

[14] Harold W. Fearing, Phys. Rev. **D7**, 243 (1973)

[15] Ebbe M. Nyman, Phys. Rep. **9**, 179 (1974)

[16] R. P. Haddock and K. C. Leung, Phys. Rev. **D9**, 2151 (1974)

[17] D. I. Sober *et al*, Phys. Rev. **D11**, 1017 (1975)

[18] Charles Picciotto, Il Nuovo Cimento **29A**, 41 (1975)

[19] Charles Picciotto, Nucl. Phys. **B89**, 357 (1975)

[20] Douglas S. Beder, Nucl. Phys. **B84**, 362 (1975)

[21] B. M. K. Nefkens and D. I. Sober, Phys. Rev. **D14**, 2434 (1976)

[22] M. K. Liou and W. T. Nutt, Phys. Rev. **D16**, 2176 (1977)

[23] Q. Ho-Kim and J. P. Lavine, Nucl. Phys. **A285**, 407 (1977)

[24] G. Grammer, Jr., Phys. Rev. **D15**, 917 (1977)

[25] M. K. Liou and W. T. Nutt, Il Nuovo Cimento **46A**, 365 (1978)

[26] M. K. Liou, Phys. Rev. **D18**, 3390 (1978)

[27] P. Pascual, R. Tarrach, Nucl. Phys. **B134**, 133 (1978)

[28] Harold W. Fearing, TRIUMF Preprint TRI-PP-78-28, Dec. 1978

[29] B. M. K. Nefkens *et al*, Phys. Rev. **D18**, 3911 (1978)

[30] Charles Picciotto, Phys. Rev. **D19**, 3244 (1979)

[31] A. Cass and B. H. J. McKellar, Nucl. Phys. **B166**, 399 (1980)

[32] D. E. A. Smith, P. F. Glodis, R. P. Haddock, K. C. Leung, M. A. Tamor, Phys. Rev. **D21**, 1715 (1980)

[33] G. Landi and F. Matera, Il Nuovo Cimento **64A**, 332 (1981)

[34] Charles Picciotto, Can. J. Phys. **59**, 336 (1981)

[35] E. J. Moniz, Nucl. Phys. **A374**, 557c (1982)

[36] H. W. Fearing, G. R. Goldstein, M. J. Moravcsik, TRIUMF Preprint TRI-PP-83-44, May 1983

[37] Harold W. Fearing, Invited paper at the Workshop on Nuclear Physics with stored cooled beams, Bloomington, Oct. 15-17, TRIUMF preprint TRI-PP-84-100, Oct. 1984

[38] Charles Picciotto, Phys. Rev. **C31**, 1036 (1985)

[39] M. J. Moravcsik and G. R. Goldstein, Phys. Rev. **C34**, 1411 (1986)

[40] M. K. Liou and Z. M. Ding, Phys. Rev. **C35**, 651 (1987)

[41] L. Heller, S. Kumano, J. C. Martinez, E. J. Moniz, Phys. Rev. **C35**, 718 (1987)

[42] R. Wittman, Phys. Rev. **C37**, 2075 (1988)

[43] C. A. Meyer *et al*, Phys. Rev. **D38**, 754 (1988)

[44] A. Bosshard *et al*, Phys. Rev. Lett. **64**, 2619 (1990)

[45] A. Bosshard *et al*, Phys. Rev. **D44**, 1962 (1991)

[46] J. D. Jackson, *Classical Electrodynamics*, 2nd ed. (Wiley, New York, 1975), Chap. 15, p. 701ff.

[47] Nucl. Instrum. Methods **A264**, 186 (1988)

[48] J. A. Faucett *et al*, Phys. Rev. **C30**, 1622 (1984), J. S. Findley *et al*, Nucl. Phys. **A292**, 53 (1977), J. Mougey *et al*, Nucl. Phys. **A262**, 461 (1976)

[49] R. L. Craun and D. L. Smith, Nucl. Instrum. Methods **80**, 239 (1970)

[50] R. W. Engstrom, *Photomultiplier Handbook*, RCA Corporation 1980, PMT-62

[51] Particle Properties Data Booklet, page 113, from "Review of Particle Properties", Reviews of Modern Physics **56**, No 2, Part II, April 1984

[52] L. Lyons, *Statistics for nuclear and particle physicists*, Cambridge University Press 1986

[53] R. K. Bock, H. Grote, D. Notz, M. Regler, *Data analysis techniques for high-energy physics experiments*, Cambridge University Press 1990

[54] R. A. Arndt, Scattering Analysis Interactive Dial-in (SAID) program (SM90) (unpublished)

Appendices

Appendix A

List of Analysis Cuts and Efficiencies

We list in this chapter all the analysis cuts which are applied to the data in order to define a $\pi p\gamma$ candidate event. We have refrained from listing the precise definitions of the variables to which these cuts apply. Instead, we give a general description of the action of each cut.

- **CTOF** : $\epsilon = 0.986 \pm 0.004$

  The time-of-flight counters on the pion spectrometer return both time and $\frac{dE}{dx}$ information. CTOF measures the correlation between the $\frac{dE}{dx}$ measurement and $\Delta t = (t_{out} - t_{in})$ and is utilized to reject hits in the drift chambers which are uncorrelated to the particle track.

- **MTOF** : $\epsilon = 0.997 \pm 0.004$

  Time-of-flight information is a necessary input to the pion spectrometer data analysis. MTOF guarantees that this information is indeed available.

- **ERR** : $\epsilon = 0.962 \pm 0.003$

  ERR guarantees that the drift chamber data stored on tape are valid. Some events have no chamber data due to accidental hits in the TOF counters or incomplete data due to a software imposed upper bound on how much data per event are transfered to tape.

- **XHIT** : $\epsilon = 0.724 \pm 0.008$

  Noise and multiple hits in the chambers as well as hardware problems such as

bad wires and dead time can make it impossible to define a complete track with valid measurements in all chambers. This efficiency is *not* related to the probability of finding a hit in a chamber plane given that there was a charged particle track.

- **PBND** : $\epsilon = 0.997 \pm 0.004$

  PBND identifies the particle in the spectrometer as a pion. The corresponding efficiency was measured with elastic $\pi^+ p$ scattering data off a liquid hydrogen target.

- **YTGT** : $\epsilon = 0.983 \pm 0.005$

  This cut limits the interaction vertex to the extent of the target in the coordinate normal to the scattering plane ($\hat{z}$ in the lab system).

- **MREJ** : $\epsilon = 0.978 \pm 0.001$

  MREJ amounts to a cut on very large angle scattering and π-decay in the spectrometer. See appendix D.1 for a more detailed discussion on the variable x = MREJ of equation D.8.

- **PLPU** : $\epsilon = 0.962 \pm 0.003$

  PLPU removes events with evidence of excessive pile-up in the proton $\frac{dE}{dx}$ measurement.

- **XNV** : $\epsilon > 0.997$

  Good neutral NaI events are vetoed by accidental coincidences with a hit in the charged particle veto counters. The low veto count rate makes this a negligible effect.

- **C2PU** : $\epsilon = 0.979 \pm 0.008$

  This is a cut which removes events with invalid proton $\frac{dE}{dx}$ and pile-up signatures. They can be traced back to event triggers which were corrupted by accidental events in the $\frac{dE}{dx}$ counter. The same signature is caused by events which are dominated by a very late NaI event in coincidence with an earlier

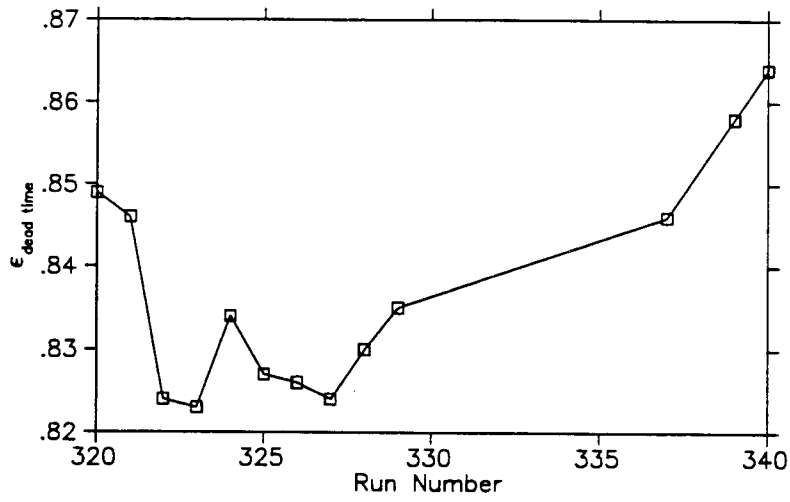

Figure 59. Efficiency due to dead time in the data acquisition system as function of the run number.

π^+p event. Those events can of course be eliminated by a cut on NaI (i.e. photon) timing information.

- **DEAD** : $\epsilon = f(R_\pi)$, $\bar{\epsilon} = 0.835$

  DEAD measures the dead time in the data acquisition system and is defined by the ratio of "$\pi p\gamma$" triggers stored on tape over the number of these triggers presented as a request for attention to the computer. This efficiency depends on the trigger rate and the amount of CPU time needed to process and store one full event. Figure 59 shows ϵ_{DEAD} as a function of run number.

The cuts listed so far combine for a total efficiency of

$$\boxed{\epsilon = 0.515 \pm 0.015}$$

There are other cuts whose efficiencies have not been defined due to uncertainties in the proton and photon energy calibrations.

- **PPID**

  The variable PPID is defined in equation 18.4 on page 101 and used for particle identification as well as a tool to define the proton energy calibration.

- **DG4**

  DG4 has become a standard cut to separate elastic π^+p scattering events from inelastic events based on a comparison of the measured pion momentum and proton angle to elastic scattering kinematics (see chapter 20).

- **PL**

  PL is a cut on the longitudinal π^+p momentum balance along the direction of the photon.

Appendix B

The Analysis Model

The purpose of this chapter is to relate theoretical quantities, such as cross sections and asymmetries, to quantities which are derived from experimental data. We are interested in how the design of the experiment and the analysis of the acquired data affects this relationship and in how we can use this knowledge as a tool to design a better experiment.

Let's define a physics event as a vector $\mathbf{e}$ of measurables (angles, momenta, energies, positions, etc.) in an N-dimensional space $\mathcal{R}^N$. The detector responds to this event by returning a measurement $\mathbf{m}$. The vector $\mathbf{m}$ will not be identical to $\mathbf{e}$ due to measurement errors. We can define a conditional probability $P(\mathbf{m}|\mathbf{e})$ which tells us how likely it is to find a measurement $\mathbf{m}$ given the event $\mathbf{e}$. $P(\mathbf{m}|\mathbf{e})$ is called the "detector response function".

Not every measurement $\mathbf{m}$ will be accepted by the data acquisition electronics. Only signatures consistent with a certain condition T, called the "trigger", will be passed on to tape and stored for posterity. How T should be chosen is one of the questions we like to answer. For that purpose, we will define a function $P(\mathbf{m}|\mathrm{T})$ which is the conditional probability that $\mathbf{m}$ satisfies T. If $\mathbf{m}$ does indeed satisfy T, $P(\mathbf{m}|\mathrm{T})$ will be set equal to 1.

We also introduce

$\rho(\mathbf{e})$ = the probability that an event $\mathbf{e}$ occurs

$\Delta\mathbf{m}$ = an N-dimensional volume element in the space $\mathcal{R}^N$

To this end, we can define the expected signal and background as

$$\begin{aligned} S(\Delta\mathrm{m}) &= \int_{\Delta\mathbf{m}} d\mathbf{m} \int d\mathbf{e}\, P(\mathbf{m}|\mathrm{T})\, P(\mathbf{m}|\mathbf{e})\, \rho_S(\mathbf{e}) \\ B(\Delta\mathrm{m}) &= \int_{\Delta\mathbf{m}} d\mathbf{m} \int d\mathbf{e}\, P(\mathbf{m}|\mathrm{T})\, P(\mathbf{m}|\mathbf{e})\, \rho_B(\mathbf{e}) \end{aligned} \tag{B.1}$$

No effort has yet been made to decide whether a given measurement $\mathbf{m}$ is consistent with the hypothesis that it was caused by a particular event $\mathbf{e}_S$. More importantly, one wants to know which event $\mathbf{e}_S$ of a class of events $\mathcal{Z}$ is *most* consistent with $\mathbf{m}$ and how likely it is that the measurement $\mathbf{m}$ was indeed caused by that event $\mathbf{e}_S$.

The tools for this analysis are the Maximum-Likelyhood (ML) and the Least-Squares (LS or χ^2) methods. Let $\mathcal{Z}$ be a class of events $\mathbf{e}_S$ which are parameterized by an n-dimensional vector $\mathbf{p}$, i.e.

$$\mathcal{Z} = \left\{ \mathbf{e}_S | \mathbf{e}_S \in \mathcal{R}^N,\ \mathbf{e}_S = f(\mathbf{p})\ \forall\, \mathbf{p} \in \mathcal{R}^n \right\}$$

$f : \mathbf{p} \rightarrow \mathbf{e}_S$ maps the parameter space $\mathcal{R}^n$ into the event space $\mathcal{R}^N$. It follows that $\mathcal{Z}$ is a subspace (or more precisely a submanifold) of $\mathcal{R}^N$.

Example :

Elastic $\pi^+ p$ scattering is characterized by two free parameters, the initial pion kinetic energy T_0 and the pion scattering angle Θ_π, i.e.

$$\mathbf{p} = \{T_0, \Theta_\pi\}\ ,\ \mathrm{n} = 2$$

The space of measurables might be spanned by

T_π = the kinetic energy of the scattered pion
Θ_π = the pion scattering angle
T_p = the kinetic energy of the scattered proton
Θ_p = the proton scattering angle

or in other words

$$\begin{aligned} \mathbf{m} &= \{T_\pi, \Theta_\pi, T_p, \Theta_p\} \in \mathcal{R}^4,\ \mathrm{N} = 4 \\ \mathbf{m} &= f(\mathbf{p}) = f(\{T_0, \Theta_\pi\} \in \mathcal{R}^2) \end{aligned}$$

The task is to find a vector $\mathbf{p}_S$ such that $\mathbf{e}_S = f(\mathbf{p}_S)$. This is a classic optimization problem. Making use of our earlier definition of $P(\mathbf{m}|\mathbf{e})$, we can formulate the ML and LS methods as follows :

- **ML** : The Maximum Likelyhood method searches for an event $\mathbf{e}_S = f(\mathbf{p}_S)$ such that $P(\mathbf{e}_S|\mathbf{m})$ becomes a maximum. $P(\mathbf{e}_S|\mathbf{m})$, the conditional probability of having an event $\mathbf{e}_S$ which has caused the measurement $\mathbf{m}$, can be related to $P(\mathbf{m}|\mathbf{e}_S)$ through Bayes theorem :

  $$P(\mathbf{e}_S|\mathbf{m}) = P(\mathbf{m}|\mathbf{e}_S)\,\frac{P(\mathbf{e}_S)}{P(\mathbf{m})}$$

  where $P(\mathbf{e}_S)$ and $P(\mathbf{m})$ are the probabilities for the occurrences of $\mathbf{e}_S$ and $\mathbf{m}$, respectively.

  Notice that $\mathbf{m}$ is given in this case, which makes $P(\mathbf{m})$ a constant for this optimization problem. Unless $P(\mathbf{e}_S)$ varies strongly over a range of the order of one sigma (which is the detector resolution), $P(\mathbf{e}_S)$ can be considered constant and $P(\mathbf{m}|\mathbf{e}_S) \approx P(\mathbf{e}_S|\mathbf{m})$.

  The vector $\mathbf{p}_S$ and the event $\mathbf{e}_S = f(\mathbf{p}_S)$ are thus defined by the equation

  $$P(\mathbf{e}_S|\mathbf{m}) = P(\mathbf{m}|\mathbf{e}_S) = P(\mathbf{m}|f(\mathbf{p}_S)) = \max_{\mathbf{p}\in\mathcal{R}^n} P(\mathbf{m}|f(\mathbf{p})) \qquad \text{(B.2)}$$

- **LS** : The Least Squares method looks for an event $\mathbf{e}_S$ such that

  $$d^2(\mathbf{m}|\mathbf{e}_S) = d^2(\mathbf{m}|f(\mathbf{p}_S)) = \quad _{in} = \min_{\mathbf{p}\in\mathcal{R}^n} d^2(\mathbf{m}|f(\mathbf{p})) \qquad \text{(B.3)}$$

For the special case where $P(\mathbf{m}|\mathbf{e})$ is a product of Gaussian distribution functions, which is very often a good approximation, the two methods give identical

results and are related by

$$\chi^2_{min} = d^2(\mathbf{m}|\mathbf{e}_S) = -2\,[\,\ln P(\mathbf{m}|\mathbf{e}_S) - \ln P(\mathbf{e}_S|\mathbf{e}_S)]$$

We define the following classification algorithm :

> *The hypothesis that the measurement* $\mathbf{m}$ *was caused by the event* $\mathbf{e}_S \in \mathcal{Z}$ *is accepted if and only if*
>
> $$\chi^2_{min} = d^2(\mathbf{m}|\mathbf{e}_S) \leq \chi^2_0$$
>
> *where* χ_0 *is a constant.*

The choice of χ_0 depends on an analysis of the distribution of signal and background events.

In order to simplify further developments, we work with the following assumption :

> *The detector response function* **is** *a product of N Gaussian distribution functions with standard deviations* $\{\sigma_i | \, i = 1 \ldots N\}$. *Furthermore, the measurements* m_i *are statistically independent.*

With this simplification we can define dimensionless vectors

$$\begin{aligned} z_i &= \frac{e_i}{\sigma_i} \quad , \quad i = 1 \ldots N \\ x_i &= \frac{m_i}{\sigma_i} \quad , \quad i = 1 \ldots N \end{aligned}$$

and

$$\begin{aligned} P(\mathbf{x}|\mathbf{z}) &= \left(\frac{1}{\sqrt{2\pi}}\right)^N e^{-\frac{1}{2}d^2(\mathbf{x}|\mathbf{z})} \\ d^2(\mathbf{x}|\mathbf{z}) &= \sum_i (x_i - z_i)^2 \end{aligned}$$

It is easy to show that

$$\begin{aligned} P(\mathbf{m}|\mathbf{e}) &= \left(\prod_{i=1}^{N} \frac{1}{\sigma_i}\right) P(\mathbf{x}|\mathbf{z}) \\ d^2(\mathbf{m}|\mathbf{e}) &= d^2(\mathbf{x}|\mathbf{z}) \end{aligned}$$

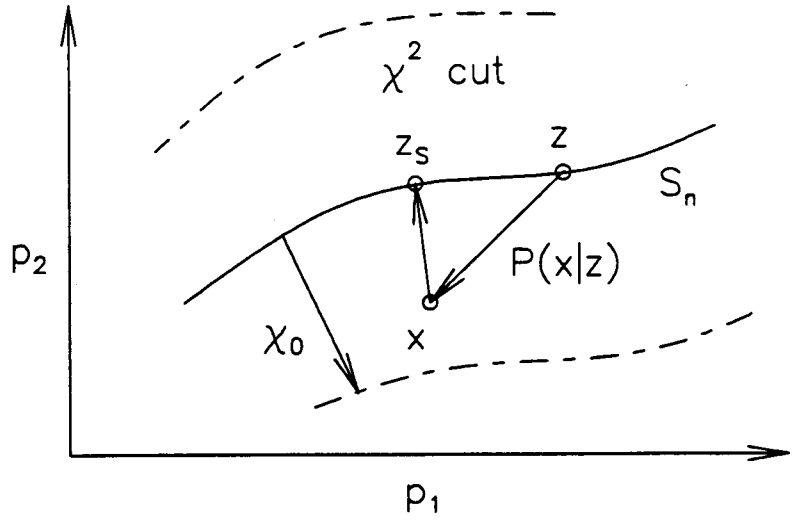

Figure 60. The action of a Maximum Likelyhood analysis on the space of events e and measurements **m**.

and we will work from now on exclusively in the space of **x** and **z**. It is worth noting that the variables $(x_i - z_i)$ are random Gaussian variables with mean zero and standard deviation one.

The action of a χ^2 or maximum likelyhood analysis is graphically represented in figure 60. An event **z** leads to a measurement **x** with probability $P(\mathbf{x}|\mathbf{z})$. The χ^2-analysis associates an event $\mathbf{z}_S$ to **x** such that $P(\mathbf{x}|\mathbf{z}_S)$ is a maximum. In the space of vectors **x** and **z**, this association corresponds to a projection of the point **x** onto the subspace $\mathcal{Z} = \{\mathbf{z}(\mathbf{p})\}$. If the distance $d^2(\mathbf{x}|\mathbf{z}_S)$ is less or equal to χ_0, we accept the hypothesis that **x** was caused by the event $\mathbf{z}_S$.

The space of all points **x** which can be associated to the point $\mathbf{z}_S$ in this manner forms a disc of dimension (N-n) and radius χ_0. We will denote it by $\mathcal{D}^{\chi_0}_{N-n}(\mathbf{z}_S)$.

The number of events $X(\mathbf{z}_S)$ with an experimental signature compatible with $\mathbf{z}_S$ will then be equal to

$$X(\mathbf{z}_S) = \int_{\mathcal{S}^m} d\mathcal{S}^m \int_{\mathcal{D}^{\chi_0}_{N-n}(\mathbf{z}_S)} d\mathbf{x}\, P(\mathbf{x}|\mathrm{T})\, P(\mathbf{x}|\mathbf{z})\, \rho_X(\mathbf{z}) \qquad \text{(B.4)}$$

where we have made use of the fact that $\rho_X(\mathbf{z})$ is only defined on an m-dimensional

surface $\mathcal{S}^m$ which is given by the mapping

$$\mathbf{z} = g(\mathbf{q}) \qquad g : \{\mathbf{q} \in \mathcal{R}^m\} \longrightarrow \left\{\mathbf{z} \in \mathcal{S}^m \subset \mathcal{R}^N\right\} \tag{B.5}$$

Changing variables from $\mathcal{R}^N$ to $\mathcal{R}^m$, we find

$$X(\mathbf{z}_S) = \int_{\mathcal{R}^m} d\mathbf{q} \int_{\mathcal{D}^{\mathbf{x}_0}_{N-n}(\mathbf{z}_S)} d\mathbf{x}\, P(\mathbf{x}|\mathrm{T})\, P(\mathbf{x}|g(\mathbf{q})) \left(\frac{d\mathcal{P}}{d\mathbf{q}}\right) \tag{B.6}$$

where $\left(\frac{d\mathcal{P}}{d\mathbf{q}}\right)$ is proportional to $\left(\frac{d\sigma}{d\mathbf{q}}\right)$, the m-fold differential cross section for an event of kinematic signature $\mathbf{z} = g(\mathbf{q})$.

Experimentally, we are more interested in the number of events which can be associated into a certain acceptance bin $\Delta\mathbf{p}$. $\Delta\mathbf{p}$ is defined in the space of signal parameters $\mathcal{R}^n$ which is mapped into $\mathcal{R}^N$ by

$$\mathbf{z} = f(\mathbf{p}) \qquad f : \{\mathbf{p} \in \mathcal{R}^n\} \longrightarrow \left\{\mathbf{z} \in \mathcal{S}^n \subset \mathcal{R}^N\right\} \tag{B.7}$$

Applying the appropriate coordinate transformation, we find

$$X(\Delta\mathbf{p}) = \int_{\Delta\mathbf{p}} d\mathbf{p}' \sqrt{\det(A^\top A)} \int_{\mathcal{R}^m} d\mathbf{q} \left(\frac{d\mathcal{P}}{d\mathbf{q}}\right) \int_{\mathcal{D}^{\mathbf{x}_0}_{N-n}(f(\mathbf{p}'))} d\mathbf{x}\, P(\mathbf{x}|\mathrm{T})\, P(\mathbf{x}|g(\mathbf{q})) \tag{B.8}$$

where

$$A_{ij} = \frac{\partial f_i}{\partial p'_j} \;\forall\, i = 1 \ldots N,\, j = 1 \ldots n$$

This expression is nice but unwieldy and we will try to develop a more useful form.

Events $\mathbf{x}$ only contribute to X if they are contained in the set of discs $\mathcal{D}^{\mathbf{x}_0}_{N-n}(\mathbf{z}_S)$ around the points $\mathbf{z}_S = f(\mathbf{p}')$. We can make this association explicit by defining a new function $P(f(\mathbf{p}')|\mathrm{T})$ through

$$P(f(\mathbf{p}')|\mathrm{T}) = \frac{\int_{\mathcal{D}^{\mathbf{x}_0}_{N-n}(f(\mathbf{p}'))} d\mathbf{x}\, P(\mathbf{x}|\mathrm{T}) P(\mathbf{x}|\mathbf{z})}{\int_{\mathcal{D}^{\mathbf{x}_0}_{N-n}(f(\mathbf{p}'))} d\mathbf{x}\, P(\mathbf{x}|\mathbf{z})} \tag{B.9}$$

Furthermore, since all of these events $\mathbf{x}$ are associated with a signal event $\mathbf{z}_S$, we do not want to loose them in the trigger. The trigger condition T must therefore be defined in such a way that $P(\mathbf{x}|\mathrm{T})$ (or $P(f(\mathbf{p}')|\mathrm{T})$) is equal to one, except where hardware limits the acceptance $\Delta\mathbf{p}$. From now on we will assume that T indeed satisfies this criterion and set $P(f(\mathbf{p}')|\mathrm{T}) = 1$. This can not be done in the final analysis, where the experimental acceptance has to be folded in properly.

The signal $S(\Delta\mathbf{p})$ is given by

$$S(\Delta\mathbf{p}) = \int_{\Delta\mathbf{p}} d\mathbf{p}' \sqrt{\det(A^\top A)} \int_{\mathcal{R}^n} d\mathbf{p} \left(\frac{d\mathcal{P}}{d\mathbf{p}}\right) \int_{\mathcal{D}_{N-n}^{\chi_0}(f(\mathbf{p}'))} d\mathbf{x}\, P(\mathbf{x}|f(\mathbf{p}))$$

In the linear approximation, where $f(\mathbf{p}) \approx f(\mathbf{p}_0) + A \cdot (\mathbf{p} - \mathbf{p}_0)$ and $\det(A^\top A) \approx$ *constant*, we can simplify

$$\begin{aligned}\int_{\mathcal{D}_{N-n}^{\chi_0}(f(\mathbf{p}'))} d\mathbf{x}\, P(\mathbf{x}|f(\mathbf{p})) &= \left\{\int_{\mathcal{D}_{N-n}^{\chi_0}(f(\mathbf{p}'))} d\mathbf{x}_{N-n} \left(\frac{1}{\sqrt{2\pi}}\right)^{N-n} e^{-\frac{1}{2}\mathbf{x}_{N-n}^2}\right\} \times \\ &\quad \left(\frac{1}{\sqrt{2\pi}}\right)^{n} e^{-\frac{1}{2}d^2(f(\mathbf{p}')|f(\mathbf{p}))} \\ &= \mathcal{G}_{N-n}(\chi_0^2) \left(\frac{1}{\sqrt{2\pi}}\right)^{n} e^{-\frac{1}{2}d^2(f(\mathbf{p}')|f(\mathbf{p}))} \qquad \text{(B.10)}\end{aligned}$$

where $\mathcal{G}_{N-n}(\chi_0^2)$ is the integral $\int_0^{\chi_0^2} g_{N-n}(\chi^2)d\chi^2$ over a χ^2-distribution of (N-n) degrees of freedom, $g_{N-n}(\chi^2)$. We can define χ_0^2 through

$$\mathcal{G}_{N-n}(\chi_0^2) = 1 - \alpha \qquad \text{(B.11)}$$

where α is the fraction of good signal events which are lost due to the cut $\chi^2(\mathbf{z}_S|\mathbf{x}) = d^2(\mathbf{z}_S|\mathbf{x}) \leq \chi_0^2$. A typical choice for α is $\alpha = 0.1$ [53, page 260].

With this result, we can show that for $\left(\frac{d\mathcal{P}}{d\mathbf{p}}\right) = C \cdot \left(\frac{d\sigma}{d\mathbf{p}}\right) \approx constant = \left(\frac{d\mathcal{P}}{d\mathbf{p}'}\right)$

$$\begin{aligned}S(\Delta\mathbf{p}) &= (1-\alpha) \int_{\Delta\mathbf{p}} d\mathbf{p}' \left(\frac{d\mathcal{P}}{d\mathbf{p}'}\right) \int_{\mathcal{R}^n} d\mathbf{p} \sqrt{\det A^\top A} \left(\frac{1}{\sqrt{2\pi}}\right)^{n} e^{-\frac{1}{2}d^2(f(\mathbf{p}')|f(\mathbf{p}))} \\ &= (1-\alpha) \int_{\Delta\mathbf{p}} d\mathbf{p}' \left(\frac{d\mathcal{P}}{d\mathbf{p}'}\right) \int_{\mathcal{S}^n} d\mathcal{S}^n \left(\frac{1}{\sqrt{2\pi}}\right)^{n} e^{-\frac{1}{2}(\mathbf{s}'-\mathbf{s})^2} \\ &= (1-\alpha) \int_{\Delta\mathbf{p}} d\mathbf{p}' \left(\frac{d\mathcal{P}}{d\mathbf{p}'}\right)\end{aligned}$$

which confirms that, in the case of constant cross section, the expected number of signal events S is *not* affected by a finite detector resolution.

In the linear approximation, we can also find an expression for $\sqrt{\det A^\top A} =$ *constant*

$$\sqrt{\det A^\top A} = \left[\int_{\mathcal{R}^n} d\mathbf{p} \left(\frac{1}{\sqrt{2\pi}}\right)^{n} e^{-\frac{1}{2}d^2(f(\mathbf{p}')|f(\mathbf{p}))}\right]^{-1} \qquad \text{(B.12)}$$

which we can exploit to derive

$$S(\Delta\mathbf{p}) = (1-\alpha)\,\Delta\mathbf{p}\, \frac{\int_{\Delta\mathbf{p}} d\mathbf{p}' \int_{\mathcal{R}^n} d\mathbf{p}\, e^{-\frac{1}{2}d^2(f(\mathbf{p}')|f(\mathbf{p}))} \left(\frac{d\mathcal{P}}{d\mathbf{p}}\right)}{\int_{\Delta\mathbf{p}} d\mathbf{p}' \int_{\mathcal{R}^n} d\mathbf{p}\, e^{-\frac{1}{2}d^2(f(\mathbf{p}')|f(\mathbf{p}))}}$$

$$\overline{\left(\frac{d\sigma}{dp}\right)}(\Delta \mathbf{p}) = \frac{\int_{\Delta \mathbf{p}} d\mathbf{p}' \int_{\mathcal{R}^n} d\mathbf{p}\, e^{-\frac{1}{2}d^2(f(\mathbf{p}')|f(\mathbf{p}))} \left(\frac{d\sigma}{d\mathbf{p}}\right)}{\int_{\Delta \mathbf{p}} d\mathbf{p}' \int_{\mathcal{R}^n} d\mathbf{p}\, e^{-\frac{1}{2}d^2(f(\mathbf{p}')|f(\mathbf{p}))}}$$

$$\overline{\mathcal{A}}(\Delta \mathbf{p}) = \frac{\int_{\Delta \mathbf{p}} d\mathbf{p}' \int_{\mathcal{R}^n} d\mathbf{p}\, e^{-\frac{1}{2}d^2(f(\mathbf{p}')|f(\mathbf{p}))} \left(\frac{d\sigma}{d\mathbf{p}}\right) \mathcal{A}}{\int_{\Delta \mathbf{p}} d\mathbf{p}' \int_{\mathcal{R}^n} d\mathbf{p}\, e^{-\frac{1}{2}d^2(f(\mathbf{p}')|f(\mathbf{p}))} \left(\frac{d\sigma}{d\mathbf{p}}\right)} \tag{B.13}$$

i.e. we have a measure of how strongly a finite detector resolution affects the expected number of events and the experimental observables $\overline{\left(\frac{d\sigma}{d\mathbf{p}}\right)}(\Delta \mathbf{p})$ and $\overline{\mathcal{A}}(\Delta \mathbf{p})$.

The expression B.10 does not hold in general, because

$$d^2(\mathbf{x}|\mathbf{z}) \neq d^2(\mathbf{x}|f(\mathbf{p}')) + d^2(f(\mathbf{p}')|\mathbf{z})\, \forall\, \mathbf{x} \in \mathcal{D}^{\chi_0}_{N-n}(f(\mathbf{p}'))$$

This was only possible in the linear approximation with $\mathbf{z} = f(\mathbf{p})$, where the vectors $(\mathbf{x} - f(\mathbf{p}'))$ and $(f(\mathbf{p}') - f(\mathbf{p}))$ are indeed orthogonal. The value of

$$\mathcal{D}(f(\mathbf{p}')|g(\mathbf{q})) = \int_{\mathcal{D}^{\chi_0}_{N-n}(f(\mathbf{p}'))} d\mathbf{x}\, P(\mathbf{x}|g(\mathbf{q})) \tag{B.14}$$

depends on the orientation of the disc $\mathcal{D}^{\chi_0}_{N-n}(f(\mathbf{p}'))$ relative to the vector $(f(\mathbf{p}') - g(\mathbf{q}))$. However, we can estimate $\mathcal{D}(f(\mathbf{p}')|g(\mathbf{q}))$ by extending $\mathcal{D}_{N-n}$ to an N-dimensional ball $\mathcal{D}_N$, in which case orientation becomes meaningless. Applying the same procedure to the signal S allows us to quantify the backgrounds Q and N through the expressions

$$\eta = \frac{Q}{S} = \frac{\int_{\Delta \mathbf{p}} d\mathbf{p}' \int_{\mathcal{R}^m} d\mathbf{q}\, \mathcal{D}(f(\mathbf{p}')|g(\mathbf{q})) \left(\frac{d\mathcal{P}}{d\mathbf{q}}\right)_Q}{\int_{\Delta \mathbf{p}} d\mathbf{p}' \int_{\mathcal{R}^n} d\mathbf{p}\, \mathcal{D}(f(\mathbf{p}')|f(\mathbf{p})) \left(\frac{d\mathcal{P}}{d\mathbf{p}}\right)_S} \tag{B.15}$$

$$R_x = \frac{N}{S} = \frac{\int_{\Delta \mathbf{p}} d\mathbf{p}' \int_{\mathcal{R}^m} d\mathbf{q}\, \mathcal{D}(f(\mathbf{p}')|g(\mathbf{q})) \left(\frac{d\mathcal{P}}{d\mathbf{q}}\right)_N}{\int_{\Delta \mathbf{p}} d\mathbf{p}' \int_{\mathcal{R}^n} d\mathbf{p}\, \mathcal{D}(f(\mathbf{p}')|f(\mathbf{p})) \left(\frac{d\mathcal{P}}{d\mathbf{p}}\right)_S} \tag{B.16}$$

where we have assumed that $\sqrt{\det A^\top A} \approx$ *constant* over $\Delta \mathbf{p}$. The function $\mathcal{D}$ depends on the dimensions in the problem, n and N, and the loss factor α which determines χ^2_0. $\mathcal{D}$ is well approximated by

$$\mathcal{D}(f(\mathbf{p}')|g(\mathbf{q})) \equiv \mathcal{D}(x) \approx Ce^{-\frac{1}{2}\beta x} \tag{B.17}$$

with $x = d^2(f(\mathbf{p}')|g(\mathbf{q}))$, β is a constant and C is an arbitrary normalization (see table 20).

n	N	α	β
4	8	0.7	0.5847
4	8	0.8	0.5123
4	8	0.9	0.4130
4	6	0.8	0.6531
4	7	0.8	0.5705
4	8	0.8	0.5123
6	10	0.7	0.6377
6	10	0.8	0.5695
6	10	0.9	0.4716

Table 20. The parameter β in $\mathcal{D}(f(\mathbf{p}')|g(\mathbf{q}))$ as function of n, N and α.

With this estimate for the background contribution, we can also ask how a change in the detector resolution affects the results. The derivative with respect to resolution is defined as

$$\begin{aligned} D_{\sigma_i}X &\equiv \frac{1}{X}\cdot\sigma_i\cdot\frac{\partial}{\partial\sigma_i}X \qquad\qquad (B.18)\\ &= -1+\beta\,\frac{\int_{\Delta\mathbf{p}}d\mathbf{p}'\int_{\mathcal{R}^m}d\mathbf{q}\;(f_i(\mathbf{p}')-g_i(\mathbf{q}))^2\,\mathcal{D}(f(\mathbf{p}')|g(\mathbf{q}))\left(\frac{d\mathcal{P}}{d\mathbf{q}}\right)}{\int_{\Delta\mathbf{p}}d\mathbf{p}'\int_{\mathcal{R}^m}d\mathbf{q}\,\mathcal{D}(f(\mathbf{p}')|g(\mathbf{q}))\left(\frac{d\mathcal{P}}{d\mathbf{q}}\right)} \end{aligned}$$

$$\begin{aligned} \frac{\Delta X}{X} &= \sum_i\left(\frac{\Delta\sigma_i}{\sigma_i}\right)D_{\sigma_i}X\\ D_{\sigma_i}\eta &= D_{\sigma_i}Q-D_{\sigma_i}S\\ D_{\sigma_i}R_x &= D_{\sigma_i}N-D_{\sigma_i}S \qquad\qquad (B.19) \end{aligned}$$

and can be used to study η and R_x, which enter in the expression for the measurement error of the asymmetry (equation 8.9 on page 43) as functions of σ_i. We have seen in chapter 15 how these expressions can be used to study background and to find possible trade-offs between detector specifications.

Before we leave this chapter we should ask how the results change in experiments where a full blown χ^2-analysis is not necessary. This could be the case for

an analysis of pion-proton elastic scattering data, where cuts on the variables

$$\begin{aligned}(q_\pi - q_\pi^{ES}(\alpha_\pi)) &= \text{the pion momentum} \\ (T_p - T_p^{ES}(\alpha_\pi)) &= \text{the proton kinetic energy} \\ T_0 - T_\pi - T_p &= \text{the missing energy}\end{aligned}$$

are sufficient to reduce the background to acceptable levels. Instead of using a χ^2-fit to associate a measurement $\mathbf{x}$ to a signal event $\mathbf{z}_S$, we use elements of the vector $\mathbf{x}$ itself (such as α_π, or the missing energy which we know must be zero for $\pi^+ p$ scattering). The disc $\mathcal{D}_{N-n}^{\chi_0}(f(\mathbf{p}'))$ turns into a hypercube $\mathcal{C}_{N-n}^{\chi_0}(f(\mathbf{p}'))$ centered at $f(\mathbf{p}')$ with sides $2\chi_0$. By approximating $\mathcal{C}_{N-n}$ by a ball $\mathcal{D}_N$, we get back our original derivation, which can still be used to estimate the background and choose the desired detector resolution.

B.1 Summary

We have seen how to relate the experimental observables, $\overline{\frac{d\sigma}{d\mathbf{p}}}$ and $\overline{\mathcal{A}}$, which are affected by acceptance, detector resolution and analysis strategy, to the theoretical predictions, $\frac{d\sigma}{d\mathbf{p}}$ and $\mathcal{A}$. We have seen how the background enters into these expressions through η and R_x and how we can estimate its size. The derivations are general and can be utilized to study the design of any experiment.

Appendix C

Chamber Algorithms

C.1 The Chamber Geometry

In order to reconstruct the track of a particle through the spectrometer it is necessary to know the orientation of every wire relative to some coordinate system – typically the lab system. The desired positioning accuracy is of order μm which is not easily achieved in commercial production processes. In practise, this means that some construction parameters will be specified with rather small tolerances while others will be measured after the chamber is fully assembled and operational.

The parameters which had to be fixed in the construction phase for these chambers were :

- a constant spacing between wires within a plane with a tolerance of 0.18 mm. This was achieved by stringing the wires on a specifically designed table with threaded rods on either end. The thread provided the needed accuracy in the wire spacing while the orientation of each plane relative to the wires was fixed by two bolts connected to opposite corners of the wire frame.

- The width of each plane (normal to the wire plane) was kept constant to within 0.13 mm. This guaranteed that all planes were parallel after they had been assembled into a chamber.

- The orientation of the wires relative to the midplane of the chamber was fixed by those same bolts which were utilized during the stringing of the wires.

The parameters which were measured after the chambers had been mounted to the magnet and after the completed spectrometer was positioned in the experimental hall were :

- The orientation of the chambers relative to the target. The midplanes of the chambers were aligned with the scattering plane (or rather the beam axis) with the help of special surveillance gear.

Some parameters are not accessible for precise measurements after the chamber has been assembled. They have to be determined through a detailed analysis of the response of the chamber to straight-through particle tracks. In this experiment the parameters which had to be determined in this way were :

- the distances between individual wire planes
- shifts of one wire plane relative to another in a direction normal to both the wire and the plane axis

Figures 61 and 62 illustrate those two cases and define the variables which need to be derived from the data. After a track has been selected and parameterized, the residual errors δ_i tell us about necessary shifts and scale changes based on the following algorithms :

1. **Shifts**

   We begin by expressing the real coordinates of the track in terms of the observed coordinates and three independent correction parameters :

$$\begin{aligned} x_1 &= x_{o1} - r_{MPMP} - r_{MPPM} - r_{MMPP} \\ x_2 &= x_{o2} + r_{MPMP} + r_{MPPM} - r_{MMPP} \\ x_3 &= x_{o3} - r_{MPMP} + r_{MPPM} + r_{MMPP} \\ x_4 &= x_{o4} + r_{MPMP} - r_{MPPM} + r_{MMPP} \end{aligned} \tag{C.1}$$

   What we measure, however, is the difference between observed coordinates and the coordinates obtained from a straight line fit to the observed track

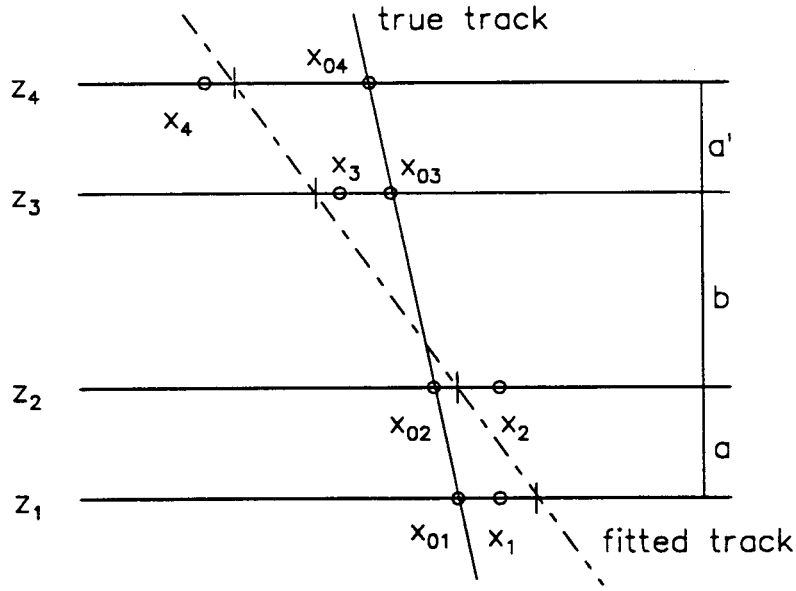

Figure 61. The definition of the chamber geometry : shifts.

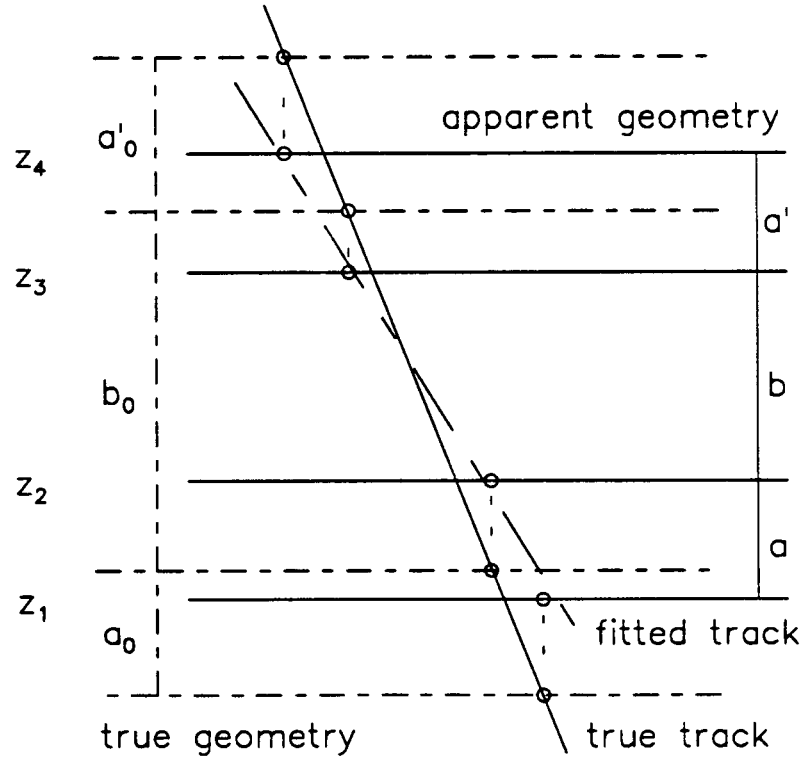

Figure 62. The definition of the chamber geometry : scale changes.

positions :

$$\delta_i = x_{oi} - \hat{x}_i, \quad \mathrm{i} = 1 \ldots 4 \tag{C.2}$$

The correction parameters r are expressed in terms of the δ_i as

$$\begin{aligned} r_{MPMP} &= \frac{1}{4}(\delta_1 - \delta_2 + \delta_3 - \delta_4) \\ r_{MPPM} &= \frac{1}{4}(\delta_1 - \delta_2 - \delta_3 + \delta_4) \\ r_{MMPP} &= \frac{1}{4}(\delta_1 + \delta_2 - \delta_3 - \delta_4) \end{aligned} \tag{C.3}$$

This definition of the correction parameters is useful for a local track fit, where we only look at one chamber coordinate, as well as for a global track fit, where we look at all chamber coordinates. The latter is only useful for straight through tracks (with B = 0), while the former is applicable for any track.

2. **Scale Changes**

We can relate the true distances between planes, a_0, a_0', and $D_0 = b_0 + \frac{1}{2}(a_0 + a_0')$, to the currently accepted distances, a, a', and $D = b + \frac{1}{2}(a + a')$, through the following algorithms which are based on the variables δ_i which have been defined above :

$$\begin{aligned} (\delta_1 - \delta_2) = 2(r_{MPMP} + r_{MPPM}) &= -sa\left(1 - \frac{a_0}{a}\right) \\ (\delta_3 - \delta_4) = 2(r_{MPMP} - r_{MPPM}) &= -sa'\left(1 - \frac{a_0'}{a'}\right) \\ r_{MMPP} &= -\frac{1}{2}sD\left(1 - \frac{D_0}{D}\right) \end{aligned} \tag{C.4}$$

These definitions only apply to straight through tracks and a global line fit to the track positions.

The two methods are independent due to their different dependence on the slope s of the track. They provide, in conjunction with global data on the target spot location and the mean of the angular distribution of tracks, a unique solution to the problem of defining the geometry of the chambers relative to the lab system.

C.2 The Time-to-Space Transformation

We can define $x(t)$ with the simple assumption that the flux of tracks through the volume of one cell is constant (figure 63).

$\frac{dN}{dx} = C$ = a constant density of tracks across the cell volume

$\frac{dN}{dt} = R(t)$ = the accumulated spectrum of TDC values for this cell or a collection of identical cells

$$\left(\frac{dN}{dt}\right) = \left(\frac{dN}{dx}\right) \cdot \left(\frac{dx}{dt}\right) = C \cdot \left(\frac{dx}{dt}\right)$$

$$x(t) = \int \left(\frac{dx}{dt}\right) dt = \int \frac{1}{C} \left(\frac{dN}{dt}\right) dt \propto \int R(t)\, dt \qquad \text{(C.5)}$$

Given the square geometry of the cell and the resulting dependence of the electric field on position, $x(t)$ will also depend on the angle of the track with respect to the normal of the chamber plane, i.e. $x = x(t, \alpha)$.

Furthermore, the zero of the TDC spectrum is not well defined and must be fine-tuned to data due to the large acceleration of electrons around the anode and due to varying pathlengths between the track position and the electronics. The same is true for the overall $x(t)$-dependence. Ideally, one would like to restrict the data to good tracks only in the tuning procedure, but this requires a well-defined time-to-space calibration which is not yet available. In order to find $x(t, \alpha)$, we have to go through several calibration cycles with the hope that each new cycle is based on a more reliable calibration than the one before. The calibration loop is defined as the following sequence of steps :

1. Define the geometry of the chamber cell (see the last section).
2. Build up a representation of the zero point of the TDC spectrum for each wire. A knowledge of the previous map $x(t, \alpha) : t \rightarrow x$ is used to guess where the zero should be.
3. Build up a representation of $x(t, \alpha)$ based on a set of reference tracks.
4. Go back to step 1.

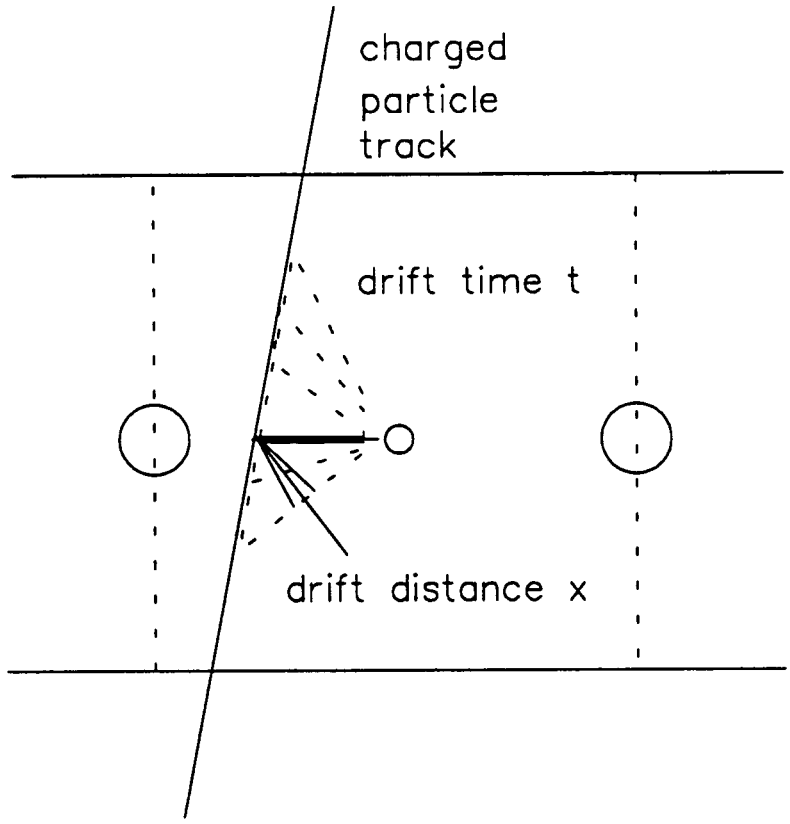

Figure 63. The time-to-space transformation defined in terms of chamber data.

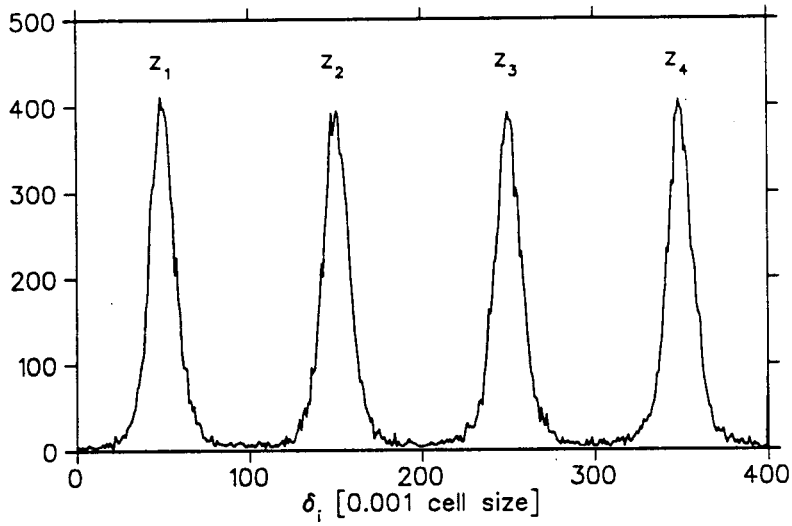

Figure 64. Results of the $x(t, \alpha)$ calibration procedure. We show residual errors $x_{observed} - x_{fit}$ for the x-coordinate of the chamber closest to the target. Distributions are shown for all four wire planes, z_1 — z_4.

The loop ends as soon as the results of the calibration, i.e. the position resolutions as measured by the residual errors $(x_{oi} - \hat{x}_i)$, have stabilized.

The results are shown in figure 64 and the final measured position resolutions for all coordinates are listed in table 21.

The residual errors between the track fit and the measured positions are a valuable analysis tool. They allow us to study, for example, the effect of the PACMAN magnetic field on tracking. Figure 65 shows the residual errors for the w-coordinate for the cases "spectrometer magnet ON" and "spectrometer magnet

coordinate	δx
x	0.35 mm
y	0.40 mm
w	0.70 mm
v	0.70 mm

Table 21. Position resolution for each chamber coordinate.

OFF". In the "magnet OFF" case, oscillations of the error on a cell boundary have developed, indicating that the map $x(t, \alpha)$ is sensitive to the magnetic field at the chamber location. Since we need the analysis of straight-through tracks for the definition of the cell geometry relative to the laboratory system, calibration procedures have to be developed, which take this effect into account.

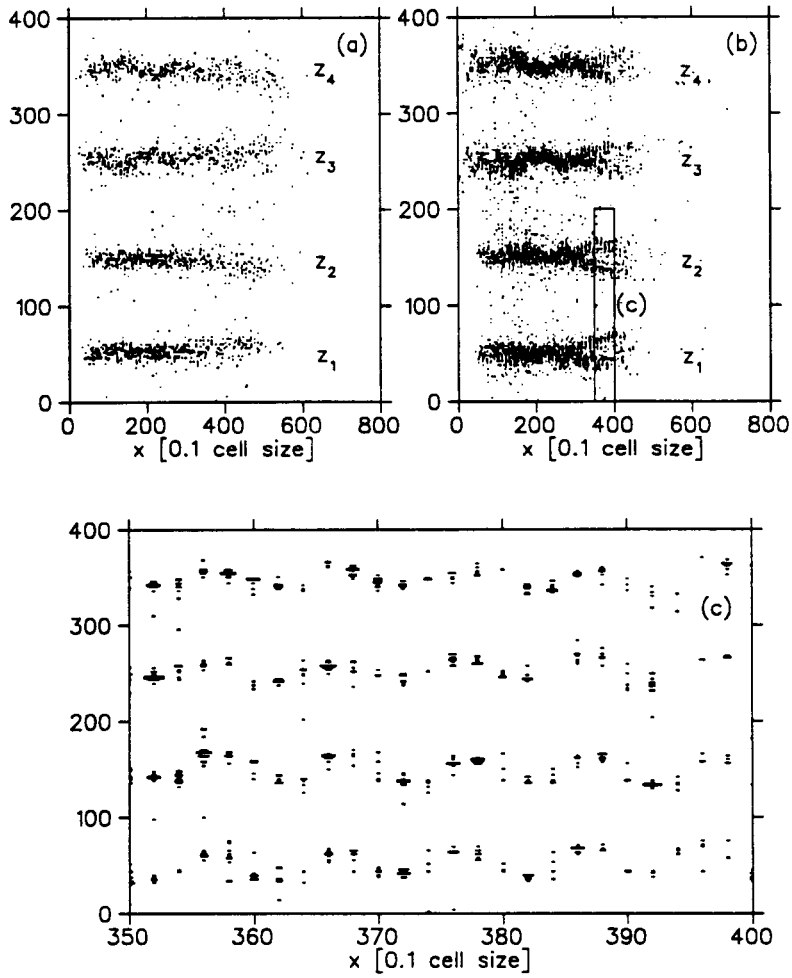

Figure 65. The residual errors of the track as a measure of the effect of the magnetic field on tracking. The residual errors are plotted as a function of the position of the track at the location of the chamber for (a) field ON and (b) field OFF. Figure (c) shows an enlarged section of figure (b), where oscillations of the residual errors on a cell boudary have developed.

Appendix D

The Track Model

The central piece of the pion spectrometer is PACMAN, a large dipole magnet with a pole width of 68 cm and a pole gap of, for this experiment, 30 cm. The large size of the gap relative to the width implies a fringe field which extends far beyond the pole face and can not be neglected in the analysis of spectrometer data. The 3 inch thick field clamps limit the extent of the magnetic field somewhat (see figure 66), but the problem of tracking the particle through the fringe field is still non-trivial.

Instead of struggling with three-dimensional tracking algorithms and the task of measuring the field in sufficient detail, we chose to determine the momentum calibration from experimentally measured pion tracks with known momentum. The tracks came from elastic pion-proton scattering on a liquid hydrogen target. In order to cover the acceptance in (q_π, α_π) needed for bremsstrahlung, data were taken over a range of initial pion energies. The calibration which is used for this analysis is based on elastic $\pi^+ p$ scattering at energies T_0 = 265, 205, 145 MeV.

Each track is described by the following set of variables (see figure 67)

$$\vec{m} = \{q, x_{in}, y_{in}, \alpha_{in}, \beta_{in}, x_{ou}, y_{ou}, \alpha_{ou}, \beta_{ou}\} \tag{D.1}$$

which has to be compared to the track model

$$\vec{f}(\vec{q}) = \vec{f}(\{\hat{q}, \hat{x}_{in}, \hat{y}_{in}, \hat{\alpha}_{in}, \hat{\beta}_{in}\}) \tag{D.2}$$

where $\vec{f}(\vec{q})$ is unknown for the time being. However, we know how to relate $\vec{m}$ to $\vec{f}(\vec{q})$:

$$\vec{m} = \vec{f}(\vec{q}) + \vec{\varepsilon} + \vec{M}\vec{S}(\vec{q}) \tag{D.3}$$

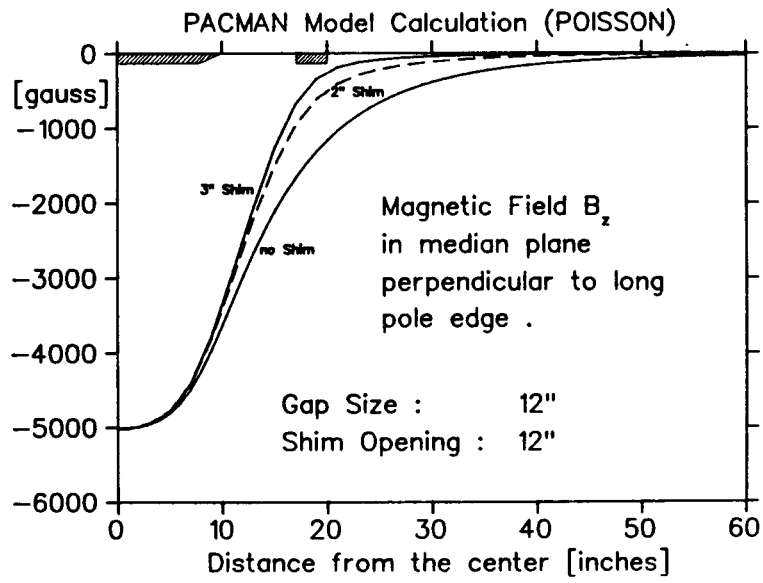

Figure 66. The effect of the field clamps on the PACMAN magnetic field profile.

where $\vec{\varepsilon}$ are Gaussian measurement errors with mean $< \vec{\varepsilon} >= 0$ and $\vec{MS}$ is the multiple scattering contribution [51], whose mean $< \vec{MS} >$ is also zero. The mean $< \cdot >$ here denotes an average over tracks with the same initial conditions. With this we can define

$$\begin{aligned} \vec{f}(\vec{\hat{q}}) &= \{\hat{q}, < x_{in} >, < y_{in} >, < \alpha_{in} >, < \beta_{in} >, \\ &\quad < x_{ou} >, < y_{ou} >, < \alpha_{ou} >, < \beta_{ou} >\} \\ &= \vec{f}(\{\hat{q}, \hat{x}_{in}, \hat{y}_{in}, \hat{\alpha}_{in}, \hat{\beta}_{in}\}) \end{aligned} \tag{D.4}$$

and

$$\{\hat{x}_{in}, \hat{y}_{in}, \hat{\alpha}_{in}, \hat{\beta}_{in}\} = \{< x_{in} >, < y_{in} >, < \alpha_{in} >, < \beta_{in} >\} \tag{D.5}$$

which will be an unbiased predictor for $\vec{m}$. Once we have developed a representation of $\vec{f}(\vec{\hat{q}})$ from our ensemble of pion reference tracks, we can define the momentum of any track through a least squares fit to

$$\frac{1}{2}\left[\vec{m} - \vec{f}(\vec{\hat{q}}) - \vec{MS}(\vec{q})\right]^2$$

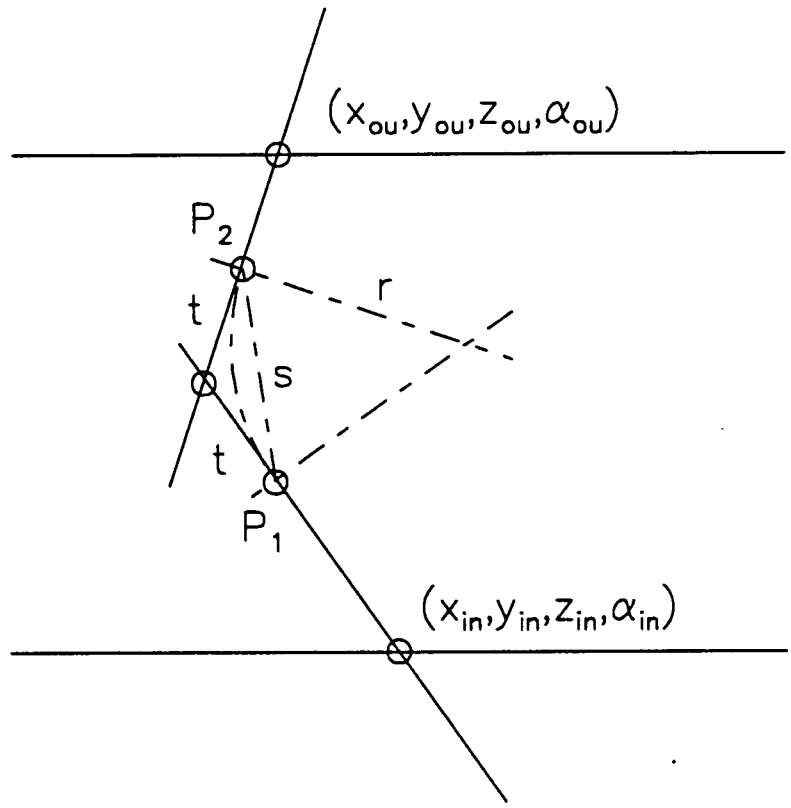

Figure 67. Definition of the variables relevant for the pion momentum calibration ≡ the track model.

where $\vec{MS}$ is a function of $\{\vec{q}\}$ and the multiple scattering angles $\{\Theta, \Psi\}$ with "measurements" $\{\Theta = 0, \Psi = 0\}$.

This procedure is logically straightforward but numerically quite involved, since we have to build the function $\vec{f}(\vec{q})$, which depends on six variables, from a finite set of reference tracks.

D.1 Our Track Model

In the analysis for this experiment we used a different approach which turns out to have some nice properties. The track model for a region of uniform magnetic field is easily defined.

$$\begin{aligned}
\vec{P}_1 &\equiv \{P_{1x}, y_{in}, P_{1z}\} \\
\vec{P}_2 &\equiv \{P_{2x}, y_{ou}, P_{2z}\} \\
s &= 2r \sin\left(\frac{\alpha_B}{2}\right) = \left|\vec{P}_2 - \vec{P}_1\right| \\
t &= r \tan\left(\frac{\alpha_B}{2}\right) = \frac{s}{2\cos\left(\frac{\alpha_B}{2}\right)} \\
r &= = \frac{s}{2\sin\left(\frac{\alpha_B}{2}\right)} \\
\hat{q} &= \frac{0.29979\, B_0\, r}{\cos\left(\frac{1}{2}(\beta_{in} + \beta_{ou})\right)} \\
&\equiv q\,(s, \alpha_B, B_0)
\end{aligned} \tag{D.6}$$

In this model, $\vec{f}(\vec{q})$ is a function of

$$\{\hat{q}, B_0, x_{in}, y_{in}, \alpha_{in}, \beta_{in}, y_{ou}, \beta_{ou}, P_{1x}, P_{1z}, P_{2x}, P_{2z}\}\,.$$

Obviously, it is possible to choose a set $\{P_{1x}, P_{1z}, P_{2x}, P_{2z}\}$ for some fixed B_0 which will correctly predict q for a given track $\vec{m}$. $\left\{\vec{P}_1, \vec{P}_2\right\}$ will be unique for each track and momentum.

Our trick is to force $\left\{\vec{P}_1, \vec{P}_2\right\}$ to be points on smooth boundaries, B_1 and B_2, which will be independent of t: parameters. In other words, we represent the complicated shape of our magnetic field as a region of uniform field with a

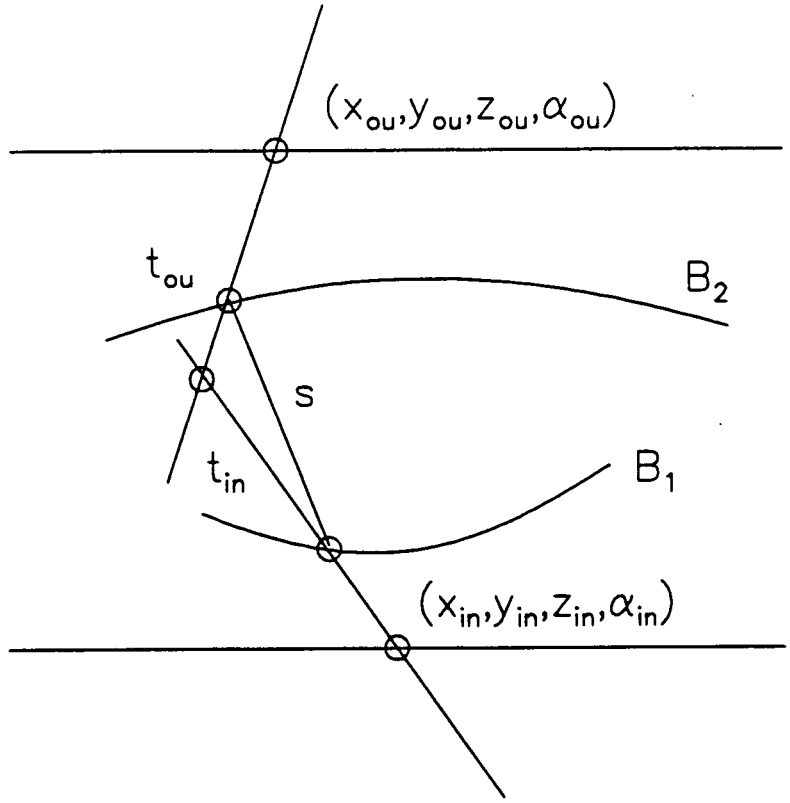

Figure 68. The track model and a typical pion track.

boundary B which is defined as an average of $\left\{\vec{P}_1, \vec{P}_2\right\}$ over all reference tracks :

$$\begin{aligned} B_1(x,y,z) &= < P_{1x}, y_{in}, P_{1z} >_{\text{tracks}} \\ B_2(x,y,z) &= < P_{2x}, y_{in}, P_{2z} >_{\text{tracks}} \end{aligned} \tag{D.7}$$

Given this independently existing boundary, we can predict $\{x_{ou}, \alpha_{ou}\}$ for any $\{\hat{q}, x_{in}, y_{in}, \alpha_{in}, \beta_{in}, y_{ou}, \beta_{ou}\}$. Furthermore, we can immediately define a momentum for any particle track without resorting to the complexities of a least-squares fit, which we will show now.

Since we have fixed the boundaries to be independent of track parameters, the typical situation for a given track $\vec{m}$ will be as shown in figure 68, i.e. the track parameters will not be consistent with the track model $\vec{f}(\vec{q})$, which would predict $t_{in} = t_{ou}$.

We can deal with this in two ways :

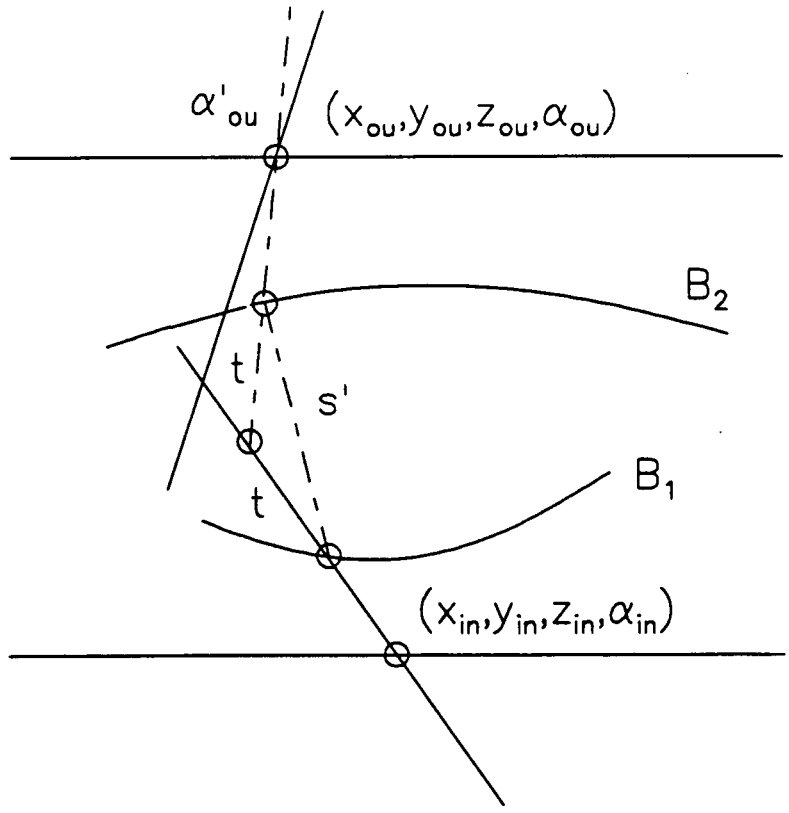

Figure 69. A typical pion track is forced to be consistent with the track model.

1. Ignore the fact that $t_{in} \neq t_{ou}$.

   We define the momentum measurement q as

$$\begin{aligned} q &= q(s, \alpha_B = \alpha_{ou} - \alpha_{in}, B_0) \\ x &= t_{ou} - t_{in} \end{aligned} \tag{D.8}$$

   where x is a measure of how much multiple scattering there was. Pion-decay with the resulting kink in the track is treated just like large angle multiple scattering.

2. Force $t_{in} = t_{ou}$ by replacing α_{ou} with an angle α'_{ou} which is defined entirely on the basis of the field boundary B (see figure 69).

$$q = q(s', \alpha'_B = \alpha'_{ou} - \alpha_{in}, B_0) \tag{D.9}$$

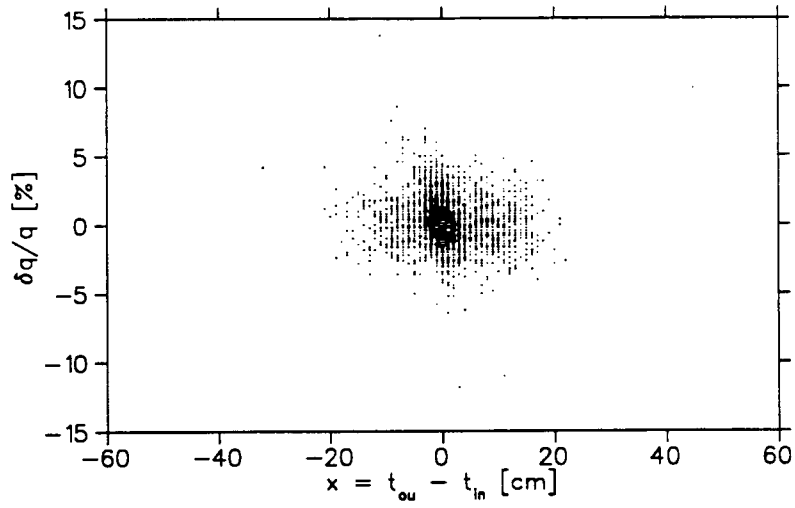

Figure 70. The momentum resolution $\frac{\delta q}{q}$ plotted against our measure for multiple scattering, x, for elastically scattered pions off a liquid hydrogen target.

The latter solution has some remarkable properties :

- The variables $x = t_{ou} - t_{in}$ and $\frac{\delta q}{q} = \frac{(q-\hat{q})}{\hat{q}}$ are uncorrelated ! This implies that π-decay and large angle multiple scattering do not degrade the momentum resolution. Elastic $\pi^+ p$ scattering data on a liquid hydrogen target (see figure 70) support this conclusion.

- The "momentum resolution" $(q-\hat{q})/\hat{q}$ contains contributions coming not only from the momentum calibration but also from the momentum resolution in the initial beam ($\frac{\delta q_0}{q_0} = 1.1$ %) and uncertainties in α_{in}, which are due to measurement errors and multiple scattering in the target. This is so because $\hat{q}$ is really defined in terms of the elastic scattering kinematics $\hat{q} = q_{ES} = f(q_0, \alpha_{in})$.

The momentum resolutions attainable for methods 1 and 2 are

$$\begin{aligned} \text{Method 1 :} \quad (\tfrac{\delta q}{q})_{ES} &= 6.7\ \% \\ \text{Method 2 :} \quad (\tfrac{\delta q}{q})_{ES} &= 4.3\ \% \end{aligned}$$

i.e. the simple change from method 1 to method 2 improves the resolution by 50 % !

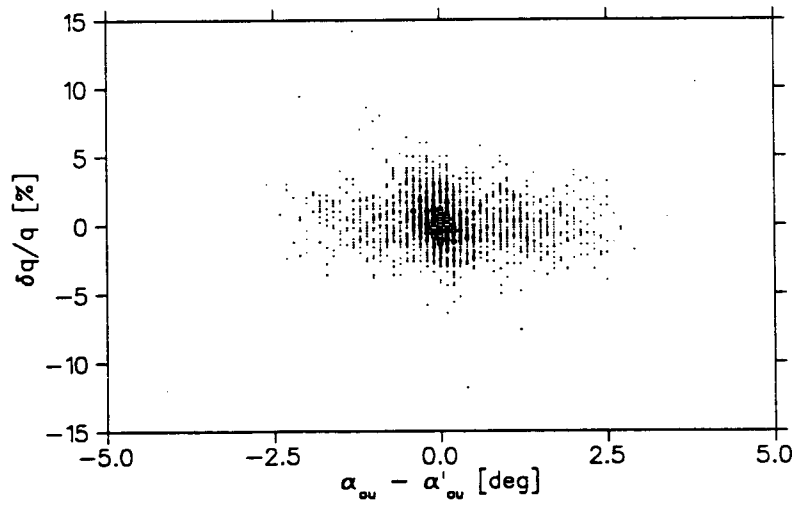

Figure 71. The change in angle, $\alpha_{ou} - \alpha'_{ou}$, plotted against the pion momentum resolution $\frac{\delta q}{q}$.

- Applying a least-squares fit as mentioned above with degrees of freedom for the multiple scattering angles Θ and Ψ does *not* improve the results. In fact, the independence of $\frac{\delta q}{q}$ on multiple scattering/π-decay is lost.

  This can be shown by plotting the change in angle, $\delta\alpha_{ou} = \alpha_{ou} - \alpha'_{ou}$, against the momentum resolution $(\frac{\delta q}{q})_{ES}$ (figure 71). The track model, as it is presented here in terms of a fixed boundary, can deal with large angle multiple scattering or pion decay, because the position of the outgoing track, x_{ou}, is far less sensitive to these effects than the outgoing angle α_{ou}.

  A full least-squares fit, with α_{ou} as one of the parameters to be fitted to, works well only for small angle scattering – larger angle scattering events would have to be rejected. This is supported in figure 72 where we plot the χ^2-distribution against $(\frac{\delta q}{q})_{ES}$. The momentum resolution rapidly deteriorates for large χ^2 values.

These observations imply that method 2 is the optimal algorithm for this choice of a track model.

How does this compare to estimates of the theoretically possible momentum resolution ?

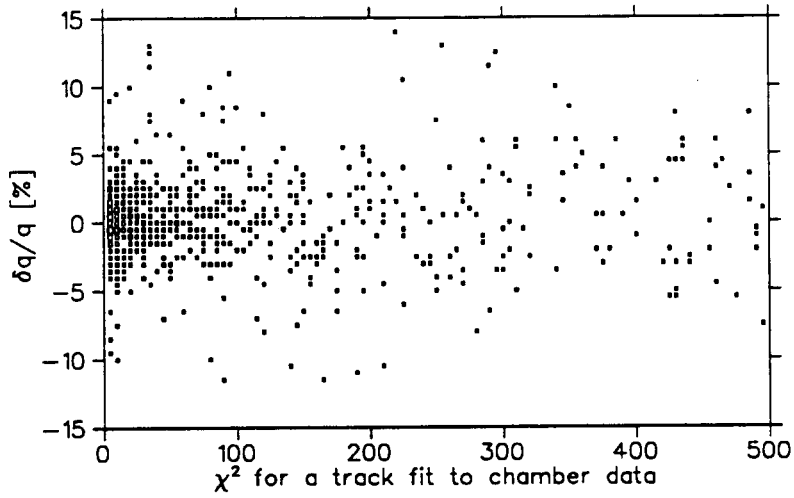

Figure 72. The distribution of χ^2-values, which is obtained from a least-squares fit of tracks to an extended track model, is plotted against the pion momentum resolution $(\frac{\delta q}{q})_{ES}$.

The measured momentum resolution $(\frac{\delta q}{q})_{ES}$ is made up of two contributions

$$\left(\frac{\delta q}{q}\right)_{ES} = \sqrt{\left(\frac{\delta q}{q}\right)^2_{spectrometer} + \left(\frac{\delta q_0}{q}\right)^2} \qquad \text{(D.10)}$$

which have been estimated as

$$\left(\frac{\delta q_0}{q}\right) = f\left(\frac{\delta q_0}{q_0}, \delta\alpha_0, \Theta_{LH_2}\right) = 1.1 \text{ \% FWHM}$$

with

$\left(\frac{\delta q_0}{q_0}\right)$	= 1.1 % FWHM	=	the initial pion momentum resolution
$\delta\alpha_0$	= 1.4° FWHM	=	the beam divergence in the scattering plane
Θ_{LH_2}	= 0.33° FWHM	=	the multiple scattering contribution in the liquid hydrogen target

and

$$\left(\frac{\delta q}{q}\right)_{spectrometer} = 2.7 \text{ \% FWHM}$$

with

$$\left(\frac{\delta q}{q}\right) = \frac{\sqrt{4\Theta^2_{x1} + \frac{1}{2}\Theta^2_{01} + \frac{1}{3}\Theta^2_0}}{\overline{\alpha_B}}$$

Θ_{x1} = 0.26° = the measurement uncertainty in α_{in}

Θ_{01} = 0.14° = the multiple scattering contribution to α_{in} due to the wire chambers in front of the PACMAN magnet

Θ_0 = 0.4° = the multiple scattering contribution to α_B due to the air in the magnetic field region of the spectrometer

$\overline{\alpha_B}$ = 22° = the average bend angle for elastically scattered pions at $T_0 = 265$ MeV

This adds up to a combined value for the theoretical momentum resolution of

$$\left(\frac{\delta q}{q}\right)_{ES} = 3\ \%\ \text{FWHM} \tag{D.11}$$

We conclude that there must exist a third contribution which can only come from the simplifications inherent in the track model of

$$\left(\frac{\delta q}{q}\right)_{track\ model} = \sqrt{\left(\frac{\delta q}{q}\right)^2_{experimental} - \left(\frac{\delta q_0}{q}\right)^2_{theoretical}} \approx 3\ \%\ \text{FWHM}$$

Given the calculational simplicity of the model, its unique features with regard to large angle multiple scattering and π-decay, and the fact that δT_π is already less than the other measurement errors in the experiment, δk and δT_p, no attempt has been made to recover $\left(\frac{\delta q}{q}\right)_{track\ model}$ through a better track model.

This exercise is left to the reader !

Appendix E

Scintillator Readout

The purpose of this chapter is to discuss some of the problems which have to be dealt with in the application of a scintillator - photomultiplier tube - analog-to-digital converter (ADC) readout chain. There exists a saying : *"It has been done many times before"*, which comes in handy as an excuse not to take these problems seriously. The price to be paid is an additional year which has to be spent in data analysis.

There are two sections in this chapter. The first deals with variations in the response of the photomultiplier tube [50]. The second concerns itself with the coupling of the output signal of the phototube to the input of the ADC, and with the shape and pulse height distributions of the signal and their effect on the measurement.

E.1 Gain Variations

The principles of the operation of a photomultiplier tube as a light detector is shown in figure 73. Scintillation light strikes the photocathode and knocks out electrons through the photoelectric effect. These electrons are focused and accelerated by an electric field towards the first dynode where they free more electrons upon impact. These secondary electrons are focused and accelerated towards the second dynode and the process repeats itself. By the time the electrons finally arrive at the anode, a multiplication of the order of 10^3 to 10^8 has taken place and the signal, which

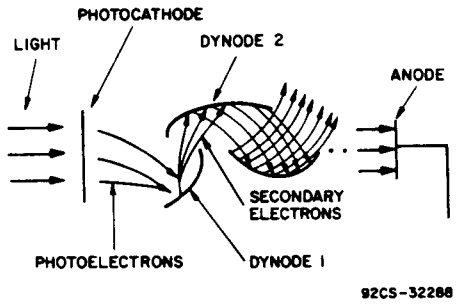

Figure 73. Schematic representation of a photomultiplier tube and its operation.

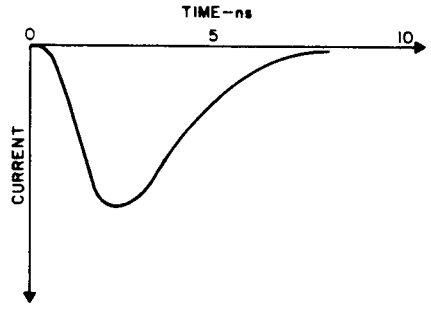

Figure 74. Pulse shape obtained from a photomultiplier excited by a light pulse having a 0.5 ns rise time.

appears at the output of the tube, can be processed by conventional electronics. The high voltage, which is needed to operate the tube, is coming from an external power supply and is distributed to the dynodes by electronics, which is mounted directly to the base of the tube. This electronics is refered to as "the base".

The typical shape of the signal pulse is shown in figure 74. The pulse height depends on the gain of the tube which is determined by the accelerating voltage between dynodes.

Assuming that the high voltage supplied to the tube is properly stabilized, variations of the tube gain can be due to

- Temperature variations

  Both the spectral response of the cathode and the response of the dynodes depend on temperature (figure 75). A change in the temperature of the device can be due to changing operating conditions (there are resistors close to the

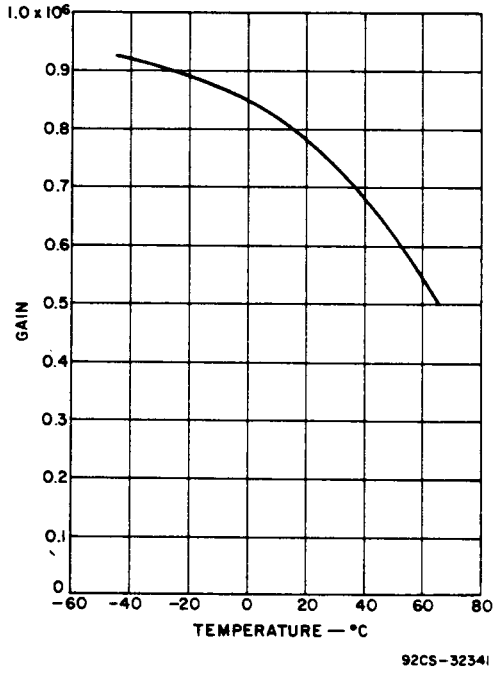

Figure 75. Typical variation of the gain with temperature for a 9-stage photomultiplier tube (type 8571) with Cs-Sb dynodes operating at 100 volts per stage.

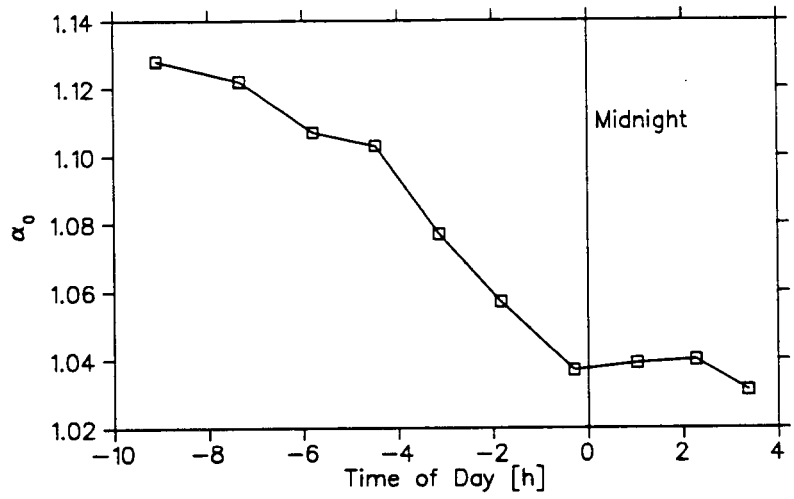

Figure 76. Temperature dependence of the gain of the proton detector $\frac{dE}{dx}$ counter plotted against the time-of-day.

base of the tube which might heat up) or simply due to the change from day to night. Evidence for the latter is visible in figure 76, where the gain α_0 for the proton $\frac{dE}{dx}$ counter is plotted against time.

- Signal current

  - Space charge

    The electron density in the last few stages of the multiplication process may become so high for large signals that interactions between the electrons begin to affect the focusing between dynodes. This effect is refered to as a buildup of space charge. As a result, the gain tends to decrease (see figure 77) as the signal becomes large, i.e. the response of the device has become non-linear. The point at which space charge sets in depends on the tube design and the voltage distribution over the dynodes. In general, a higher voltage between the anode and the last dynode pushes the non-linearity to larger signal currents (this is called a tapered base design because the relative voltage between dynodes rises gradually towards the anode).

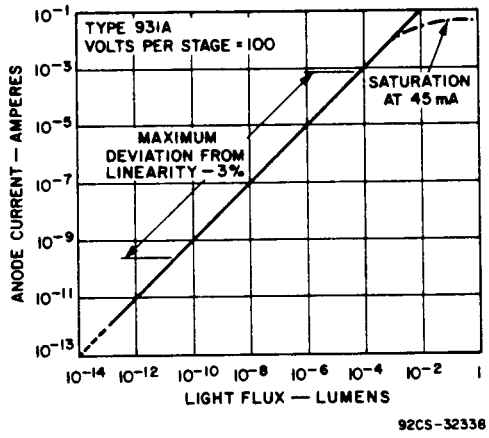

Figure 77. Range of anode-current linearity as a function of the light flux for a 931 A photomultiplier.

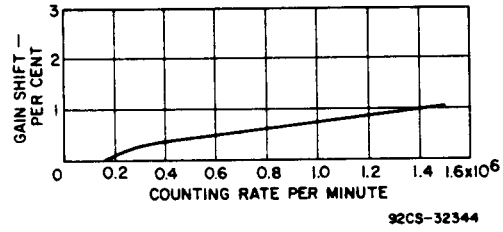

Figure 78. Typical variation of pulse height with pulse-count rate for a 6342A photomultiplier.

– Insulator charging

Even under ideal operating conditions, electrons, which are released from one dynode do not always end up on the active area of the next dynode, but instead hit the insulating support structures. As a result, those structures charge up and develop an electrical field of their own which affects the focusing between the dynodes. The gain changes until an equilibrium between the charging current and the growing focusing by the spacers has been reached. If the average signal current changes, a new equilibrium develops and the overall gain settles to a new value. This process is thought to be the cause of a dependence of the gain on the signal rate (see figure 78). Above 10^5 counts/sec, photomultiplier

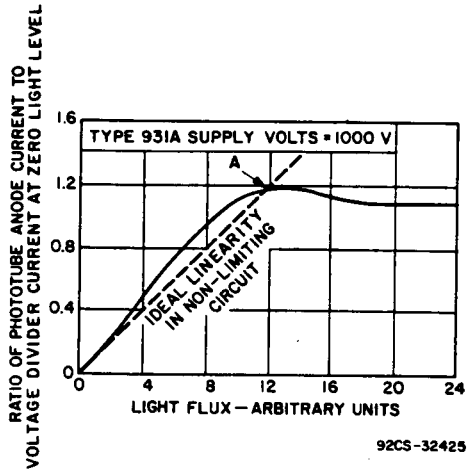

Figure 79. The variation of the gain as a function of signal current for a base design with a simple divider chain.

tubes become particularly sensitive to sudden drops in the count rate. These drops can be caused, for example, by short lapses (of the order of microseconds) of the beam on target.

- The base design

  A common means to provide high voltage to the dynodes is to use a resistor-based divider chain. The current through the resistors must be chosen to be much larger (a factor of 10) than the expected maximum signal current, otherwise the interaction between the two currents will cause a variation in gain as is shown in figure 79.

- Magnetic fields

  Photomultiplier tubes are sensitive to a magnetic field, since it changes the focus between dynodes and, particularly, between the first dynode and the photocathode. The effect on the gain is shown in figure 80 for a typical tube design and various orientations of the magnetic field.

  The tubes which were used for the proton detector were shielded with several layers of metal shielding and were oriented with respect to the magnetic field as in figure 80-2. In this orientation, the magnetic field moves the focus across the

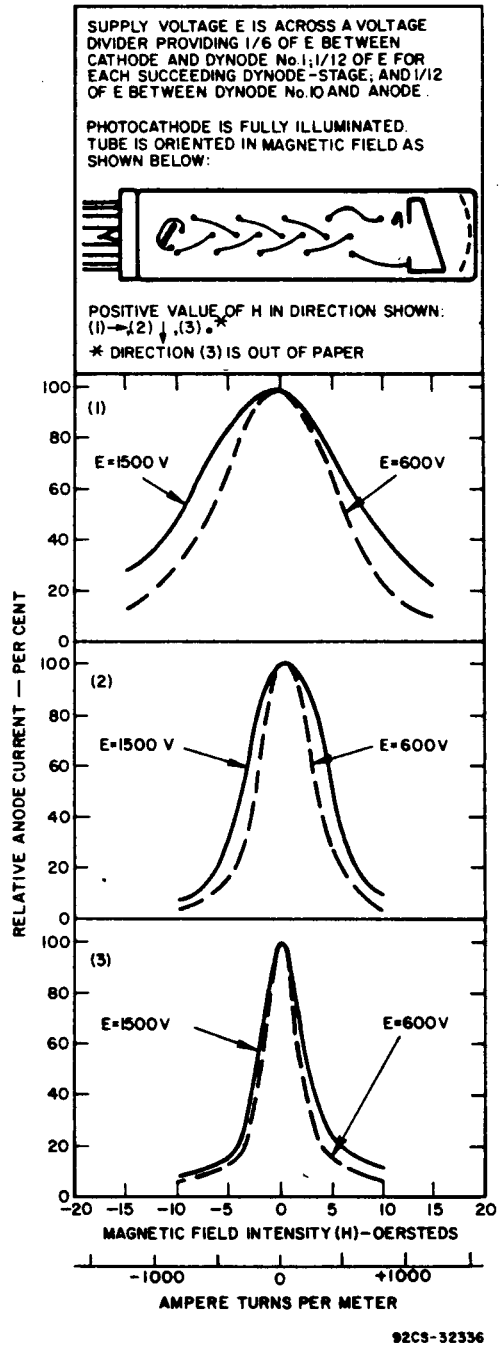

Figure 80. Curves for a $\frac{3}{4}$ inch diameter type 4516 photomultiplier showing the effect of magnetic fields on the anode current.

dynode towards the support structure. Insulator charging and space charge effects are likely going to be more important, and non-linearities in the anode response have to be anticipated (see chapter 18).

The most effective way to deal with gain variations is to choose operating conditions appropriately and to monitor them throughout the experiment. We are talking here about factors such as

- the high voltage applied to the tube,
- the voltage between dynodes, and dynode and anode (i.e. the design of the base),
- the temperature,
- the residual magnetic field (after shielding has been taken into account),
- the count rate,
- the average signal current.

The gain can be monitored by incorporating reference signals into the event stream. These signals can be derived from physical processes like elastic pion-proton scattering, where the energies of the particles are known. This is the ideal case, since the gain is measured under the same conditions under which data are taken, i.e. geometric effects, light collection, saturation in the scintillator and so on are all taken into account.

The alternative to monitoring the gain with reference events, is to feed light directly to the photocathode. This is done by mounting an LED to the lightguide, which connects the scintillator and the photomultiplier tube, with the luminour end pointing towards the phototube. The signal must be calibrated in units of particle energy by the method mentioned before, but only once, i.e. it can be done before or after the experiment and with specialized hardware. The shape of the light pulse can be tailored to approximate a real event by supplying an appropriately shaped voltage pulse to the LED.

Detector	*Beam Rate [MHz]*	*Pedestal Position*
TINA	15	0
	0.2	13
MINA	15	0
	0.2	4

Table 22. The pedestal values for TINA and MINA as a function of beam rate.

The problem with LEDs is that the amount of light released depends not only on voltage but also on temperature and the history of the device. Over a long period of time the LED-based energy calibration is bound to shift. However, LEDs are very good at monitoring short-term gain variations.

A non-linear relationship between scintillation light and the phototube response is only expected under extreme operating conditions such as an excessive magnetic field at the position of the tube or high count rates. The only way to avoid this situation is to carefully check the performance of the detector under those operating conditions, before the experiment gets under way.

E.2 Baseline Shifts and Pile-Up

The photomultiplier tube is coupled to the ADC through a capacitance. This is called "AC-coupled". The signal which is seen by the ADC therefore contains no DC component. Consequently, the pedestal, which is the response of the ADC to no signal, is defined by the average signal current. If the rate of events changes, the average current changes and the pedestal moves, a behaviour which is refered to as a "baseline shift". Experimental evidence for this effect can be found in the photon detector data, since this detector is particularly sensitive to baseline shifts due to the long signal duration of several 100 ns. Table 22 shows values for the pedestals for TINA and MINA for two beam rates. The shift is to be compared to the intrinsic width of the pedestal of 1-2 channels which is due to ever present

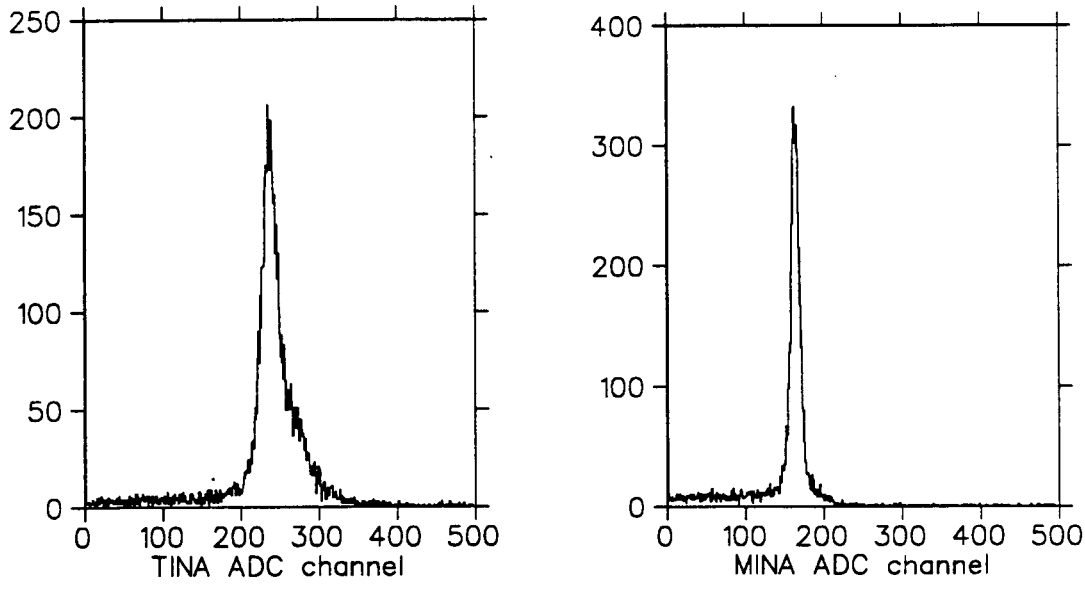

Figure 81. Experimental evidence for pile-up for TINA and MINA.

electrical noise and digitization errors.

Baseline shifts are a long-term effect. On a short time scale of the order of the signal duration, attention has to be paid to "pile-up". Pile-up is simply the corruption of one signal by another which occurs shortly before or after the original one. The ADC measures the overlap of the two. This effect can be quite harmful for signals which decay slowly, as in the case of NaI detectors, and once again, examples for pile-up are shown for TINA and MINA with data taken on the frozen spin target (figure 81). In order to see the pedestal, data have to be taken from a detector which is *not* involved in the event trigger, because otherwise we would only be measuring the detection threshold.

There are various ways to control the pile-up :

- Lower the signal rate.

- Clip the signal.

  The signal is split at the output of the photomultiplier (with a simple resistor-based splitter). One branch connects to the ADC while the other is connected to a piece of wire of length τc, where τ is the time it takes for the signal to

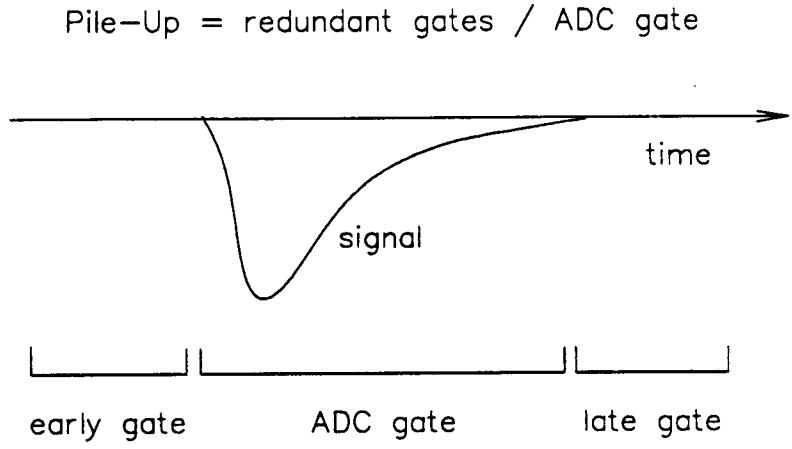

Figure 82. The use of redundant ADC gates to define pile-up.

travel the length of the wire. Depending on how well the wire is electrically terminated (the wire is usually a 50 Ohm BNC cable), part of the signal reflects off the end of the wire and travels back to interfere with the original signal in a destructive manner. The duration of the signal going to the ADC is effectively cut short to a time 2τ. The disadvantages of this method are a large overshoot in the tail of the resulting signal, loss of information due to the lesser charge which is measured by the ADC, and a large sensitivity to the temporal placement of the ADC gate relative to the signal (due to the large overshoot in the tail of the signal).

- Measure the pile-up with redundant ADC gates.

  An example of this technique is shown in figure 82. The disadvantage here is the need for additional ADC gates, i.e. additional electronics hardware and more data per event. The method allows full off-line control over the handling of pile-up information.

Appendix F

The Phenomenological Behaviour of PPID

The variable on which the proton energy calibration is based is

$$\mathrm{PPID}(L_p, L) \equiv \frac{dL_{measured}}{dL_{calculated}(L)} \tag{F.1}$$

where

$dL_{measured}$ = $\alpha_0\, dL(L_p)$

α_0 = gain calibration for the $\frac{dE}{dx}$ counter. $\alpha_0 = 1$, if the calibration is done properly.

$dL(L_p)$ = the light output corresponding to the energy lost by the proton of energy $T_p(L_p)$ in the $\frac{dE}{dx}$ counter.

$T_p(L_p)$ = the relationship between energy lost in a plastic scintillator and the amount of light which can be detected (normalized to $T(L)$ for electrons).

and

$dL_{calculated}$ = $dL(L)$

L = the amount of light detected by the proton detector.

The relation between L and L_p is the outcome of the proton energy calibration and is written as

$$L_p = L_p(L) \tag{F.2}$$

The experimental evidence is described in terms of PPID as

$$\mathrm{PPID}(L_p, L) = \frac{\alpha_0\, dL(L_p)}{dL(L)} = H(L) \tag{F.3}$$

which gives us

$$L_p = dL^{-1}\left\{\frac{1}{\alpha_0} H(L)\, dL(L)\right\} \tag{F.4}$$

This definition of L_p assumes that the functions $dL(L)$ and $T(L)$ are a valid representation of experimental data on energy losses of protons in plastic scintillator (brand name NE 102). In order to check this assumption we have to discuss the origins of $dL(L)$ and $T(L)$.

The function $T(L)$ is a result of simultaneously integrating the Bethe-Bloch equation 18.1 together with equation 18.2, which describes saturation effects in the scintillator (chapter 18) The path length drops out of the relation $T(L)$ and the normalization of $\frac{dE}{dx}$ is not critical. The remaining parameters which affect $T(L)$ are kB and C from equation 18.2. Their values are given in reference [49] as

$$kB = 1.31 \cdot 10^{-2} \pm 10\ \% \quad \text{for the one-parameter fit}$$

$$kB = 1.29 \cdot 10^{-2} \pm 10\ \% \quad \text{for the two-parameter fit}$$
$$C = 9.59 \cdot 10^{-6}$$

Variations of kB and C at the one sigma level shifts $T(L)$ by at most 0.5 MeV which is negligible for this application.

The absolute normalization of $\frac{dE}{dx}$, which was taken from scientific data tables (at TRIUMF, these tables are available through the program LOSSPROG), has an estimated uncertainty of 2-3 % at the highest energies measured (130 MeV) and can go up to 10 % at lower energies where atomic corrections become important.

The data taken in this experiment indicate that there might also exist a systematic uncertainty (see section 18.1). In order to study this possibility it is necessary to look at the qualitative behaviour of PPID(L_p, L). The results will serve as a bench mark and the basis by which we will interpret the experimental data.

The function PPID($\alpha L, L, \alpha_0 = 1$) is shown in figure 83 for various values of α. We can draw several conclusions from these results :

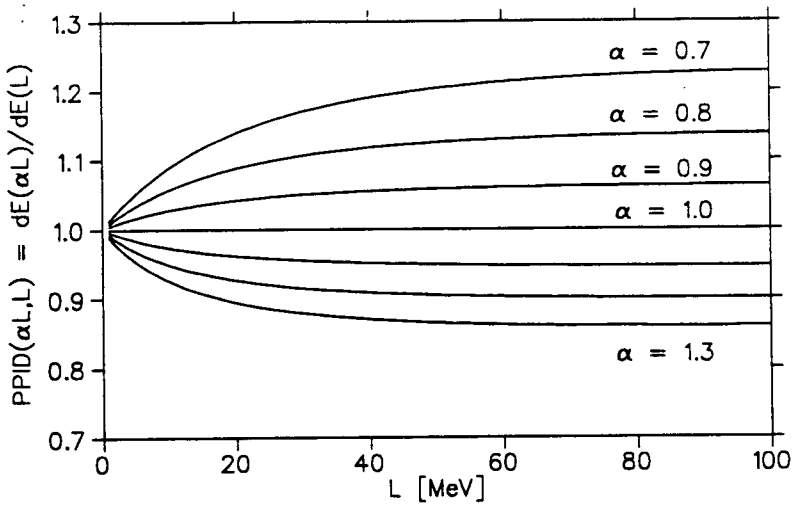

Figure 83. The phenomenological behaviour of PPID($\alpha L, L$).

1. The function PPID(L) has a finite limit for $L \rightarrow 0$ which is independent of the gain parameter α.

$$\lim_{L \to 0} \{\text{PPID}(\alpha L, L)\} \; = \; 1 \; \neq f(\alpha) \tag{F.5}$$

2. However, the derivative of PPID(L) with respect to L at the point $L = 0$ does depend on α :

$$\frac{d}{dL} \left[\text{PPID}(\alpha L, L)\right]_{L=0} \; = \; f(\alpha) \; \approx \; 0.0365 \, (1 - \alpha) \tag{F.6}$$

3. As L becomes large, PPID($\alpha L, L$) becomes approximately constant.

$$\text{PPID}(\alpha L, L) \overset{L>50\,MeV}{\longrightarrow} constant \; = \; f(\alpha) \tag{F.7}$$

Before we attempt to build a consistent energy calibration based on PPID(L_p, L), we have to make sure that the experimental data show the same behaviour as PPID($\alpha L, L$) in the limits where the results are independent of the calibration constant α.

PPID(L, L') can be approximated by the function

$$\text{PPID}(L, L') \approx F(L, L') = \left[\frac{L + a}{L' + a}\right]^{-b} \tag{F.8}$$

with

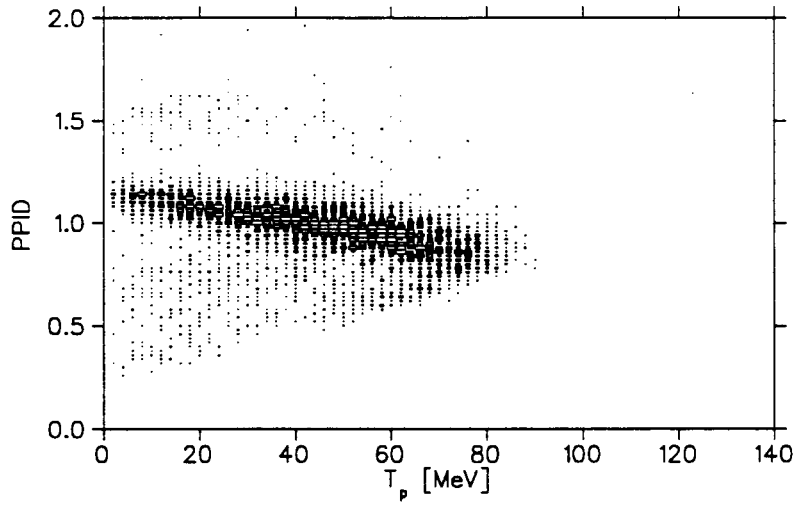

Figure 84. The proton energy non-linearity in terms of PPID.

$$a = 13.03 \pm 0.06 \qquad \text{for } 20 \leq L, L' \leq 100 \text{ MeV}$$
$$b = 0.6744 \pm 0.0007$$

and a maximal error of

$$\left| \text{PPID}(L, L') - \left[\frac{L+a}{L'+a} \right]^{-b} \right| \leq 0.005 .$$

Experimentally, PPID is defined as $\text{PPID}(L_p, L_{measured})$ and its behaviour as based on $\pi \rightarrow ppX$ data off the frozen spin target is shown in figure 84. The results allow us to conclude that there is a need for an energy-dependent calibration, since no constant gain-calibration $L_p = \alpha L_{measured}$ can reproduce the high-energy behaviour of PPID_{exp}.

Appendix G

Derivations

G.1 Derivation of $\left(\frac{\delta S}{S}\right)$

$$\begin{aligned} N &= (S+Q+N_x)-N_x & (\delta N)^2 &= S+Q+2N_x \\ B &= (Q'+M'_x)-M'_x & (\delta B)^2 &= Q'+2M'_x \end{aligned}$$

$$\beta = \frac{M_B}{M} \qquad M_{(B)} = (C\rho\epsilon(R_0\,\Delta t))_{(B)} = (C\rho\epsilon M_0)_{(B)}$$

$$S = N - \frac{1}{\beta}B \qquad Q = \frac{1}{\beta}Q' \qquad N'_x = \frac{1}{\beta}M'_x$$

$$\eta = \frac{Q}{S} \qquad R_x = \frac{N_x}{S} \qquad R'_x = \frac{N'_x}{S}$$

$$\begin{aligned} (\delta S)^2 &= (\delta N)^2 + \frac{1}{\beta^2}(\delta B)^2 + B^2\frac{1}{\beta^2}\left(\frac{\delta\beta}{\beta}\right)^2 \\ &= S+Q+2N_x+\frac{1}{\beta^2}(Q'+2M'_x)+\frac{Q'^2}{\beta^2}\left(\frac{\delta\beta}{\beta}\right)^2 \\ \left(\frac{\delta S}{S}\right)^2 &= \frac{1}{S}\left[(1+\eta+2R_x)+\frac{1}{\beta}(\eta+2R'_x)\right]+\eta^2\left(\frac{\delta\beta}{\beta}\right)^2 \end{aligned} \tag{G.1}$$

$$M_t = M + M_B = constant = M\,(1+\beta) \propto S\,(1+\beta) \Rightarrow \frac{1}{S} \propto (1+\beta)$$

$$\frac{\partial}{\partial\beta}\left[\left(\frac{\delta S}{S}\right)^2\right] = 0 \quad \Rightarrow \quad \beta^2 = \frac{\eta + 2R'_x}{1+\eta+2R_x}$$

$$\eta \to 0 \quad \Rightarrow \quad \beta \to 0$$

$$\left(\frac{\delta S}{S}\right)^2 = \frac{1}{S}(1+\beta)(1+\eta+2R_x) + \eta^2\left(\frac{\delta\beta}{\beta}\right)^2 \tag{G.2}$$

$$\left(\frac{\delta\beta}{\beta}\right)^2 = 2\left\{\left(\frac{\delta\rho}{\rho}\right)^2 + \left(\frac{\delta\epsilon}{\epsilon}\right)^2 + \left(\frac{\delta M_0}{M_0}\right)^2\right\} \tag{G.3}$$

G.2 Derivation of $(\delta\mathcal{A})$

$$M_\uparrow = M_\downarrow \equiv M \qquad P_\uparrow = P_\downarrow = P \qquad S_{\uparrow\downarrow} = M(1 \pm \mathcal{A}P)$$

$$R = \frac{\left(\frac{N_\uparrow}{M_\uparrow} - \frac{B}{M_B}\right) - \left(\frac{N_\downarrow}{M_\downarrow} - \frac{B}{M_B}\right)}{\left(\frac{N_\uparrow}{M_\uparrow} - \frac{B}{M_B}\right) + \left(\frac{N_\downarrow}{M_\downarrow} - \frac{B}{M_B}\right)} \qquad \beta \equiv \frac{M_B}{M} \tag{G.4}$$

$$\mathcal{A} = \frac{2R}{[P_\uparrow + P_\downarrow] - [P_\uparrow - P_\downarrow]R} \tag{G.5}$$

$$\begin{aligned}
4(\delta R)^2 \;=\; & \frac{1}{M^2}(1-\mathcal{A}P)^2(\delta N_\uparrow)^2 \\
& + \frac{1}{M^2}(1+\mathcal{A}P)^2(\delta N_\downarrow)^2 \\
& + \left(1+\mathcal{A}P+\frac{B}{M_B}\right)^2(1-\mathcal{A}P)^2\left(\frac{\delta M_\uparrow}{M_\uparrow}\right)^2 \\
& + \left(1-\mathcal{A}P+\frac{B}{M_B}\right)^2(1+\mathcal{A}P)^2\left(\frac{\delta M_\downarrow}{M_\downarrow}\right)^2 \\
& + 4(\mathcal{A}P)^2\frac{1}{M_B^2}(\delta B)^2 \\
& + 4(\mathcal{A}P)^2\frac{B^2}{M_B^2}\left(\frac{\delta M_B}{M_B}\right)^2
\end{aligned}$$

$$
\begin{aligned}
&= \frac{2}{M}\left[\left(1-\mathcal{A}^2P^2\right)+\left(1+\mathcal{A}^2P^2\right)(\eta+2R_x)+2\mathcal{A}^2P^2\frac{1}{\beta}(\eta+2R_x')\right] \\
&\quad +2\left[\left(1-\mathcal{A}^2P^2\right)^2+2\eta\left(1-\mathcal{A}^2P^2\right)+\eta^2\left(1+\mathcal{A}^2P^2\right)\right]\left(\frac{\delta M}{M}\right)^2 \\
&\quad +4\mathcal{A}^2P^2\eta^2\left(\frac{\delta M_B}{M_B}\right)^2 \\
&\leq 2\left\{\frac{1}{M}\left[(1+2\eta+4R_x)+2\beta(1+\eta+2R_x)\right]\right. \\
&\quad \left.\left(1+2\eta+2\eta^2\right)\left(\frac{\delta M}{M}\right)^2+2\eta^2\left(\frac{\delta M_B}{M_B}\right)^2\right\}
\end{aligned}
$$

$$
\begin{aligned}
(\delta\mathcal{A})^2 &\approx \frac{1}{4P^2}\left\{4(\delta R)^2+2\mathcal{A}^2P^2\left(1+\mathcal{A}^2P^2\right)\left(\frac{\delta P}{P}\right)^2\right\} \\
&\leq \frac{1}{P^2}(\delta R)^2+\left(\frac{\delta P}{P}\right)^2 \\
&\leq \frac{1}{2P^2}\left\{\frac{1}{M}\left[(1+2\eta+4R_x)+2\beta(1+\eta+2R_x)\right]\right. \\
&\quad \left.+\left(1+2\eta+2\eta^2\right)\left(\frac{\delta M}{M}\right)^2+2\eta^2\left(\frac{\delta M_B}{M_B}\right)^2\right\} \\
&\quad +\left(\frac{\delta P}{P}\right)^2 \qquad \text{(G.6)}
\end{aligned}
$$

$$
\begin{aligned}
\left(\frac{\delta M}{M}\right)^2 &= \left(\frac{\delta M_0}{M_0}\right)^2+\left(\frac{\delta\epsilon}{\epsilon}\right)^2 \\
\left(\frac{\delta M_B}{M_B}\right)^2 &= \left(\frac{\delta M_0}{M_0}\right)^2+\left(\frac{\delta\epsilon}{\epsilon}\right)^2+2\left(\frac{\delta\rho}{\rho}\right)^2
\end{aligned}
$$

$$
(\delta\mathcal{A})^2 \overset{\eta=0}{\leq} \frac{1}{2P^2}\left\{\frac{1}{M}(1+4R_x)+\left(\frac{\delta M_0}{M_0}\right)^2+\left(\frac{\delta\epsilon}{\epsilon}\right)^2\right\}+\left(\frac{\delta P}{P}\right)^2 \qquad \text{(G.7)}
$$

G.3 Derivation of $(\delta\mathcal{A})$ for Experimental Data

$$
\begin{aligned}
P_\uparrow &= \frac{1}{n_+}\sum_{i=1}^{n_+}P_{\uparrow i} & (\delta P_\uparrow)^2 &= \frac{1}{n_+}(\delta P)^2 \\
P_\downarrow &= \frac{1}{n_-}\sum_{i=1}^{n_-}P_{\downarrow i} & (\delta P_\downarrow)^2 &= \frac{1}{n_-}(\delta P)^2 \qquad \text{(G.8)}
\end{aligned}
$$

$$\mathcal{A} = \frac{2R}{[P_\uparrow + P_\downarrow] - [P_\uparrow - P_\downarrow]\, R} \qquad R \overset{\eta=0}{=} \frac{X_\uparrow - X_\downarrow}{X_\uparrow + X_\downarrow}$$

$$X_\uparrow = \frac{1}{n_+} \sum_i \left(\frac{N_\uparrow}{M_\uparrow}\right)_i \qquad X_\downarrow = \frac{1}{n_-} \sum_i \left(\frac{N_\downarrow}{M_\downarrow}\right)_i \qquad M_{\uparrow\downarrow} = (M_0\, \epsilon)_{\uparrow\downarrow}$$

$$\begin{aligned}(\delta\mathcal{A})^2 \;=\; & \frac{4}{[(P_\uparrow + P_\downarrow) - (P_\uparrow - P_\downarrow)\, R]^4} \times \\ & \left\{(P_\uparrow + P_\downarrow)^2\, (\delta R)^2 + R^2 \left[\frac{1}{n_+}(1-R)^2 + \frac{1}{n_-}(1+R)^2\right] \left(\frac{\delta P}{P}\right)^2\right\}\end{aligned}$$

$$(\delta R)^2 = \frac{4}{(X_\uparrow + X_\downarrow)^4} \left\{X_\downarrow^2\, (\delta X_\uparrow)^2 + X_\uparrow^2\, (\delta X_\downarrow)^2\right\}$$

$$(\delta X_\uparrow)^2 = \frac{1}{n_+^2} \left\{\sum_i \left(\frac{S + 2N_x}{M^2}\right)_{\uparrow i} + \left(\frac{\delta M}{M}\right)^2 \sum_i \left(\frac{S}{M}\right)^2_{\uparrow i}\right\}$$

$$(\delta X_\downarrow)^2 = \frac{1}{n_-^2} \left\{\sum_i \left(\frac{S + 2N_x}{M^2}\right)_{\downarrow i} + \left(\frac{\delta M}{M}\right)^2 \sum_i \left(\frac{S}{M}\right)^2_{\downarrow i}\right\} \qquad \text{(G.9)}$$